Experimental and numerical study on the transition from minor to major overwash of dunes

by

Jens Figlus, Nobuhisa Kobayashi,

Christine Gralher, and Vicente Iranzo

RESEARCH REPORT NO. CACR-09-04
October, 2009

Center for Applied Coastal Research
Ocean Engineering Laboratory
University of Delaware
Newark, DE 19716

ACKNOWLEDGEMENTS

This study was supported by the U.S. Army Engineer Research and Development Center under Contract No. W912BU-09-C-0023.

TABLE OF CONTENTS

ABSTRACT . . . . . **vii**

Chapter

1 INTRODUCTION **1**
2 EXPERIMENT **5**

2.1 Experimental Setup 6

2.1.1 Sediment Characteristics 8
2.1.2 Test Procedure 10

2.2 Wave Generation and Measurement 12

2.2.1 Wave gauges 12
2.2.2 Acoustic Doppler Velocimeters 14

2.3 Profiling 18

2.3.1 Laser Line Scanner 18
2.3.2 Ultrasonic Thickness Gauges 23

2.4 Overwash Collection 24

2.4.1 Water Collection Basin 24
2.4.2 Sand Trap 27

3 DATA ANALYSIS . . . 29

3.1 Hydrodynamics . . . 29

3.1.1 Free Surface Elevation and Wet Probability . . . 29
3.1.2 Velocity . . . 48

3.2 Morphology . . . 52

3.2.1 Profile Evolution . . . 52
3.2.2 Erosion and Deposition . . . 57

3.3 Overwash . . . 64

3.3.1 Transport Rates . . . 64
3.3.2 Overwash Volume and Profile Change Relationship . . . 70
3.3.3 Sediment Analysis . . . 76

4 NUMERICAL MODEL CSHORE . . . 81

4.1 Combined Wave and Current Model . . . 81
4.2 Probabilistic Model for Wet and Dry Zone . . . 85
4.3 Sediment Transport Model . . . 89

5 COMPARISON OF NUMERICAL MODEL WITH EXPERIMENT . . . 95

5.1 Input Parameters . . . 95
5.2 Hydrodynamics . . . 96
5.3 Profile Evolution . . . 108
5.4 Wave Overtopping and Overwash Rates . . . 111

6 VERIFICATION OF CSHORE WITH ADDITIONAL PROFILE DATA . . . 115

6.1 Laboratory Dune Data . . . 115
6.2 Field Dune Data . . . 121

7 CONCLUSIONS . . . 127

Appendix

A COMPUTED HYDRODYNAMICS IN WET ZONE 131

A.1 Energy Flux and Dissipation Terms 131
A.2 Radiation Stress Term and Bottom Friction 134
A.3 Intrinsic Wave Period, Breaking Wave Fraction, and Roller Volume Flux 137

B COMPUTED SEDIMENT TRANSPORT 141

B.1 Probability of Sediment Movement and Suspension and Suspended Volume 141
B.2 Bed Load and Suspended Load Transport Rates 144

REFERENCES 147

ABSTRACT

Wave-induced overwash of sand dunes may cause rapid profile changes and possible dune destruction, thus increasing the flood risk landward of dunes. Accurate modeling of the wave overwash processes is therefore essential in predicting dune profile evolution during overwash events but available field and laboratory data are very limited. The transition from minor to major overwash has not been quantified previously. Dune profile evolution and overwash transport rates were measured for three tests with different initial dune geometries in front of a low-crested vertical wall exposed to the same wave conditions in a wave flume. The vertical wall proved effective in limiting the wave overtopping rate and reducing the overwash rate after the dune was destroyed.

In all three tests, the transition from minor to major overwash occurred rapidly but the resilience of the dune against destruction depended on its initial geometry. These tests are used to asses a numerical model for wave overtopping and overwash of a dune. The numerical model is shown to be in agreement with the measurements of the free surface elevations, fluid velocities and dune profiles. Wave overtopping and sand overwash rates are predicted reasonably well with a modified sediment transport formulation. However, beach erosion in front of the exposed wall is underpredicted.

Using available field and laboratory data, the numerical model is also shown to be capable of predicting measured field and laboratory profile changes for overwash conditions ranging from no or little overwash to major overwash and complete destruction of the dune.

Chapter 1

INTRODUCTION

Coastal dunes are natural barriers protecting areas along many of the world's sandy coastlines against storm surge and wave action. Waves attacking the beach during extreme surge events often have enough energy to overtop the dune crest and create landward transport of water and sediment. The landward transport of water over the highest profile elevation is called wave overtopping and similarly, the landward transport of sediment is termed overwash. The dune may erode rapidly and the lowering of the dune crest may lead to the increase of wave overtopping and overwash. The transition from minor to major wave overwash is examined experimentally and numerically in this report to elucidate the dune destruction processes by wave overtopping. Breaching of a sand barrier has been investigated by other researchers (e.g., Wamsley et al., 2006). However, local dune breaching is not considered in this report.

Predicting beach profile changes and overwash accurately is important for effective flood risk assessment, sustainable development of coastal areas and engineering design of beach nourishment projects (CEM, 2003), especially in view of sea level rise. Because of the complexity of the involved sediment transport processes, comprehensive field and laboratory observations are essential for the development of numerical morphology models (Donnelly et al., 2006).

An experiment was conducted in a wave flume to measure the temporal changes of wave overtopping and sand overwash rates with the dune profile evolution. Three-dimensional laser scans of the evolving bottom morphology allowed

us to monitor dune profile changes at high resolution in time and space. The experiment comprised three tests with different initial dune geometries constructed in a sand-bed wave flume in front of a low-crested vertical wall. This experimental setup corresponds to a dune in front of a seawall or a dune with a relatively steep landward slope located on a low backshore because sediment transported over the crest of the wall was removed in this experiment. An innovative sand trap located inside a water collection basin behind the vertical wall enabled us to measure the temporal variations of overwash transport rates and sediment characteristics. Each of the three tests was continued even after the exposure of the wall in order to examine the effect of wave overtopping on beach erosion in front of the wall. The literature review by Kraus and McDougal (1996) suggests that wave overtopping is not considered in the discussion of the effects of seawalls on the beach.

The present study aims at creating a unique set of laboratory data pertaining to longshore uniform wave-induced overwash of dunes. Measured profile and overwash evolution is separated into three phases of minor overwash, major overwash and beach erosion in front of the wall. These data are then used to modify and calibrate the numerical model CSHORE (Kobayashi et al., 2010) developed to predict berm and dune erosion in the absence of wave overtopping. The following chapters describe the experiment setup, instrumentation, collected data, and analysis procedures. Furthermore, the essential parts of the numerical model CSHORE are explained before comparisons between the data and CSHORE are presented to show the capability and difficulty in capturing the essential hydrodynamic and morphological processes during the transition from minor to major overwash.

Additionally, the modified CSHORE is compared with profile changes in previous laboratory experiments of dune erosion with no or minor overwash and several field measurements of pre- and post storm dune profiles of severe erosion with and without overwash. These comparisons indicate that the latest CSHORE can predict

dune erosion and overwash under various conditions if one empirical parameter in CSHORE is calibrated. Finally, the experimental and numerical results are summarized and conclusions are presented. Further computed results including additional hydrodynamic and sediment transport variables are presented in Appendices A and B to show the utility of CSHORE in examining the processes of wave overtopping and overwash.

Chapter 2

EXPERIMENT

In this chapter the experimental setup for three overwash test series conducted in the UD "Sand Tank" is presented. Instrument calibrations and measurement confidence bounds are explained. Special focus lies on the processes of obtaining accurate bottom profiles as well as water and sediment overwash volumes.

Conducting the overwash experiment including evolving bottom morphology is inherently challenging due to the number of interlinked processes involved. Hydrodynamic forcing (i.e. wave action, storm surge, currents) and beach profile evolution are always coupled and constantly changing. This complicated relationship manifests itself in the high uncertainty of overwash (sediment and water) prediction. Under severe storm conditions (high surge level and large waves) overwash processes, however, play a major role in reshaping the morphology of beach-dune systems, especially in the subaerial portion of the profile. Hence, the goal of the experiment described hereafter is to gain better understanding of wave-induced overwash processes and their effect on the evolution of sandy beach profiles. Emphasis is put on onshore sediment transport and dune crest lowering due to wave overtopping. Furthermore, the measured data is used to calibrate the numerical model CSHORE for major wave-induced overwash events. Another goal with a more practical engineering application is to answer the question on how the geometry of the dune affects its resistance against destruction by wave overtopping and overwash. This knowledge is important for the design of the nourished beach and dune shape since current practice only considers placed sediment volume but no specific geometry.

2.1 Experimental Setup

The overwash experiment was conducted in the UD "Sand Tank" movable bed wave flume which has dimensions of $30\,m \times 2.4\,m \times 1.5\,m$ $(L \times W \times H)$ and is equipped with a piston-type wave maker on one end and an energy absorbing gravel embankment on the other end. The flume has been upgraded to include a state-of-the-art laser profiling system (Section 2.3) and a water collection basin with a sediment trap (Section 2.4) in addition to already existing instruments including nine capacitance wave gauges and two acoustic Doppler velocimeters (ADV) which are explained in detail in Section 2.2. Figure 2.1 shows a schematic side view of the section of the flume used for the experiment.

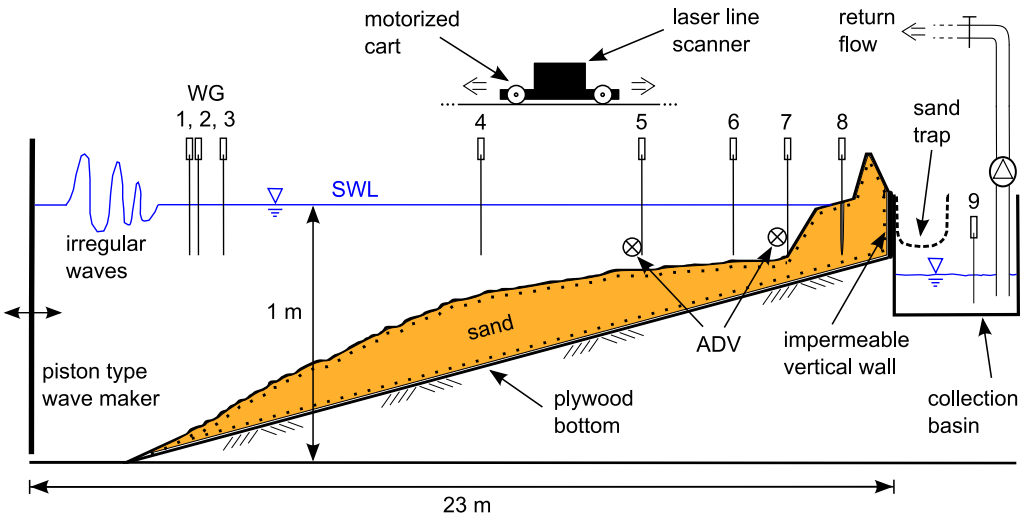

Figure 2.1: *Schematic side view of the overwash experiment setup including wave paddle, beach profile on top of plywood slope, collection basin with sediment trap, water recirculation system and measurement instrument locations.*

A dividing wall is located along the center line of the flume in order to minimize seiching and limit the amount of sand required for the experiment. Approximately ten tons of sand have been placed on top of a 1/30 rigid plywood slope stretching from $3\,m$ past the wave paddle all the way to an impermeable vertical wall behind which the overwash collection basin is located. The collection basin is a

plastic tub reinforced with plywood panels and held in place by four vertical shoring posts. During a test run overwash sediment and water flow over the crest of the impermeable vertical wall and pass through a sand trap constructed of a lightweight aluminum frame and a polyester fabric mesh with a micron rating of 74 retaining overwash sediment larger than silt. Details on the overwash collection system are given in Section 2.4.

A right-hand Cartesian coordinate system is used in the following. Its origin coincides with the still water level (SWL) at the location of offshore wave gauge 1 (WG1) and its x-axis points onshore along the centerline of the flume section. The z-axis is positive upward. Most measurement instruments used in the experiment are mounted on metal frame carts which can be moved in cross-shore direction along a set of T-tracks (Figure 2.2). One of the carts is controlled by a servo motor with

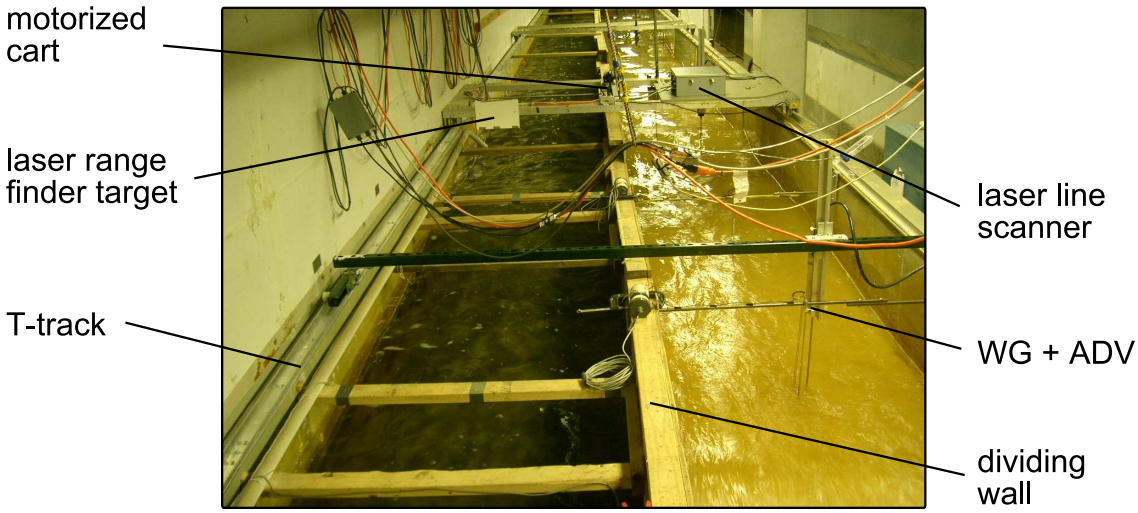

Figure 2.2: *Picture of wave flume setup facing offshore.*

continuously adjustable speed setting. It houses a laser line scanner capable of recording up to 50,000 distance samples per second as the laser beam is deflected from its horizontal direction of origin by a rotating mirror assembly to prescribe a 360° sweep in the vertical (y-z coordinate) plane normal to the cross-shore coordinate

x (Section 2.3). The cross-shore (x) position of the motorized cart is measured by a stationary laser distance finder placed next to the collection basin at the height of the cart. It shoots its beam horizontally at a reflective target mounted on the cart. The synchronized distance data from the two lasers allows for recreation of the 3D flume topography. For our experiment the field of view is limited to the sandy bottom profile.

2.1.1 Sediment Characteristics

The sediment used in the experiment is considered poorly graded (well sorted) fine sand of light brown color. Grain shapes are subangular to subrounded and the Unified Soil Classification System (USCS) label for this sand is SP. The grain size distribution obtained from a sieve analysis of several sand samples yields the characteristic sediment diameters used in the subsequent data analysis (see Figure 2.3). In order to get a better representation of the actual sediment diameters retained in each sieve, geometric mean values of sieve openings between adjacent sieves are used. The uniformity coefficient, C_u, and the coefficient of curvature, C_c, of the sediment are calculated from the size distribution curve as

$$C_u = \frac{d_{60}}{d_{10}} = 1.7 \quad ; \qquad C_c = \frac{(d_{30})^2}{d_{60} \times d_{10}} = 0.9 \tag{2.1}$$

where indices of the characteristic diameters used in the computation indicate percent finer by weight.

Buck et al. (2007) performed further tests to determine the sand's specific gravity as the ratio of sand density to fresh water density ($s = \rho_s/\rho_w$), its porosity, n_p, and its average fall velocity, w_f. A summary of the analysis results is given in Table 2.1.

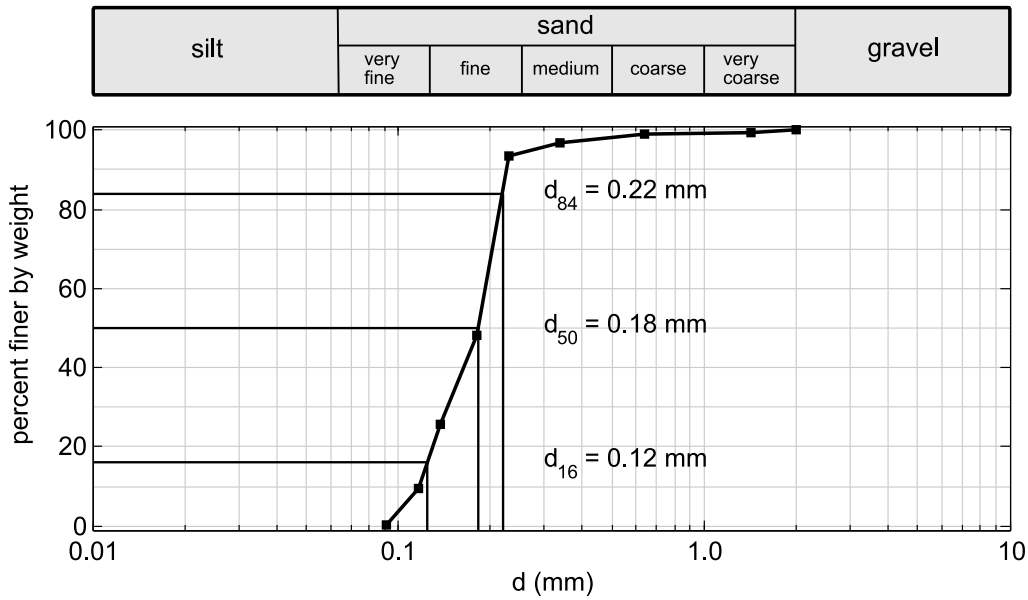

Figure 2.3: *The sieve analysis of the sediment used in the experiment shows a well sorted grain size distribution of mainly fine sand. The data points are geometric mean diameters corresponding to adjacent sieve sizes.*

Table 2.1: *Sediment characteristics.*

USCS label	SP (poorly graded sand)
color	light brown
grain shape	subangular to subrounded
$d_{16},\ d_{50},\ d_{84}$	$0.124\ mm,\ 0.183\ mm,\ 0.221\ mm$
$d_{10},\ d_{30},\ d_{60}$	$0.117\ mm,\ 0.146\ mm,\ 0.194\ mm$
$C_u,\ C_c$	$1.7,\ 0.9$
$s,\ n_p,\ w_f$	$2.6,\ 0.4,\ 2.0\ cm/s$

2.1.2 Test Procedure

Several steps make up the entire test procedure. After the initial beach profile is constructed and scanned, the water depth in the flume is raised to $100\,cm$ followed by the calibration of all the instruments. Then, an irregular wave train of 400-s duration with a TMA spectral shape is created by the wave maker (the spectral dignificant wave height $H_{mo} = 19\,cm$, and the spectral peak period $T_p = 2.6\,s$). During the run, free surface elevation and water velocities are measured at specified locations throughout the flume. The waves transform as they encounter the changing bottom geometry. They break, form a surf zone and create uprush on the dune face and subsequent overwash. The portion of overwash passing the crest of the impermeable vertical wall at the end of the beach profile is collected in the designated sand trap and collection basin. Cumulative water and sand overwash are measured in each run followed by a sieve analysis of the overwash sand. After each 400-s run the bottom profile is scanned to record any bathymetry changes before the next run is started. The test series ends when the dune is completely destroyed and the SWL reaches the vertical wall in front of the collection basin.

The overwash experiment is made up of three different tests which consist of a number of wave runs. Three different initial nearshore profile shapes are tested for their resistance against the same surge and incident wave conditions. The initial setup for each test comprises the identical amount of sand and differs only in dune and foreshore geometry. The three tests are labeled BD (berm and dune), WD (wide dune), and SD (slope in front of dune) and are depicted in Figure 2.4 along with the respective characteristic slopes making up each dune profile. Total test series duration, the number of 400-s runs and the number of profile scans are given in Table 2.2 for the BD, WD, and SD tests. The run number is indicated by an integer placed after BD, WD and SD.

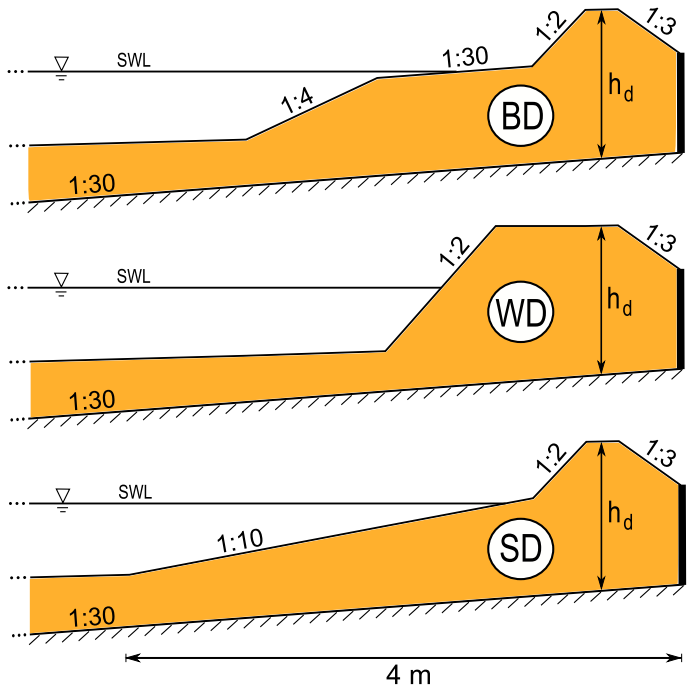

Figure 2.4: *Three initial nearshore profile setups for BD (berm and dune), WD (wide dune), and SD (slope in front of dune) tests. Sand volume per unit width (shaded area) and dune height (h_d) are identical.*

Table 2.2: *BD, WD, and SD test overview.*

	BD	WD	SD
400-s runs	18	12	15
total duration	7200 s	4800 s	6000 s
profile scans	19	13	16

2.2 Wave Generation and Measurement

Waves are created by the paddle of the piston-type wave maker located at the offshore end of the flume. The water depth at the wave maker is $1\,m$ in this experiment. The input signal to the wave actuator consists of a time series ($400\,s$ at $20\,Hz$) of voltage values corresponding to a certain paddle displacement aiming to reproduce an irregular wave train with a TMA spectral shape. A National Instruments 16 channel SCSI data acquisition board controlled by a LabView user interface handles data logging and wave maker control simultaneously. The data from all instruments is recorded at $20\,Hz$.

2.2.1 Wave gauges

Free surface elevation in the flume is measured by 8 capacitance wave gauges (WG1-8) located mostly along the center line in the wave flume section of $1.15\,m$ width (Table 2.3). Only WG4 and WG5 are placed with an offset which does not affect the results since the distance to the flume wall is more than $0.3\,m$. Capacitance wave gauges include a vertical electrical wire loop connected to a circuit board which employs two frequency oscillators to determine the capacitance in the wire over a set range. As the waves pass the half-submerged wire, the capacitance registered by the circuit board changes proportionally to the depth of the wire submerged in water. The conversion to water free surface elevation η follows a linear relationship with measurement errors of $\pm 1\,mm$.

Wave gauge placement is explained in the following. Offshore wave conditions and run repeatability are checked by WG1 through WG3, where three gauges are necessary to separate incident and reflected wave signals following Kobayashi et al. (1990). The chosen spacing between the three gauges yields a resolvable frequency range of $0.15 - 1.70\,Hz$ for this procedure. Data from WG4 through WG8 show the transformation of the shoaling wave train as it travels from offshore (wave paddle) toward onshore (dune). WG4 and WG5 capture a majority of the changes related

to wave breaking, whereas WG6, WG7, and WG8 give insight into inner surf zone dynamics and wave uprush on the beach-dune system. Wave gauges are classified as “free” if their wire does not extend below the sand bottom surface or “buried" if their wire reaches into the sandy bottom (Table 2.3). Furthermore, gauges are either submerged under water or intermittently exposed to air. The classification shown in Table 2.3 corresponds to the setup at the beginning of each test and plays a role for the respective data analysis procedure which is explained in more detail in Chapter 3.

Table 2.3: *Wave gauge locations and classification for BD, WD, and SD tests.*

	WG1	WG2	WG3	WG4	WG5	WG6	WG7	WG8
x (m)	0.00	0.25	0.95	8.30	12.90	15.52	17.07	18.61
y (m)	0.00	0.00	0.00	-0.20	-0.25	0.00	0.00	0.00
free	✓	✓	✓	✓	✓	-	-	-
buried	-	-	-	-	-	✓	✓	✓
submerged	✓	✓	✓	✓	✓	✓	✓	-
exposed	-	-	-	-	-	-	-	✓

During wave gauge calibration, a linear calibration curve is determined for each submerged gauge, relating the recorded voltage signal to its respective water level. First, the water level in the tank is raised to its maximum value just below the rim of the collection basin and all wave gauges are set to their mean positions with regard to SWL. Then, the tank is drained and the WG voltages are recorded for every $1\,cm$ of water level change. Each measurement is triggered by the reading of a reference gauge (WG3) which is calibrated by lowering its wire into the water via a stepper motor before the other wave gauges are calibrated. All submerged wave gauges are calibrated for a range of $15\,cm$ below SWL which exceeds $3\sigma_\eta$ where σ_η is

the free surface standard deviation discussed in Chapter 3. The calibration curve is then extrapolated to include the entire range of water levels present in a wave run.

Since WG8 was not submerged at the beginning of several runs to measure swash dynamics on the initial foreshore, the above described conventional calibration method could not be applied. Instead, the gauge was calibrated for a range of $\pm 15\,cm$ around the center of its wire in a water filled Plexiglas cylinder outside the flume before being buried in the sand. The slope of the obtained calibration curve was used to convert the measured voltages to free surface elevation during a wave run. The conventional calibration method was only used after profile erosion had advanced far enough to submerge WG8 in at least $8\,cm$ of water below SWL at the beginning of the run.

2.2.2 Acoustic Doppler Velocimeters

Fluid velocity data is recorded by two SonTek ADV sensors co-located with WG5 and WG7, respectively. Their respective sampling volumes are positioned 2/3 of the local water depth d below SWL (Table 2.4).

Table 2.4: *ADV measurement volume locations for BD, WD, and SD tests.*

	ADV1 (3D)	ADV2 (2D)
x (m)	12.88	17.02
y (m)	0.15	0.15
z (m)	$-2/3\ d$	$-2/3\ d$

d = local water depth at the start of each run.

ADV1 at the WG5 location is a 3D instrument with downward pointing probe tips measuring velocities in the cross-shore (u), alongshore (v), and vertical (w) directions in a sampling volume 5 cm below the probe tips. ADV2 at the

WG7 location is a 2D instrument with sideways pointing probe tips which allows for measurement of the two velocity components u and v at the location of the sampling volume. An acoustic pulse is emitted from the transmitter and reflected by suspended particles in the passing water. The signal picked up by the receiving probe tips is Doppler shifted due to the motion of the water past the probe which allows for calculation of the fluid velocity. Since fine sand is suspended during each wave run both ADVs give strong signal-to-noise ratios with error estimates of $\pm 0.5\ cm/s$.

An example of the time series of recorded free surface elevation η and cross-shore velocity u data is displayed in Figure 2.5 for a 50-s window during run WD6 for measurements at the locations of WG1, WG5, and WG7. Velocity information is available only at the two locations of ADV1 and ADV2, respectively. Transformations in the shape of the wave train are apparent when comparing the top panel (offshore) to the center and bottom panels where the waves appear more peaked with flatter troughs as expected.

Spectral analysis is performed on all WG time series showing the distribution of wave energy with frequency. Power spectra are obtained from the free surface elevation records after eliminating the initial ramp-up period of $20\,s$. Figure 2.6 displays measured spectra computed from the measured time series at the locations of WG1, WG5, and WG7 during run WD6 where the bottom panel shows the same information as the top panel but with logarithmic ordinate scaling. The observed energy losses near the spectral peak can be contributed to wave breaking and bottom friction.

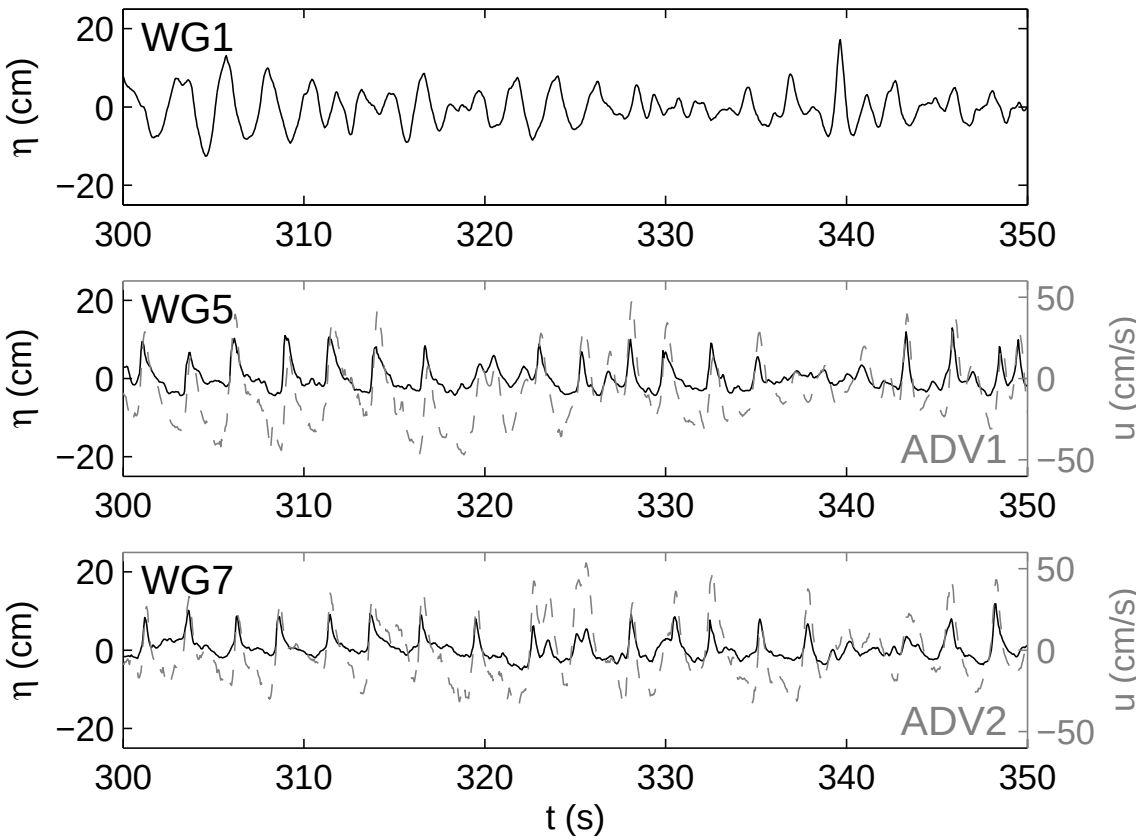

Figure 2.5: *Measured free surface elevation η at WG1, WG5, and WG7 locations (black) and measured cross-shore velocity u at ADV1 and ADV2 locations during a 50-s window of run WD6 ($t = 300 - 350\,s$).*

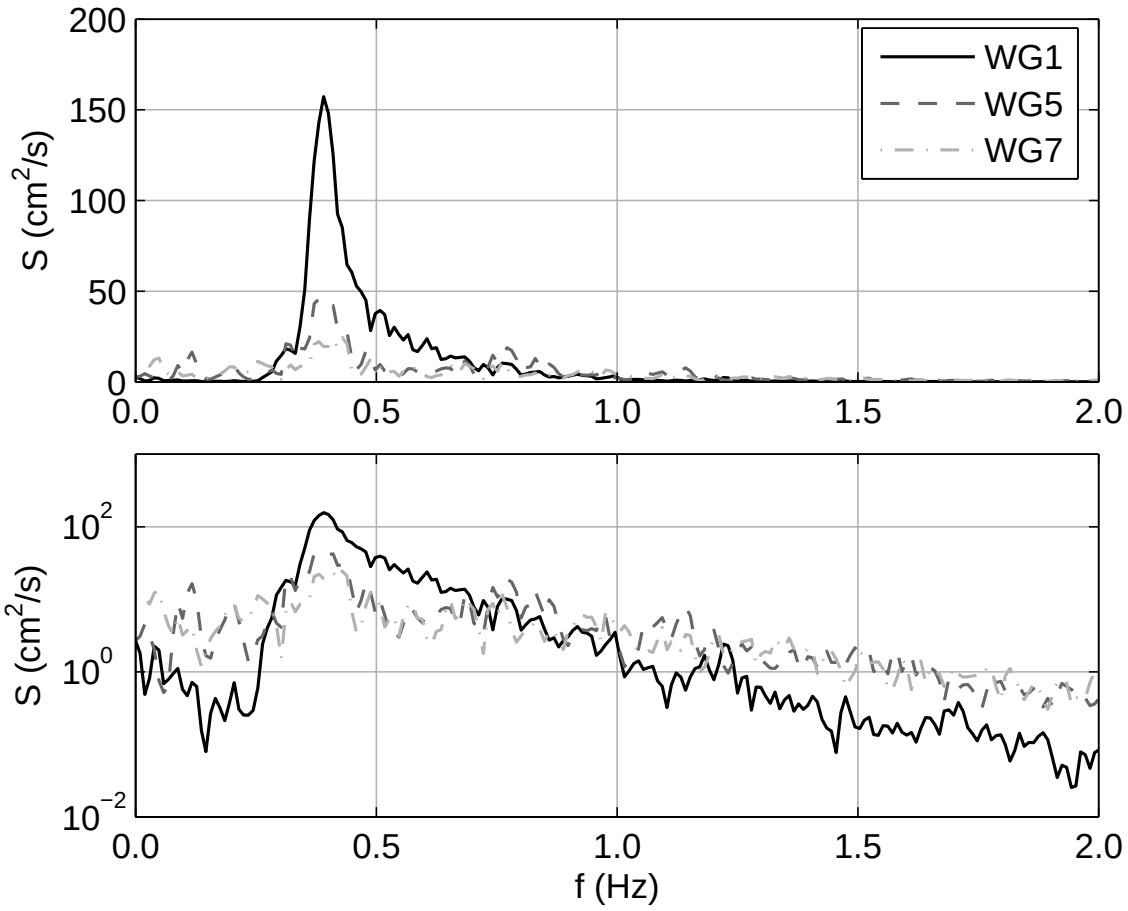

Figure 2.6: *Spectral density of wave signals at WG1, WG5, and WG7 locations during run WD6. The bottom panel shows the power spectra with a logarithmic ordinate scale for better visualization of the high and low frequency components.*

2.3 Profiling

The bottom morphology in the experiment changed rapidly over the course of a test. This is mainly due to the intense wave action and high surge level which caused major wave-induced overwash events and destruction of the dune. Since one of our goals is to gain a better understanding of the interaction between wave-induced overwash processes and morphological profile changes, it is crucial to obtain measurements of profile changes at high spatial and temporal resolution with a high level of accuracy.

Two different measurement systems are employed to record bottom morphology changes. The subaerial portion of the beach profile is measured by a laser line scanner and the submerged portion is measured using ultrasonic thickness gauges.

2.3.1 Laser Line Scanner

Bottom morphology changes during overwash events are most prominent in the beach profile region encompassing the berm and dune. Scanning this area of rapid profile change using laser technology has many advantages including the possibility for automation and direct data logging as well as the high level of accuracy and the low time requirement. The manual profiling with a vernier point previously used by Buck et al. (2007) was extremely time consuming.

A class III Acuity AR4000-LIR laser line scanner system (Figure 2.7) in conjunction with a class II Acuity AR1000 laser distance finder delivers high-resolution 3D scans of the subaerial portion of the bed profile. Both lasers obtain distance measurements via a time-of-flight measurement of the emitted laser beam as it reflects of a target. The main components of the AR4000 line scanner system are the horizontally mounted $780\,nm$ IR laser diode with an optical power output of $8\,mW$ and a rotating mirror assembly which deflects the outgoing and reflected laser beam by 90° to allow for a 2D scan of the vertical (y-z) plane during a full 360° sweep of the mirror around its horizontal axis.

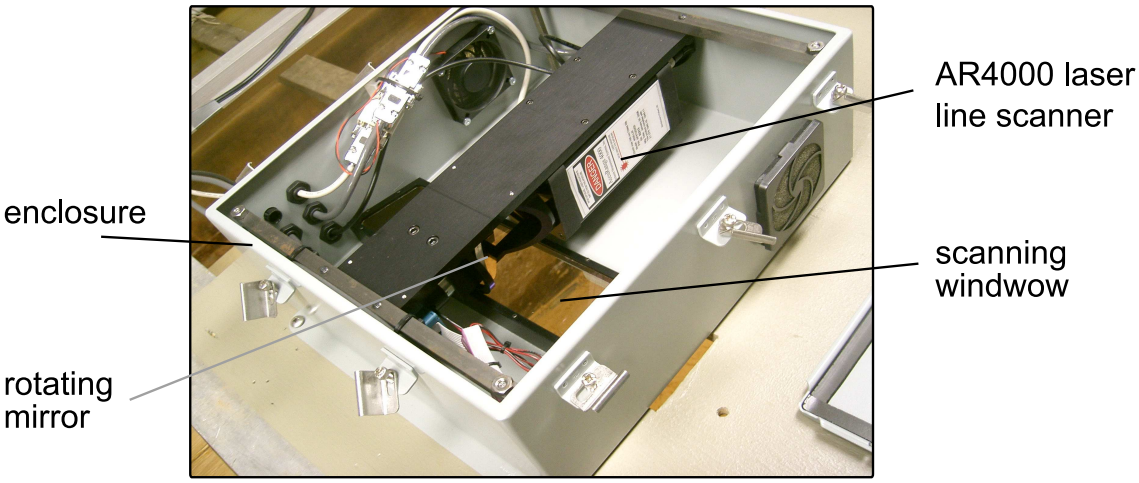

Figure 2.7: *The AR4000 laser line scanner system is mounted inside an enclosure case on a motorized cart and includes a rotating mirror to deflect the laser beam for 360° scans. Only distance samples collected within the field of view limited by the enclosure scanning window are processed.*

Performance and measurement accuracy depend on a variety of factors like distance from the target, amplitude of the return signal (reflectivity of the target), and three types of noise including detector thermal noise, laser diode noise, and noise related to the chosen sampling resolution. The line scanner has a maximum range of $9\,m$ but is configured with a close focus optics option which yields the greatest measurement sensitivity around $1\,m$ from the sensor, consistent with the required range of $0.5 - 1.5\,m$ in the experiment.

Fine sand has good diffuse reflective properties which leads to high return signal amplitudes in the detection photo diode. This ensures very accurate readings but the three types of noise that can affect the standard deviation of the return signal vary depending on the sampling rate. The AR4000 line scanner is connected to a PC via a high speed interface card capable of sampling distance measurements at a rate of $50,000\,Hz$. For the present application the sampling rate is set to $10,000\,Hz$ which yields an rms noise value or standard deviation of approximately $1.5\,mm$ mainly related to drift and fluctuation of the emitted laser beam (laser

diode noise). For more information on operation and performance of the AR4000-LIR line scanner consult the user's manual (Acuity, 2003b) which is available online (`www.acuityresearch.com`).

In order to be able to create 3D images of the surface scanned by the line scanner a third axis of motion is needed in addition to the rotation of the mirror. Therefore, the line scanner system is mounted on a motorized cart moving along the flume's x-axis on a set of T-tracks. Care has been taken to arrange the line scanner in such a way that the axes of mirror rotation and emitted laser beam coincide with the centerline (x-axis) of the flume so that one sweep of the mirror yields distance measurements of an alongshore slice of the flume topography. This was accomplished by calibrating the line scanner position through repeated scans of a custom made aluminum frame with an adjustable horizontal bar and vertical walls with exact right angles.

In an effort to limit the amount of data collected during scanning, the field of view is limited mechanically by an enclosure case and electronically through software to 60° on either side of the vertical (z-axis) facing downward from the cart into the flume which is sufficient to digitize the entire width of the sandy bottom topography.

The cart is equipped with a servo motor and control unit capable of moving the line scanner back and forth in the cross-shore direction with continuously adjustable speeds up to $10\,cm/s$ per second. The x-coordinate of the 2D slice scanned by the line scanner at any point along the flume is provided by the AR1000 distance sensor. This laser range finder emits a horizontal beam of visible red light ($650\,nm$) with optical power output of $1\,mW$. It measures the distance from its fixed position next to the collection basin to the moving cart. A portion of the light scattered from a reflective target mounted on the motorized cart is collected and focused on a photo detector inside the AR1000 to calculate the distance of the target from the fixed position of the range finder via the time-of-flight method. Since a reflective

target is used, the AR1000 can measure distances of up to $150\,m$ with an accuracy of $\pm 2\,mm$ (Acuity, 2003a). Figure 2.8 shows a top view schematic of the described arrangement.

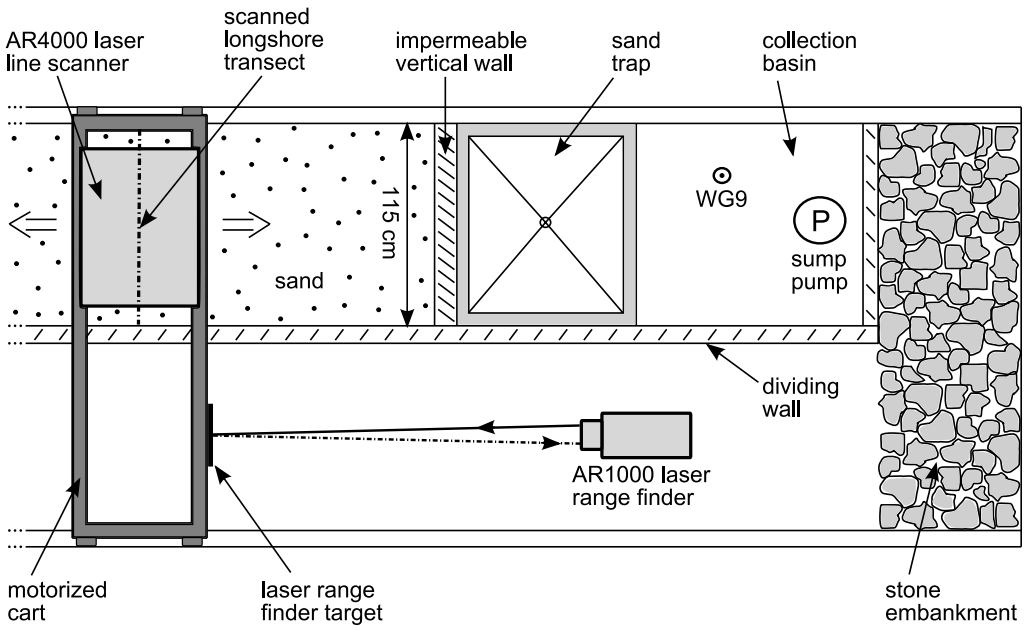

Figure 2.8: *Schematic top view of experimental setup. The fixed AR1000 laser range finder gives the x-location of the motorized cart traveling along the flume at constant speed while the AR4000 laser line scanner measures longshore transects of the bottom profile at specified increments.*

During a scan the cart is moving at a constant speed of $1\,cm/s$ while the line scanner does sweeps of alongshore slices in a fraction of a second at set cross-shore increments controlled by the AR1000 distance sensor. The scanned alongshore slices are practically perpendicular to the x-axis since the slow translatory motion of the cart during an entire 360° sweep of the line scanner is negligible compared to the high speed rotation of the mirror. For this experiment the line scanner has been configured to collect 500 data points per alongshore slice at a sampling frequency of $10,000\,Hz$ which corresponds to a measurement time of $0.05\,s$ per slice. The rotation speed of the mirror is set to allow for 3 revolutions during that time. Alongshore

slices are measured every $2\,cm$ over a length of $14\,m$ in this experiment which leads to an overall time of 20 minutes required for one complete scan.

Data from the line scanner and distance finder are collected through the high speed interface card and the RS232 serial connection, respectively, and streamed to file using custom programmed LabView software which accesses dynamic libraries specifically written to control the AR4000 line scanner system (Dunnum, 2006). An example of a 3D image created from the measured laser data is shown in Figure 2.9 where the nearshore section of the initial profile for the BD test is displayed including the vertical wall behind the backdune.

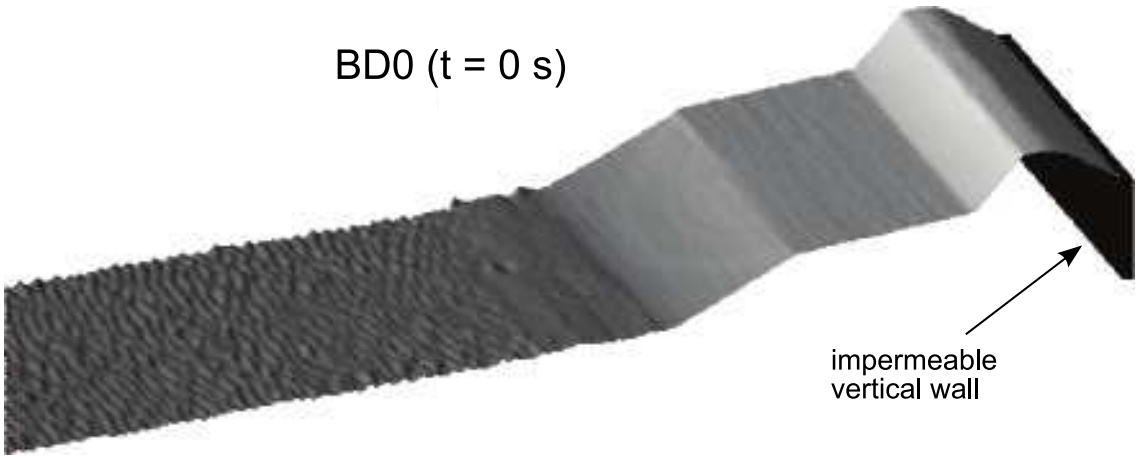

Figure 2.9: *Image of the initial nearshore profile of the BD test scanned by the AR4000 laser line scanner in conjunction with the AR1000 distance sensor. One unit of vertical and longshore length is equal to two units of cross-shore length (data aspect ratio x:y:z = 2:1:1).*

As mentioned before, only the subaerial portion of the profile can be scanned by the line scanner system since the laser distance measurements are calibrated for time-of-flight in air. However, since the scan is automated, accurate and requires only little time, the subaerial portion is increased to stretch over a cross-shore distance of $14\,m$ ($x = 6 - 20\,m$) by lowering the water level in the tank to the desired

level after each run. The limit of $x = 6\,m$ is located well seaward of WG4 positioned at $x = 8.3\,m$ as listed in Table 2.3.

2.3.2 Ultrasonic Thickness Gauges

The offshore portion of the profile ($x = 0 - 7\,m$) including $1\,m$ of overlap with the laser scan is measured using three submerged $1\,MHz$ ultrasonic transducers connected to a Panametrics 25MX precision thickness gauge via an MX-8 multiplexer. The transducers measure the time for acoustic signals to be reflected from the sandy bottom and convert it to the water depth at this specific location. They are mounted $30\,cm$ apart in an alongshore array on a specialized vernier caliper extending downward into the water from a movable cart. As the cart is moved from one cross-shore location to the next along the flume the transducers take depth readings at their respective alongshore locations yielding three individual cross-shore profile lines at $y = 30\,cm$, $y = 0\,cm$, and $y = -30\,cm$. A representative 2D offshore profile is then obtained by averaging the three transects.

The transducers give depth readings to millimeter precision up to their operational limit of $10\,cm$ from the reflective bottom boundary. The vernier caliper is adjusted before each scan to stay within this operational range. Hence, the measurement accuracy of the acoustic profiling method is mainly dependent on the vernier caliper precision and is assumed to be on the order of $5\,mm$. Collected data is logged by the 25MX thickness gauge and later transferred to a PC for further processing. The time requirement to scan the offshore portion of the profile is approximately 30 minutes.

2.4 Overwash Collection

The experiment is conducted to measure overwash volumes of water and sediment during the peak of a storm surge event from the onset of wave overtopping (minor overwash) to the complete destruction of the dune (major overwash). Buck et al. (2007) already conducted experiments of dune erosion with no or minor overwash under storm surge conditions varying in time. Not surprisingly, the experimental setup needs to have the capability to collect and measure both minor and extreme overwash volumes to an acceptable level of accuracy. This is accomplished by a custom-built water collection basin behind the backdune which houses a horizontal sand trap to separate the overwash sediment from the overtopping water (Figure 2.10).

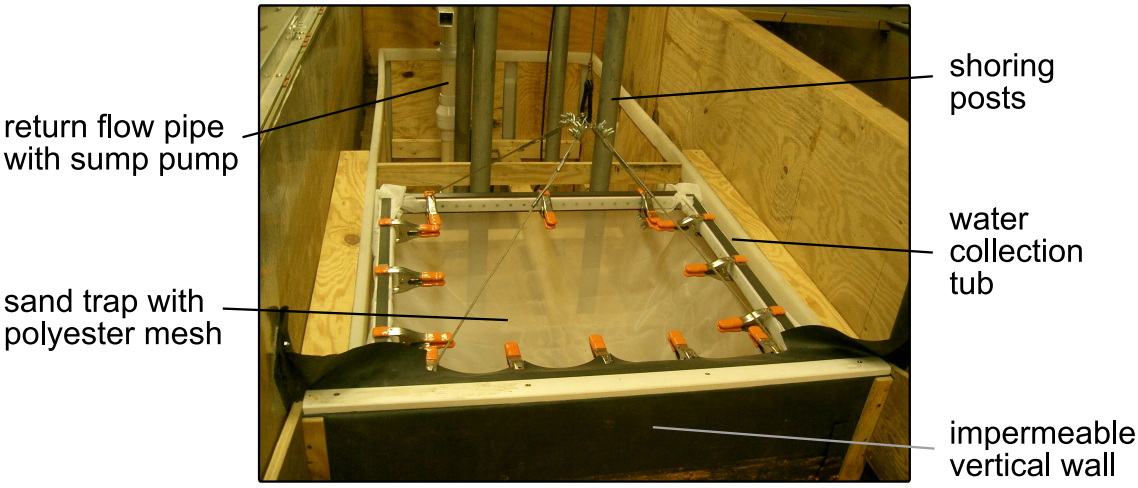

Figure 2.10: *Sand trap and water collection basin setup.*

2.4.1 Water Collection Basin

The rectangular water collection basin located behind the backdune has a capacity of 500 gallons (1900 liters) with dimensions of $2.44\,m \times 0.97\,m \times 0.78\,m$ ($L \times W \times H$). To prevent leakage, a one piece seamless polyethylene construction was chosen and scaffolding in combination with plywood panels on the inside walls is used

to preserve the tub's shape against deformation from the hydrostatic water pressure during a run. The rim of the basin reaches up to the crest of the impermeable vertical wall ($z = 6\,cm$ above SWL) at the end of the beach profile.

The water level inside the collection basin is measured by two independent systems for redundancy. Both a mechanical float gauge and an electronic capacitance wave gauge (WG9) indicate the location of the water surface within $\pm 1\,mm$ accuracy. The conversion between water surface elevation and water volume contained in the basin is done using linear calibration curves obtained by manually filling the basin with water in 10 liter (ℓ) increments. Slope and intercept of the linear best fit through the calibration points are slightly different for the mechanical float and the capacitance gauge (Figure 2.11) but a maximum error is $4\,\ell$. This error is acceptable for large overwash volume in excess of $100\,\ell$ but is too large for very minor overwash events. Thus, a smaller plastic tub of $100\,\ell$ capacity is used to collect the water that passes through the sediment trap up to $100\,\ell$ water volume. The water collected in the small tub is measured by hand using a graduated cylinder with a maximum measurement error of $0.1\,\ell$.

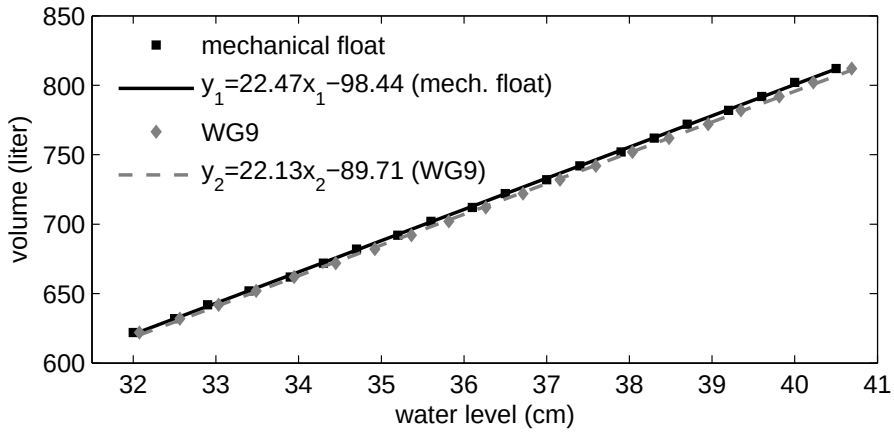

Figure 2.11: *Collection basin calibration curves.*

Once the collected water volume during a single test becomes equivalent to

the water level drop of $1\,mm$ in the flume, a recirculation system pumps water out of the collection basin back into the flume. The recirculation system consists of a Zoeller E284 sump pump, a Bürkert 8035 inline paddle wheel flow meter, a ball valve and two check valves connected by schedule 40 2-inch PVC pipes. Pump operating cycles are controlled by a float switch between maximum and minimum water levels in the collection basin. As soon as the water level exceeds the maximum level, pumping commences until the water level drops to the minimum level.

The inline flow meter (FM) is capable of measuring fluid velocities between 0.3 and $10\,m/s$. A correlation coefficient (K-factor) is necessary to compute flow rates from the measured velocities. The specific K-factor is determined by pumping a known quantity of water through the flow meter. Output signals include a digital display by the FM control unit and an electric current loop with a strength between $4-20\,mA$ proportional to the instantaneous flow rate. The current loop is connected to the data acquisition board for data logging of the instantaneous flow rate. The control unit also includes a totalizing function allowing for quick determination of the total volume of water pumped out over the entire duration of a run.

Measurement errors are below 2% of the pumped volume and have been determined by comparing the cumulative FM reading with the actual water volume collected manually in a measuring container (Figure 2.12). In addition to the manual collection method, the pumped out volumes are determined using the mechanical float and WG9 water level readings in conjunction with their respective calibration curves.

Finally, the total volume of water flowing over the vertical wall in Figure 2.10 during a run is the sum of the volume collected in the collection basin (or small tub for low overwash rates), the volume pumped out during the run, and the volume contained in the wet sand caught in the trap.

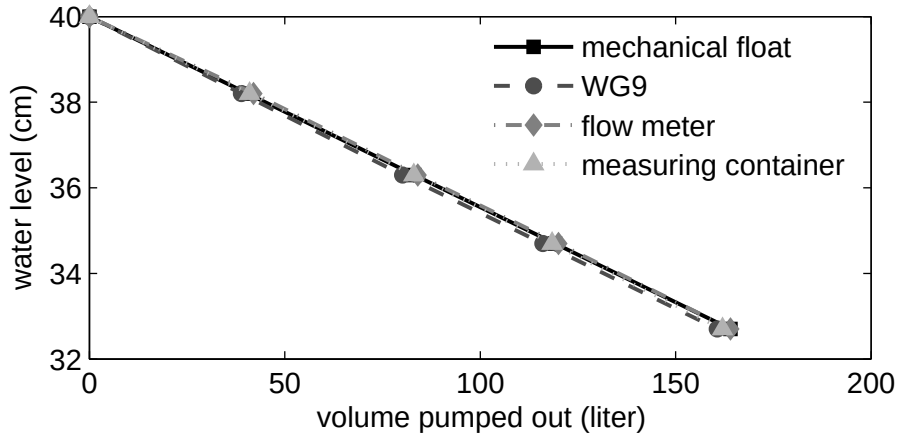

Figure 2.12: *Calibration of flow meter used for measuring water volume pumped through the recirculation system during test runs. Cumulative values obtained through four different methods are shown together.*

2.4.2 Sand Trap

A mixture of suspended load, bedload and water is carried over the crest of the impermeable vertical wall behind the backdune in each run. In order to separate the overwash sediment from the water a horizontal sand trap is lowered into the front third of the collection basin with a tight fit. A rubber lip made from flexible pond liner material directs the water and sediment mixture into the trap. The trap itself is made up of a polyester fabric mesh secured to a lightweight aluminum frame by retaining clamps which allow for easy replacement of the fabric if necessary. Suspended from a slewing crane, the sand trap is easily moved in and out of the collection basin for sand removal or repairs.

The polyester fabric mesh has a micron rating of 74 which means that particles with a diameter exceeding $0.074\,mm$ are retained. Hence, particles considered to be fine sand or larger are collected in the sediment trap whereas particles considered to be silt or clay pass the mesh together with the overwash water. Sediment samples from two locations of the dune area were collected before and after each test. Results from the sieve analyses of these samples indicate that 2% of the sediment

may not have been retained by the polyester mesh.

After each 400-s test run the trap remains in place for approximately 15 minutes to allow most of the excess water contained in the wet overwash sand to drain into the collection basin. The retained wet sand is then removed and weighed before and after oven drying for at least 12 hours to determine its dry weight and the weight of the contained water. The dried sand is then used to perform a sieve analysis. The sieve analysis is done with 400-g samples which are passed through a 74 micron sieve to remove any silt particles still present in the sample. The evolution of the grain size distributions obtained after each run is analyzed in Chapter 3 to examine possible sorting due to wave overwash.

Chapter 3

DATA ANALYSIS

This chapter gives a detailed description of the analysis procedure for all the data collected during the dune overwash experiment. Results are organized into the three main categories: hydrodynamics, morphology, and overwash.

3.1 Hydrodynamics

Free surface elevation and velocity are the two main components of the hydrodynamics measured in this experiment. Wave gauges (WG) and acoustic Doppler velocimeters (ADV) are employed to obtain these measurements (Section 2.2). For the data analysis the initial transition of 20 s in each recorded 400-s time series is removed to eliminate ramp-up effects.

3.1.1 Free Surface Elevation and Wet Probability

During each wave run free water surface elevation η is measured using eight capacitance wire gauges with the still water level (SWL) as the reference datum. The gauge locations have been strategically chosen to cover the entire transformation of the shoaling waves from offshore through steepening and breaking all the way to the creation of uprush and overwash events. The exact placement of the gauges is given in Table 2.3. In Tables 3.1 to 3.3 the incident wave parameters from the spectral and time series analysis of each test are listed. These parameters represent incident offshore values at the location of WG1 and have been computed using the measured time series from WG1, WG2, and WG3 (Section 2.2.1). Included are the

spectral significant wave height H_{mo}, the root-mean-square wave height H_{rms} and the significant wave height H_s as well as the spectral peak period T_p and the significant wave period T_s. In addition, the reflection coefficient R is tabulated. Average parameter values for each test are given at the bottom of the respective table. The parameters H_{mo}, H_{rms}, and T_p are derived from the wave energy spectrum. Integrating the wave frequency spectrum in the full frequency domain yields the zero-th moment, m_0 (cm^2), which is equivalent to the variance of the free surface elevation by definition of the wave frequency spectrum (Goda, 2000). Similarly, the standard deviation, σ_η, is equal to the square root of the zero-th moment ($\sigma_\eta = \sqrt{m_0}$). The spectral significant wave height is defined as $H_{mo} = 4\sigma_\eta$ and the root-mean-square wave height is obtained as $H_{rms} = H_{mo}/\sqrt{2}$. T_p is the wave period associated with the largest wave energy (reciprocal of the frequency at the peak of the wave frequency spectrum). The values of H_s and T_s are derived from the measured time series of the free surface elevation via the zero-upcrossing method which associates a certain height and period with each wave. The average height of the highest one third of the waves in the time series is the significant wave height H_s and the average period of these waves is T_s.

As expected, all offshore wave parameters listed in Tables 3.1 to 3.3 varied little throughout the experiment with only minimal variation in the individual runs since the water level in front of the wave maker was kept constant at $100\,cm$ and the same irregular wave signal was used in every run. For the entire experiment the average value of H_{mo} (H_{rms}) was $18.90\,cm$ ($13.36\,cm$) with a minimum of $18.33\,cm$ ($12.96\,cm$) in run WD4 and a maximum of $19.33\,cm$ ($13.67\,cm$) in run WD10. H_s was very close to H_{mo} with only minor differences of less than $2\,mm$ for individual runs. The overall average value of H_s was $18.81\,cm$. Spectral peak period values were constant in every run ($T_p = 2.57\,s$) except for WD1 ($T_p = 2.39\,s$) which may be explained by the effect of the large dune profile changes during WD1 on the recorded

wave signals at the three gauges used to calculate the incident wave parameters. T_s was slightly less than T_p and shows a little more variation ($\pm 0.04\,s$) with an overall average value of $2.31\,s$. The reflection coefficient, R, had a constant average of 0.16 but varied slightly in each test from higher to lower values which can be attributed to the flattening of the bottom profile in the dune region.

An example of the total, incident and reflected wave frequency spectra obtained from the analysis of the three offshore gauge records is plotted in Figure 3.1 where the bottom panel shows the same results after an 8 point spectral smoothing is applied. The largest wave energy for this run is associated with a peak frequency of $f = 0.389\,Hz$ which corresponds to a peak period of $T_p = 2.57\,s$ (Table 3.1). Incident and total spectral shapes are very similar with only minor reduction of the incident wave energy around the peak period caused by wave reflection. The plot also reveals that the frequency limits ($0.15 - 1.70\,Hz$) imposed by the three wave gauge analysis procedure (Section 2.2.1) is sufficient for the range of measured frequencies in the flume since no significant wave energy in the total spectrum exists outside these limits.

Representative for all runs, the truncated 380-s time series of the total, incident and reflected waves at WG1 are shown in the four panels of Figure 3.2 for run BD5, which is the same run as for the spectral example above. The total free surface elevation signal, η_t (panel 1) is measured by the wave gauge and corresponds to the sum of the incident (panel 2) and reflected (panel 3) signals as verified in panel 4. Approximately, 200 waves comprise each of the identical 380-s runs which is sufficient for statistical wave analysis.

Table 3.1: *Spectrum and time series parameters for incident waves at WG1 location for* 18 *runs of BD test.*

Run	H_{mo} (cm)	H_{rms} (cm)	H_s (cm)	T_p (s)	T_s (s)	R
BD1	18.69	13.22	18.47	2.57	2.30	0.17
BD2	19.02	13.45	18.83	2.57	2.32	0.19
BD3	19.09	13.50	18.94	2.57	2.35	0.19
BD4	18.65	13.19	18.54	2.57	2.32	0.18
BD5	18.83	13.32	18.50	2.57	2.31	0.21
BD6	18.68	13.21	18.50	2.57	2.30	0.20
BD7	18.90	13.37	18.63	2.57	2.31	0.16
BD8	19.07	13.48	18.91	2.57	2.33	0.15
BD9	18.96	13.40	18.84	2.57	2.31	0.15
BD10	18.85	13.33	18.77	2.57	2.30	0.15
BD11	18.48	13.07	18.22	2.57	2.29	0.15
BD12	18.60	13.15	18.65	2.57	2.30	0.13
BD13	18.52	13.10	18.39	2.57	2.29	0.15
BD14	18.62	13.17	18.44	2.57	2.32	0.15
BD15	19.07	13.48	19.15	2.57	2.32	0.13
BD16	19.16	13.55	19.17	2.57	2.32	0.13
BD17	19.04	13.46	19.11	2.57	2.29	0.13
BD18	19.09	13.50	19.04	2.57	2.31	0.14
Avg.	18.85	13.33	18.73	2.57	2.31	0.16

Table 3.2: *Spectrum and time series parameters for incident waves at WG1 location for 12 runs of WD test.*

Run	H_{mo} (cm)	H_{rms} (cm)	H_s (cm)	T_p (s)	T_s (s)	R
WD1	19.22	13.59	19.07	2.39	2.32	0.24
WD2	19.04	13.46	19.00	2.57	2.31	0.19
WD3	18.69	13.21	18.55	2.57	2.30	0.20
WD4	18.33	12.96	18.10	2.57	2.30	0.21
WD5	18.70	13.22	18.58	2.57	2.30	0.15
WD6	18.87	13.34	18.81	2.57	2.30	0.14
WD7	18.89	13.36	18.68	2.57	2.30	0.13
WD8	19.05	13.47	19.22	2.57	2.31	0.13
WD9	19.19	13.57	19.18	2.57	2.32	0.12
WD10	19.33	13.67	19.27	2.57	2.32	0.13
WD11	18.86	13.34	18.99	2.57	2.28	0.13
WD12	19.00	13.44	18.98	2.57	2.30	0.13
Avg.	18.93	13.39	18.87	2.55	2.31	0.16

Table 3.3: *Spectrum and time series parameters for incident waves at WG1 location for 15 runs of SD test.*

Run	H_{mo} (cm)	H_{rms} (cm)	H_s (cm)	T_p (s)	T_s (s)	R
SD1	18.34	12.97	18.21	2.57	2.29	0.19
SD2	18.58	13.14	18.37	2.57	2.32	0.20
SD3	19.10	13.50	18.82	2.57	2.31	0.19
SD4	19.00	13.44	18.89	2.57	2.33	0.20
SD5	19.11	13.52	18.80	2.57	2.31	0.18
SD6	19.13	13.53	18.97	2.57	2.31	0.17
SD7	18.87	13.34	18.73	2.57	2.27	0.15
SD8	19.12	13.52	19.22	2.57	2.30	0.16
SD9	19.00	13.44	19.03	2.57	2.31	0.13
SD10	19.10	13.50	18.95	2.57	2.31	0.14
SD11	19.01	13.44	18.97	2.57	2.30	0.13
SD12	18.63	13.18	18.62	2.57	2.29	0.14
SD13	18.88	13.35	19.04	2.57	2.31	0.13
SD14	18.81	13.30	18.80	2.57	2.31	0.14
SD15	19.04	13.47	19.04	2.57	2.29	0.15
Avg.	18.92	13.37	18.83	2.57	2.30	0.16

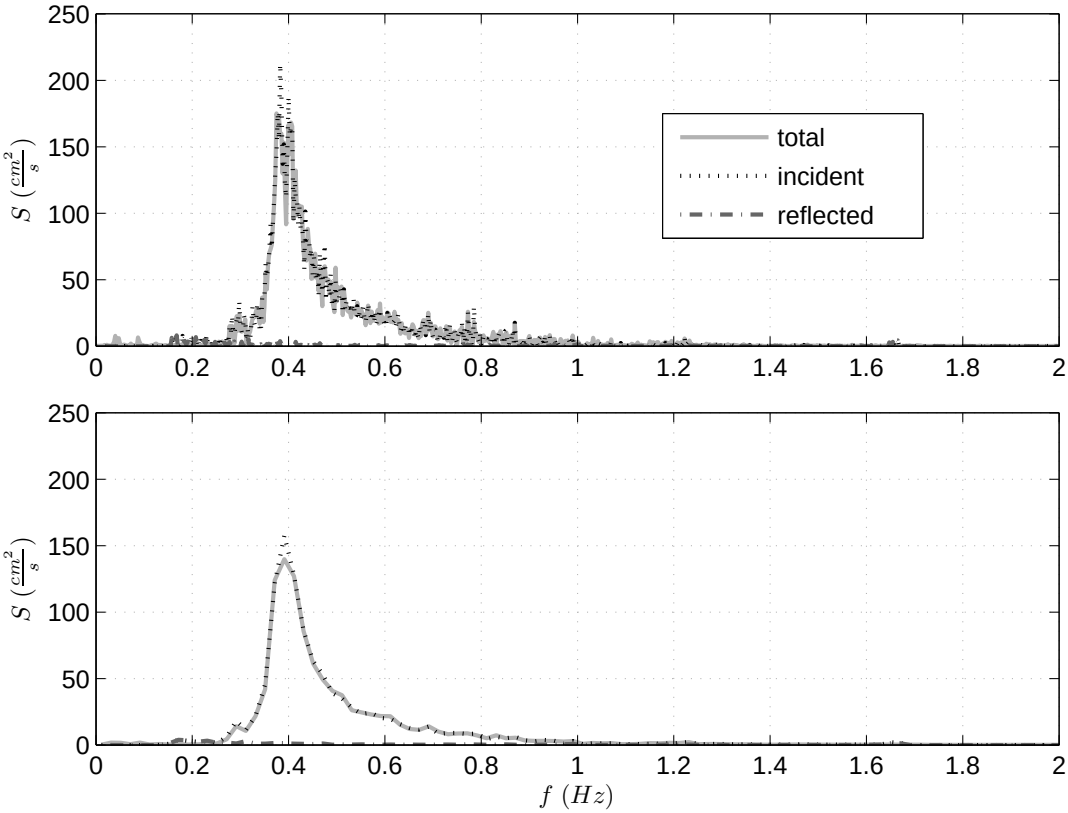

Figure 3.1: *Unsmoothed (top panel) and smoothed (bottom panel) offshore wave frequency spectra for run BD5. Incident and reflected wave signals have been calculated from the total signals obtained from WG1, WG2, and WG3.*

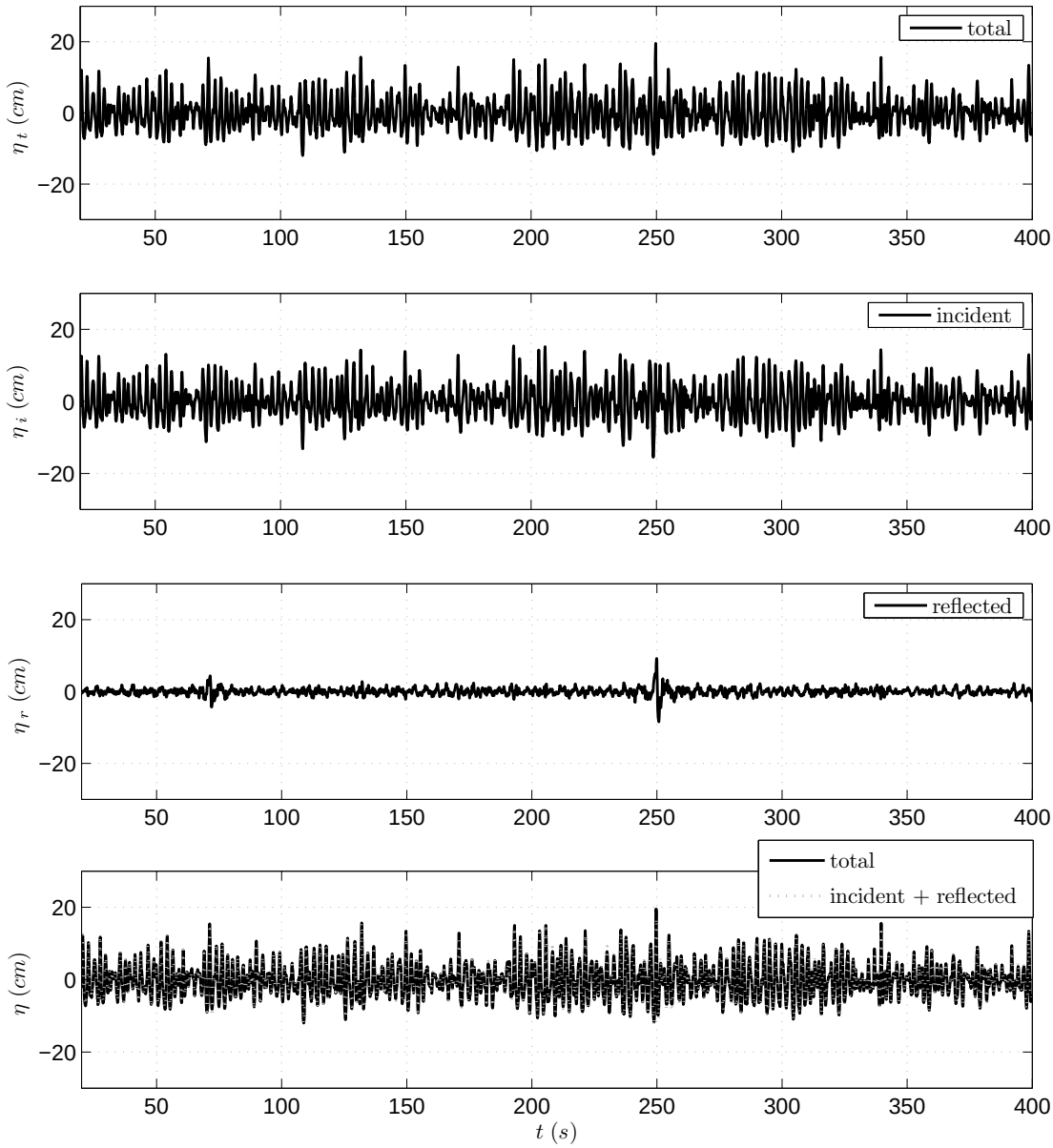

Figure 3.2: *Total, incident and reflected wave time series at WG1 location during run BD5. The first 20 s are truncated before the data analysis to eliminate ramp-up effects.*

The mean free surface elevation, $\overline{\eta}$, its standard deviation, σ_η, and the wet probability, P_w, are the statistical properties computed for all eight gauge locations. The overbar indicates time averaging during the wet duration which is the time a certain point on the bottom profile is submerged in water. The associated wet probability, P_w, indicates the likelihood of that point to be submerged in water at any given time during a run and is expressed as

$$P_w = \frac{J_{wet}}{J} \tag{3.1}$$

where J is the total number of data points in the recorded free surface elevation time series and J_{wet} represents the number of data points for which the gauge at that location is considered to be submerged in water. For cross-shore locations in the upper swash zone the water depth of the wave run-up can be very small which makes the determination of the exact wet duration and wet probability rather difficult since no common definition exists. A procedure for obtaining free surface elevation from wave gauges located in that region is proposed in the following.

In general, the free surface elevation at any cross-shore location is given by

$$\eta(t) = h(t) + z_b(t) \tag{3.2}$$

where the free surface elevation $\eta(t)$ and the bottom elevation $z_b(t)$ are in reference to $z = 0$ (SWL) and $h(t)$ is the time dependent local water depth ($h(t) \geq 0$). Equation (3.2) holds true at any cross-shore location. In the experiment the value of $\eta(t)$ at various cross-shore locations is obtained from the recorded wave gauge data but the analysis procedure depends on the location and classification of the respective gauge (Table 2.3). Wave gauges are considered to be free or buried corresponding to the way they are mounted with regards to the sandy bottom. Buried wave gauges allow for detection of small changes in free surface elevation above the changing bottom

as needed in the upper swash zone. The analysis procedure for the data from the free gauges (WG1-5) is a straightforward linear conversion from measured voltage to free surface elevation $\eta(t)$ with a zero reading at SWL. This procedure is the same for the buried gauges which remain completely submerged during the entire wave run (WG6-7). All submerged gauges yield wet probabilities of $P_w = 1$ for their respective cross-shore locations since $J_{wet} = J$ in (3.1).

For gauges classified as buried and exposed (only WG8 for the first 8, 4, and 4 runs of BD, WD, and SD, respectively) the analysis procedure is modified since several processes affect the recorded voltage time series. First, the zero reading before a wave run does not correspond to SWL but rather to a voltage recorded with the gauge buried in the wet sand of initial elevation z_{bi}. This reference level is easily changed to SWL by adding the known value of z_{bi} for each run to the measured free surface elevation. Second, the gauge encounters wet and dry periods depending on the wave uprush and the changing local bottom elevation $z_b(t)$. During a wet period the voltage signal yields the free surface elevation $\eta(t)$ directly. During dry periods the voltage drops to a level indicating $z_b(t)$ since the wet sand surface serves as a lower limit for the voltage reading and $h(t) = 0$ for the fine sand with very small seepage. This lower limit is a noisy voltage fluctuation of $\pm 1.5\,mm$ rather than a distinctive measure of the exact bottom elevation but it allows for approximation of the local bottom elevation during the dry period.

Hence, the crucial part of the analysis is the determination of the wet and dry periods. This is done in two steps. First, we partition each 380-s time series into 10-s (200-point) windows, each covering approximately four times the spectral peak period ($T_p = 2.6\,s$). After confirming with visual observation it is assumed that the buried wave gauge enters a dry period at least once during each 10-s window indicating a minimum voltage corresponding to $z_b(t)$. Since the above mentioned noisy voltage fluctuation of $\pm 1.5\,mm$ is observed during dry periods when the gauge

is buried in wet sand we simply include all data points within $3\,mm$ above the local minimum for each window in the dry period (J_{dry}) and the rest of the data points in the wet period (J_{wet}). In Figure 3.3 an example taken from the WG8 time series of run WD2 is shown where the minima of the 10-s window partitions are displayed as thick solid red lines and data points J_{wet} and J_{dry} are depicted as small black dots and hollow blue circles, respectively. The wet probability P_w in the intermittently wet and dry zone is then computed using (3.1).

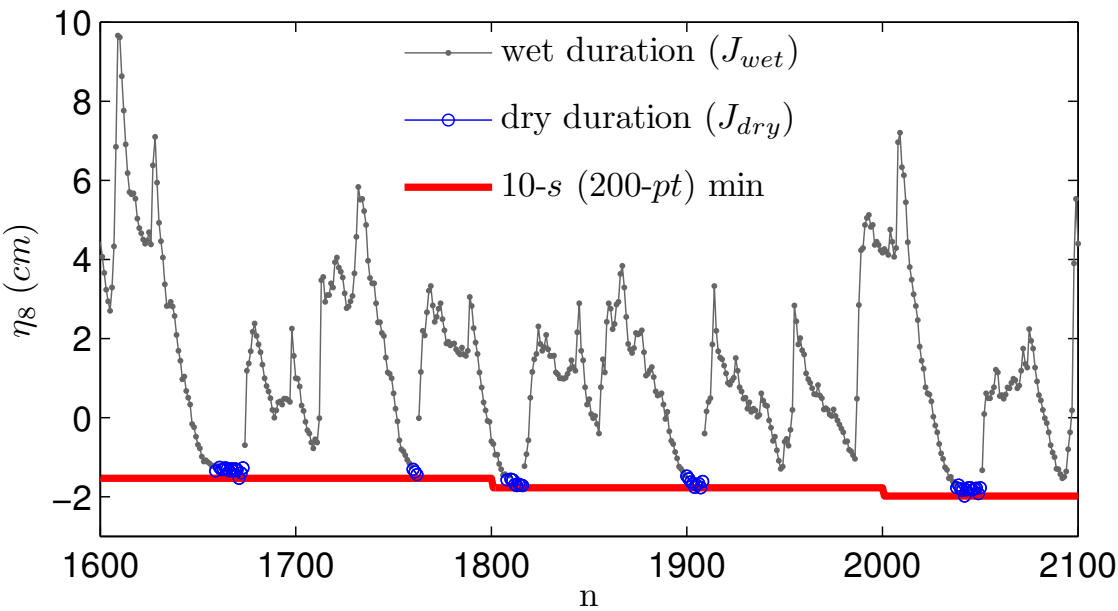

Figure 3.3: *Wet and dry periods for WG8 measurement during 500 point window ($n = 1600 - 2100$) of run WD2. This gauge above SWL was buried in the sand.*

Even though the initial and final bottom elevations z_{bi} and z_{bf} are measured manually before and after each wave run, respectively, z_{bf} is only used to confirm the local bottom elevation value obtained in the last window of the above time series analysis yielding good agreement within a $\pm 3\,mm$ error bound. It has to be noted that the statistical mean and standard deviation of the free surface elevation presented in Tables 3.4 through 3.9 refer to data points within the wet period only, to be consistent with the averaging procedure used in the model for the wet and

dry zone in CSHORE (Chapter 4). The mean free surface elevation $\overline{\eta}$ for each WG record is the setup ($\overline{\eta} > 0$) or setdown ($\overline{\eta} < 0$) with respect to SWL at that cross-shore location in the flume. Chapter 4 shows the cross-shore momentum equation including bottom shear stress.

In the present experiment setdown was consistently observed in all runs for WG1 through WG4 whereas WG6 through WG8 always showed setup. WG5 records mostly indicated setup except for a few runs with negative $\overline{\eta}$. At most, the mean free surface elevation, $\overline{\eta}$, deviated $\pm 5\,mm$ from SWL for WG1-7. Fluctuations between runs may be due to various reasons. Even though care was taken to always keep the SWL constant, slight variations on the order of $1\,mm$ at the beginning of a run as well as during a run may have been a factor. During runs with significant wave overtopping the recirculation system (Section 2.4.1) pumped water back into the flume to maintain a constant SWL. In addition, the WG accuracy is estimated to be on the order of $1\,mm$.

WG8 is located in the wave run-up dominated region which explains the large setup values, especially during the first few runs of a test when the bottom elevation was located above SWL.

Tables 3.7, 3.8, and 3.9 list the standard deviation, σ_η, at all WG locations for every run. σ_η is an indicator for wave height ($H_{mo} = 4\sigma_\eta$) and decreases after the waves break. This explains the significant drop in values between the locations of WG4 and WG5 since most waves have already broken before reaching WG5. In the region of the dune (WG8) σ_η is mostly related to the mean water depth above the local bottom and thus further decreased.

The wet probability according to (3.1) is tabulated in Table 3.10 for the WG8 location only since all other WG locations always have a wet probability of $P_w = 1$. Values below unity are computed using the procedure described above and need to be understood as approximate estimates based on the WG signal. The

Table 3.4: *Mean free surface elevation* $\overline{\eta}$ *(cm) at* 8 *wave gauge locations for* 18 *runs of BD test.*

Run	WG1	WG2	WG3	WG4	WG5	WG6	WG7	WG8
BD1	-0.18	-0.13	-0.28	-0.19	0.12	0.31	0.33	NA
BD2	-0.14	-0.14	-0.33	-0.18	0.16	0.30	0.35	3.63
BD3	-0.15	-0.16	-0.34	-0.22	0.13	0.30	0.35	3.74
BD4	-0.13	-0.13	-0.30	-0.19	0.17	0.30	0.36	3.68
BD5	-0.18	-0.14	-0.33	-0.21	0.19	0.28	0.34	3.09
BD6	-0.14	-0.14	-0.30	-0.19	0.11	0.31	0.34	3.07
BD7	-0.19	-0.17	-0.33	-0.24	0.10	0.23	0.30	2.80
BD8	-0.22	-0.22	-0.37	-0.32	0.10	0.19	0.32	2.01
BD9	-0.35	-0.36	-0.41	-0.38	-0.05	0.08	0.10	2.01
BD10	-0.30	-0.28	-0.46	-0.33	0.08	0.17	0.22	1.18
BD11	-0.29	-0.28	-0.49	-0.34	0.04	0.14	0.18	0.84
BD12	-0.19	-0.15	-0.34	-0.23	0.22	0.25	0.31	0.90
BD13	-0.11	-0.09	-0.24	-0.17	0.19	0.33	0.37	0.89
BD14	-0.18	-0.14	-0.34	-0.27	0.15	0.31	0.33	0.80
BD15	-0.09	-0.06	-0.20	-0.17	0.30	0.35	0.41	0.84
BD16	-0.14	-0.13	-0.27	-0.21	0.32	0.32	0.36	0.76
BD17	-0.30	-0.27	-0.40	-0.33	0.14	0.26	0.27	0.60
BD18	-0.17	-0.15	-0.28	-0.22	0.08	0.31	0.36	0.58

NA: not available due to WG8 failure.

Table 3.5: *Mean free surface elevation* $\overline{\eta}$ *(cm) at* 8 *wave gauge locations for* 12 *runs of WD test.*

Run	WG1	WG2	WG3	WG4	WG5	WG6	WG7	WG8
WD1	-0.16	-0.16	-0.27	-0.22	-0.14	0.25	0.50	10.10
WD2	-0.10	-0.07	-0.21	-0.20	0.22	0.31	0.44	1.71
WD3	-0.15	-0.11	-0.25	-0.26	-0.26	0.30	0.36	2.10
WD4	-0.20	-0.16	-0.29	-0.28	0.17	0.27	0.29	1.38
WD5	-0.27	-0.24	-0.37	-0.35	0.06	0.20	0.20	1.34
WD6	-0.21	-0.20	-0.28	-0.28	0.08	0.23	0.29	0.97
WD7	-0.12	-0.08	-0.20	-0.22	0.18	0.32	0.39	0.92
WD8	-0.11	-0.09	-0.19	-0.21	0.18	0.33	0.42	0.85
WD9	-0.33	-0.30	-0.45	-0.35	0.02	0.19	0.23	0.65
WD10	-0.24	-0.18	-0.31	-0.29	0.09	0.24	0.32	0.60
WD11	-0.17	-0.12	-0.23	-0.23	0.17	0.33	0.35	0.50
WD12	-0.15	-0.13	-0.21	-0.25	0.15	0.30	0.32	0.52

Table 3.6: *Mean free surface elevation* $\overline{\eta}$ *(cm) at* 8 *wave gauge locations for* 15 *runs of SD test.*

Run	WG1	WG2	WG3	WG4	WG5	WG6	WG7	WG8
SD1	-0.14	-0.13	-0.21	-0.28	0.14	0.35	0.33	2.25
SD2	-0.11	-0.09	-0.22	-0.21	0.18	0.32	0.27	1.64
SD3	-0.11	-0.10	-0.22	-0.20	0.19	0.37	0.24	1.62
SD4	-0.15	-0.13	-0.24	-0.23	0.13	0.35	0.22	1.39
SD5	-0.19	-0.15	-0.27	-0.26	0.11	0.33	0.24	1.78
SD6	-0.27	-0.26	-0.36	-0.32	0.01	0.22	0.17	1.40
SD7	-0.14	-0.17	-0.27	-0.28	0.12	0.26	0.21	1.18
SD8	-0.21	-0.20	-0.30	-0.27	0.11	0.19	0.25	1.00
SD9	-0.25	-0.24	-0.30	-0.31	0.05	0.23	0.23	0.95
SD10	-0.21	-0.18	-0.27	-0.26	0.12	0.29	0.27	0.94
SD11	-0.02	0.01	-0.07	-0.09	0.24	0.43	0.36	1.02
SD12	-0.14	-0.12	-0.20	-0.29	0.09	0.26	0.21	0.78
SD13	-0.12	-0.08	-0.15	-0.20	0.16	0.34	0.33	1.01
SD14	-0.20	-0.17	-0.27	-0.27	0.15	0.28	0.34	0.70
SD15	-0.06	-0.06	-0.15	-0.14	0.26	0.38	0.41	0.76

Table 3.7: *Standard deviation σ_η (cm) of the free surface elevation at 8 wave gauge locations for 18 runs of BD test.*

Run	WG1	WG2	WG3	WG4	WG5	WG6	WG7	WG8
BD1	4.58	4.59	4.76	4.67	3.58	3.11	3.27	NA
BD2	4.57	4.61	4.97	4.75	3.67	3.17	3.30	1.48
BD3	4.61	4.64	4.96	4.77	3.68	3.16	3.33	1.47
BD4	4.60	4.61	4.76	4.75	3.61	3.18	3.30	1.50
BD5	4.64	4.67	4.80	4.78	3.64	3.16	3.29	1.54
BD6	4.61	4.62	4.78	4.76	3.62	3.15	3.26	1.53
BD7	4.58	4.59	4.90	4.52	3.61	3.13	3.21	1.50
BD8	4.60	4.62	4.93	4.53	3.59	3.09	3.14	1.54
BD9	4.56	4.61	4.88	4.66	3.53	3.04	3.00	2.27
BD10	4.59	4.64	4.82	4.66	3.55	3.01	3.00	2.51
BD11	4.46	4.51	4.76	4.56	3.53	2.93	3.04	2.12
BD12	4.48	4.53	4.76	4.55	3.45	2.92	3.00	2.12
BD13	4.51	4.55	4.71	4.59	3.45	2.98	2.99	2.23
BD14	4.53	4.56	4.74	4.61	3.46	2.96	3.02	2.28
BD15	4.52	4.55	4.94	4.58	3.56	2.97	3.01	2.32
BD16	4.55	4.58	4.98	4.58	3.51	2.96	3.03	2.33
BD17	4.53	4.53	4.96	4.56	3.49	2.95	3.01	2.35
BD18	4.53	4.53	4.98	4.56	3.37	2.95	3.01	2.35

NA: not available due to WG8 failure.

Table 3.8: *Standard deviation σ_η (cm) of the free surface elevation at 8 wave gauge locations for 12 runs of WD test.*

Run	WG1	WG2	WG3	WG4	WG5	WG6	WG7	WG8
WD1	4.67	4.67	5.10	4.81	3.57	3.29	3.47	3.59
WD2	4.59	4.60	5.01	4.66	3.54	3.22	3.17	1.94
WD3	4.59	4.59	4.85	4.68	3.20	3.24	3.20	1.94
WD4	4.59	4.60	4.83	4.65	3.56	3.15	3.07	1.95
WD5	4.57	4.60	4.80	4.57	3.34	3.06	2.98	2.26
WD6	4.53	4.57	4.92	4.56	3.36	2.98	2.97	2.29
WD7	4.54	4.57	4.90	4.54	3.36	2.97	3.04	2.26
WD8	4.58	4.58	4.92	4.60	3.29	2.97	3.02	2.24
WD9	4.59	4.61	4.98	4.70	3.39	3.01	3.07	2.40
WD10	4.63	4.65	5.02	4.69	3.32	3.02	3.08	2.43
WD11	4.52	4.54	4.89	4.55	3.34	3.00	3.08	2.43
WD12	4.56	4.58	4.93	4.57	3.40	2.99	3.09	2.46

Table 3.9: *Standard deviation σ_η (cm) of the free surface elevation at 8 wave gauge locations for 15 runs of SD test.*

Run	WG1	WG2	WG3	WG4	WG5	WG6	WG7	WG8
SD1	4.50	4.48	4.66	4.58	3.44	3.14	3.37	1.91
SD2	4.57	4.54	4.71	4.63	3.38	3.11	3.28	1.91
SD3	4.66	4.66	4.98	4.75	3.50	3.17	3.34	1.88
SD4	4.65	4.65	4.95	4.72	3.31	3.15	3.29	1.91
SD5	4.65	4.67	4.98	4.75	3.45	3.17	3.30	2.03
SD6	4.65	4.67	4.97	4.69	3.40	3.08	3.21	2.10
SD7	4.55	4.57	4.93	4.62	3.43	3.08	3.23	2.17
SD8	4.60	4.62	4.97	4.67	3.21	3.03	3.21	2.13
SD9	4.57	4.57	4.93	4.58	3.28	3.02	3.12	2.10
SD10	4.59	4.61	4.95	4.63	3.36	3.04	3.15	2.09
SD11	4.58	4.58	4.91	4.62	3.33	3.06	3.13	2.15
SD12	4.49	4.49	4.83	4.53	3.23	3.04	3.10	2.22
SD13	4.55	4.55	4.89	4.56	3.32	3.03	3.10	2.34
SD14	4.52	4.53	4.89	4.59	3.32	3.00	3.09	2.38
SD15	4.60	4.61	4.96	4.65	3.41	3.00	3.13	2.36

lowest estimated value is $P_w = 0.79$ (BD3) which still suggests a 79% likelihood of submergence at any given time in that run. These high wet probabilities are due to the fact that the location of WG8 was close to the intersection between the bottom profile and SWL.

Table 3.10: *Wet probability P_w at WG8 location for all tests.*

Run	P_w	Run	P_w	Run	P_w
BD1	NA	WD1	0.91	SD1	0.88
BD2	0.81	WD2	0.88	SD2	0.86
BD3	0.79	WD3	0.87	SD3	0.86
BD4	0.81	WD4	0.88	SD4	0.87
BD5	0.82	WD5	1.00	SD5	1.00
BD6	0.82	WD6	1.00	SD6	1.00
BD7	0.83	WD7	1.00	SD7	1.00
BD8	0.83	WD8	1.00	SD8	1.00
BD9	1.00	WD9	1.00	SD9	1.00
BD10	1.00	WD10	1.00	SD10	1.00
BD11	1.00	WD11	1.00	SD11	1.00
BD12	1.00	WD12	1.00	SD12	1.00
BD13	1.00			SD13	1.00
BD14	1.00			SD14	1.00
BD15	1.00			SD15	1.00
BD16	1.00				
BD17	1.00				
BD18	1.00				

NA: not available due to WG8 failure.

3.1.2 Velocity

Fluid velocity data is recorded by two ADV sensors co-located with WG5 and WG7, respectively. Their respective sampling volumes are positioned 2/3 of the local mean water depth d below SWL at the beginning of each run. This elevation above the local bottom guarantees for measurements well outside the bottom boundary layer with enough clearance to prevent scouring caused by the probe tip. In addition, the distance from the free surface minimizes the negative effects of entrained air bubbles on the measurements. Even though the vertical distribution of the instantaneous velocities is influenced by many factors like orbital wave motion, undertow current, and turbulent velocities, the chosen measurement location is assumed to give a fairly good representation of the depth-averaged mean velocities.

ADV1 at the WG5 location is a 3D instrument with downward pointing probe tips measuring velocities in the cross-shore (u), alongshore (v), and vertical (w) directions in a sampling volume 5 *cm* below the probe tips (Section 2.2.2). ADV2 at the WG7 location is a 2D instrument with sideways pointing probe tips which allows for measurement of the two velocity components u and v at the location of the sampling volume. Tables 3.11 through 3.13 summarize the mean velocities $\overline{u}$, $\overline{v}$, and $\overline{w}$ and the standard deviations σ_u, σ_v, and σ_w for the test series BD, WD, and SD.

It has to be noted that the cross-shore velocity component u is dominant as expected in this two-dimensional wave flume experiment. The mean cross-shore velocity $\overline{u}$ is always negative at the two measurement locations indicating the presence of an offshore return (undertow) current as observed in previous velocity measurements in the same wave flume. Kobayashi et al. (2005) showed vertical distributions of the measured mean cross-shore velocity $\overline{u}$ at various locations under similar conditions. The measured vertical variations of $\overline{u}$ were not very large under the irregular waves in their experiment. In the present experiment, the measured values for $\overline{u}$

range from -6.72 to $-4.28\,cm/s$ with standard deviations, σ_u, between 17.40 and $20.96\,cm/s$ at the cross-shore location of ADV1 ($x = 12.88\,m$). The data collected at the ADV2 location ($x = 17.02\,m$) yields minimum and maximum values of $\overline{u}$ of -5.83 and $-2.88\,cm/s$, respectively, with σ_u ranging from 18.30 to $25.02\,cm/s$. The values for the longshore and vertical components are one order-or-magnitude smaller than the cross-shore components (Tables 3.11, 3.12, and 3.13).

Table 3.11: *Velocity (cm/s) parameters measured at $z = -2/3\ d$ for 18 runs of BD test.*

	ADV1 (3D)						ADV2 (2D)			
Run	$\overline{u}$	σ_u	$\overline{v}$	σ_v	$\overline{w}$	σ_w	$\overline{u}$	σ_u	$\overline{v}$	σ_v
BD1	-6.31	19.64	-0.22	4.25	-0.36	4.02	-4.79	18.99	0.52	3.63
BD2	-6.17	20.04	-0.31	4.40	-0.47	4.46	-4.62	19.83	0.39	3.30
BD3	-6.32	20.29	-1.36	4.39	-0.54	4.45	-4.41	20.29	-0.32	3.56
BD4	-6.63	20.05	-0.03	4.31	-0.32	4.34	-4.35	20.59	0.37	3.64
BD5	-6.00	19.93	-0.80	4.10	-0.79	4.35	-4.61	20.98	0.33	3.38
BD6	-6.38	20.00	-0.38	4.34	-0.60	4.51	-4.05	20.99	-0.06	3.43
BD7	-5.19	19.92	-0.28	4.32	-0.80	4.22	-3.82	21.23	0.14	3.55
BD8	-5.92	19.39	-0.38	4.61	-0.47	4.36	-4.25	21.00	-0.05	3.41
BD9	-5.29	19.06	-0.02	4.34	-0.47	4.32	-3.87	20.64	0.36	3.29
BD10	-6.17	18.78	-0.54	3.90	-0.30	4.21	-4.02	20.01	0.30	3.04
BD11	-4.87	18.77	-0.29	4.31	-0.43	4.67	-3.25	19.96	0.61	2.97
BD12	-5.26	18.71	0.68	4.28	-0.44	4.23	-3.75	19.61	0.37	2.93
BD13	-5.24	18.60	0.54	4.20	-0.35	4.04	-3.92	19.77	0.68	2.96
BD14	-5.51	18.62	-0.38	4.55	-0.77	4.77	-4.93	19.27	0.17	2.65
BD15	-5.82	18.72	-0.47	4.11	-0.42	4.29	-3.53	19.31	0.17	3.00
BD16	-6.06	18.79	-0.20	4.12	-0.69	4.22	-3.28	19.30	0.15	2.85
BD17	-5.49	18.50	-0.52	3.91	-0.77	3.88	-3.83	18.85	0.46	2.76
BD18	-5.70	18.61	0.39	4.28	-0.65	4.29	-3.12	19.24	0.07	2.91

Table 3.12: *Velocity (cm/s) parameters measured at $z = -2/3\ d$ for 12 runs of WD test.*

	ADV1 (3D)						ADV2 (2D)			
Run	$\overline{u}$	σ_u	$\overline{v}$	σ_v	$\overline{w}$	σ_w	$\overline{u}$	σ_u	$\overline{v}$	σ_v
WD1	-6.71	20.96	-0.06	4.46	-0.43	4.63	-3.45	19.06	-0.02	3.26
WD2	-6.72	19.60	0.17	4.25	-0.08	4.36	-3.79	19.27	0.67	3.00
WD3	-6.05	19.87	-0.06	3.95	-0.24	4.14	-4.13	19.57	0.48	3.17
WD4	-4.85	19.43	0.36	4.27	-0.65	4.51	-4.78	19.69	0.90	3.11
WD5	-6.02	18.99	-0.69	3.85	-0.52	4.10	-3.80	19.65	0.71	3.13
WD6	-5.54	18.26	-0.10	4.18	-0.43	4.20	-3.02	19.38	0.41	2.86
WD7	-5.73	18.19	-0.76	3.77	-0.60	3.96	-3.51	18.68	0.05	2.63
WD8	-5.13	18.12	-0.02	4.33	-0.65	4.29	-2.88	18.52	0.39	2.73
WD9	-5.28	17.92	-0.44	3.86	-0.54	4.28	-3.37	18.30	0.24	2.71
WD10	-5.14	18.13	-0.21	3.83	-0.63	4.15	-4.09	18.53	0.10	2.55
WD11	-5.34	17.94	-0.20	4.36	-0.54	4.40	-3.65	18.65	0.50	2.74
WD12	-6.24	18.16	-0.75	3.80	-0.31	3.70	-4.34	18.77	0.02	2.83

Table 3.13: *Velocity (cm/s) parameters measured at $z = -2/3\ d$ for 15 runs of SD test.*

	ADV1 (3D)						ADV2 (2D)			
Run	$\overline{u}$	σ_u	$\overline{v}$	σ_v	$\overline{w}$	σ_w	$\overline{u}$	σ_u	$\overline{v}$	σ_v
SD1	-4.78	18.99	-0.50	4.10	-0.64	4.12	-5.26	24.61	0.04	3.23
SD2	-5.29	18.96	-0.31	4.24	-0.84	4.22	-5.65	24.57	0.63	3.67
SD3	-5.89	18.86	-0.29	4.04	-0.56	3.99	-5.67	24.95	0.87	3.35
SD4	-5.68	18.95	-0.91	4.11	-0.13	4.24	-5.83	25.02	0.44	3.31
SD5	-5.62	18.72	-0.45	4.01	-0.73	4.38	-4.75	24.14	0.69	3.54
SD6	-5.53	18.19	-0.11	4.18	-0.48	4.43	-4.67	23.22	0.79	3.47
SD7	-5.92	17.63	-0.50	3.57	-0.57	3.89	-4.20	21.78	-0.03	3.16
SD8	-5.97	17.90	-0.07	3.70	-0.49	3.70	-3.78	20.93	0.41	2.80
SD9	-6.06	17.40	-0.12	3.67	-0.59	3.71	-4.11	20.68	0.12	2.92
SD10	-5.11	17.77	0.04	3.88	-0.28	3.89	-3.74	20.35	-0.01	2.73
SD11	-4.28	17.47	-0.26	3.81	-0.57	3.79	-4.29	20.30	0.39	2.77
SD12	-4.28	17.49	0.39	3.97	-0.40	3.59	-4.03	20.35	0.40	2.68
SD13	-4.55	17.70	0.17	3.82	-0.57	4.24	-3.98	20.01	0.32	2.71
SD14	-5.58	17.51	-0.10	3.41	-0.71	3.59	-3.87	19.64	0.51	2.69
SD15	-4.29	17.60	0.11	3.95	-0.93	4.27	-3.95	19.85	0.10	2.62

3.2 Morphology

For the analysis of the sand bottom evolution, profile scans obtained from the laser line scanner system and the three acoustic sensors are reduced to 2D coordinates (x and z) using the longshore average of the measured data for the $115\,cm$ wide flume. The x-axis is set along the flume centerline and has its origin at the location of WG1 with the vertical coordinate z positive upward above SWL. Examples of 3D laser scans before the reduction to 2D profiles are shown in Figure 3.4 where the measured initial profile, the profile after the first run, and the profile after the last run are shown for the BD, WD, and SD test series, respectively. The height and cross-shore length of the ripples in Figure 3.4 are of the order of $1\,cm$ and $7\,cm$, respectively.

3.2.1 Profile Evolution

Profiles were scanned by laser before and after each 400-s wave run from $x = 6\,m$ all the way to the overwash collection tub (Section 2.3). Since only minor changes occurred in the remaining portion of the offshore profile, this part was only scanned before and after every other wave run using acoustic profiling. Figures 3.5, 3.6, and 3.7 depict the evolution of the measured beach profiles for all three tests in the region of major profile change ($x = 16.0 - 19.9\,m$). Gray scales are used to show the time dependent progression of the profile change from the initial (light gray) to the final scan (black).

The progression of the observed nearshore profile evolution in all three tests followed a similar pattern. Initial profile adjustment due to the attacking waves changed the rather artificial foredune geometry by eroding a significant portion of the dune. The eroded material was carried offshore to form a more gently-sloping nearshore profile with a smooth terrace. This initial profile adjustment occurred very quickly during the first 400-s run in each test but the observed profile changes were very prominent, especially for the WD test, as shown in Figures 3.4 through

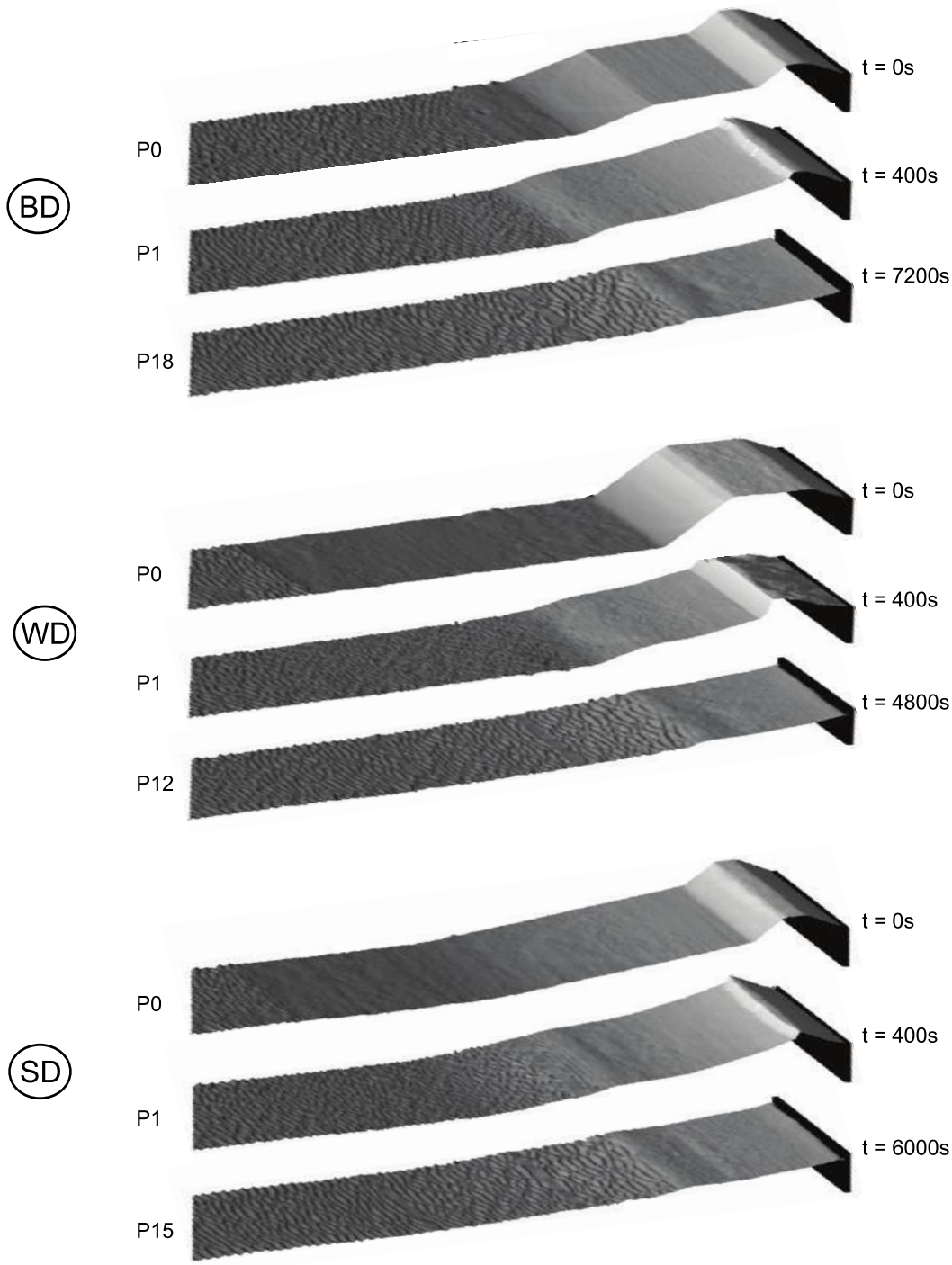

Figure 3.4: *3D images of scanned profiles before the first run, after the first run, and after the last run for BD, WD, and SD tests.*

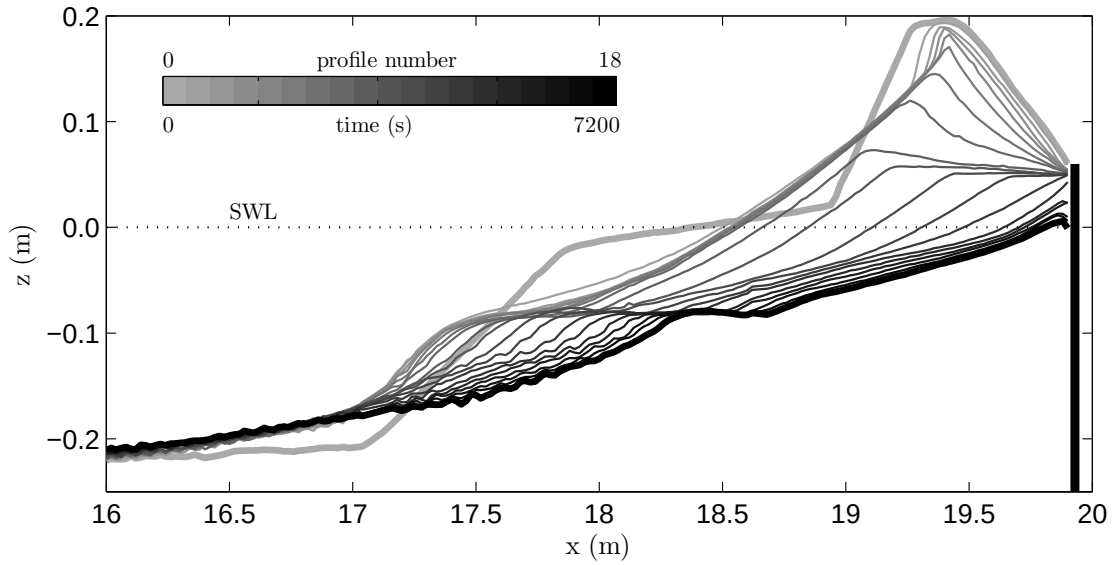

Figure 3.5: *Evolution of* 19 *measured profiles for runs BD1 through BD18. The gray scale shades indicate the measured profile number* $(0-18)$ *and the corresponding time level* $(0-7200\,s)$ *ranging from light gray (initial profile at time zero before BD1) to black (final profile after BD18).*

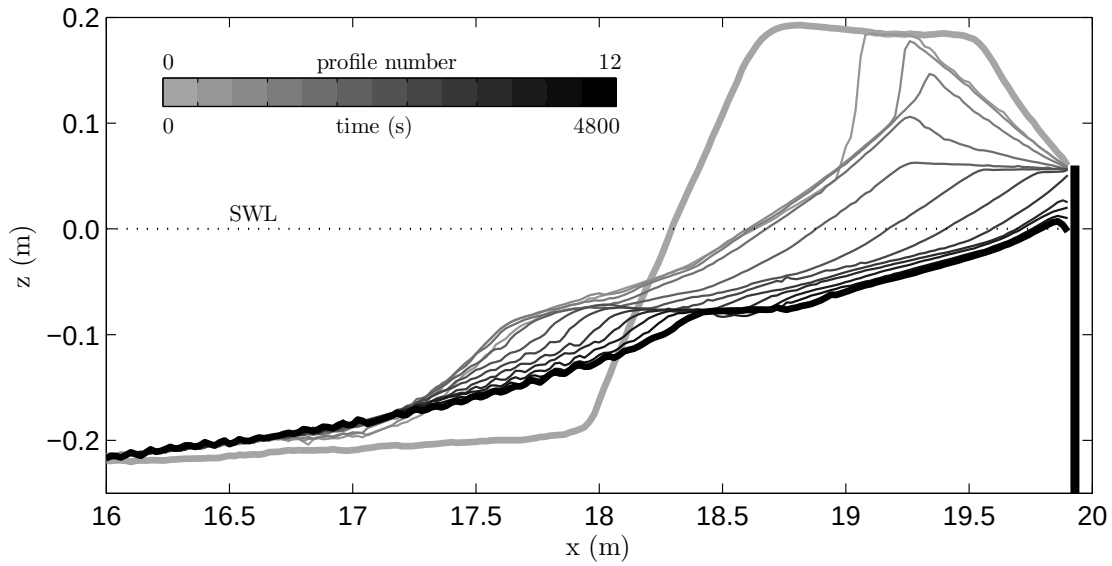

Figure 3.6: *Evolution of* 13 *measured profiles for runs WD1 through WD12. The gray scale shades indicate the measured profile number* $(0-12)$ *and the corresponding time level* $(0-4800\,s)$ *ranging from light gray (initial profile at time zero before WD1) to black (final profile after WD12).*

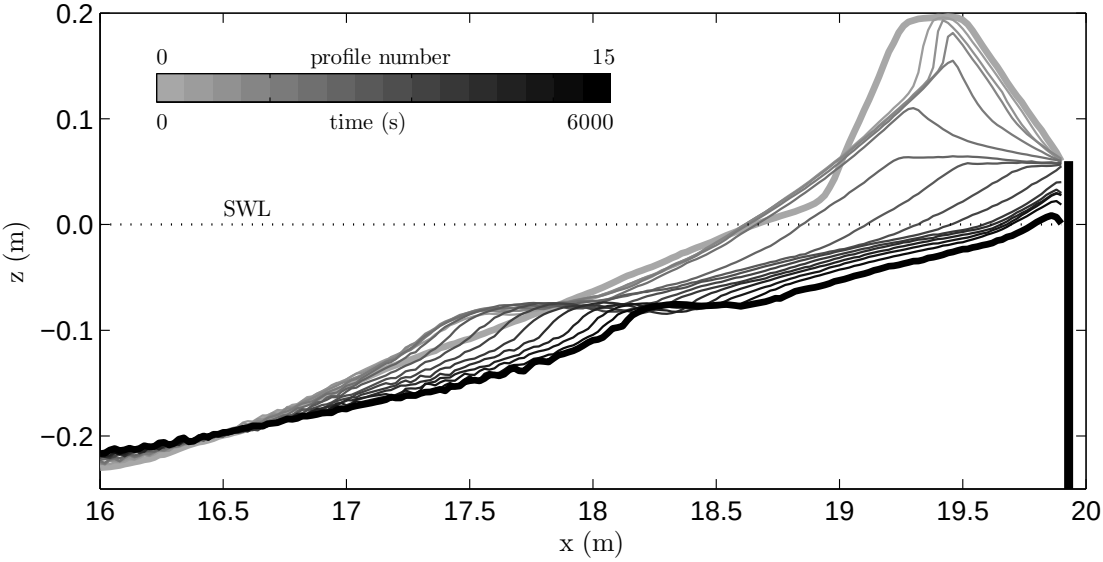

Figure 3.7: *Evolution of* 16 *measured profiles for runs SD1 through SD15. The gray scale shades indicate the measured profile number* $(0 - 15)$ *and the corresponding time level* $(0 - 6000\,s)$ *ranging from light gray (initial profile at time zero before SD1) to black (final profile after SD15).*

3.7. Scarping of the dune face occurred but the highest waves already overtopped the dune and created overwash. Except for the WD test, only minor backdune erosion occurred during the first run.

The initial profile adjustment was followed by the lowering and subsequent destruction of the entire dune leaving only a horizontal beach platform of approximately 80 *cm* length in front of the vertical wall at the level of the wall's crest. During the lowering process, scarping and slumping at the dune face increased and moved the dune crest further onshore while lowering its height at the same time. This onshore migration of the dune crest was then reversed because increased backdune erosion due to increased wave overtopping resulted in apparent offshore migration of the dune crest as the lowering process continued. Eventually, the dune was leveled completely to form the above mentioned horizontal beach platform. This platform was subsequently eroded entirely leaving only a concave nearshore beach profile up

to the crest of the vertical wall. In addition, the terrace feature which formed during the initial profile adjustment gradually moved further onshore as its seaward face continued to become gentler.

Finally, the entire concave profile in front of the vertical wall was lowered as erosion and overwash continued due to wave overtopping of the vertical wall. All three test series ended when the wall was exposed down to the still water level (SWL) which means that the top 6 cm of the vertical wall were visible after the last run of each test.

Failure and complete destruction of the dune in this experiment was intentional to observe the resilience of different dune geometries to erosion and subsequent destruction by wave induced overwash. The three tests show that the mode of dune failure is in fact related to the initial geometric composition of the dune and berm or sloping beach in addition to the dune crest height and the volume of sand contained in the dune. This is because the dune and beach profiles affect wave runup and overtopping. It should be noted that the presence of the vertical wall must have reduced the destruction time of the dune before the wall exposure because sediment transported landward of the dune is normally deposited and may reduce subsequent landward sediment transport.

The dune destruction time was noticeably longer for the BD test than for the WD and SD tests because the berm reduced wave runup on the dune. The sand volume of the protective berm feature in the initial BD profile was completely incorporated into a wide dune for the initial WD profile. This allowed the incoming waves to directly attack the dune face because the depth at the toe of the dune was larger than the incident root-mean square wave height. The dune failure during the WD test was more sudden than that of the BD test. After runs BD9 and WD5 the respective dunes were flattened out completely. The BD geometry resisted the erosion due to wave runup and overwash nearly twice as long. Hence, the BD mode

of dune failure had a more ductile character whereas the WD mode of dune failure was more brittle.

Profile change results from the SD test fell somewhere in between which may be explained by the effect of the sloped beach in front of the dune on the incoming waves. Although the slope caused some wave breaking it was not as effective as the berm in the BD test. The sloping beach allowed wave uprush to reach the dune face with more intensity, leading to much faster reduction of dune width and crest height than for the case including a berm. In addition, the underwater profile changes during the initial profile adjustment were less for the SD test and did not reduce wave action on the dune face.

It needs to be stated that the present experiment deals with the dune overwash during the peak of a storm surge without regard to the profile adjustment before the storm peak. If the storm peak is reached slowly, the different dune geometries may not have resulted in the noticeable difference of the dune destruction time due to the profile adjustment before the storm peak.

3.2.2 Erosion and Deposition

Comparing beach profiles at different time levels reveals areas of erosion and deposition caused by net sediment transport. These profile changes are quantified in the following to complement the visual description of the morphological processes (Section 3.2.1) reshaping the dune profile over the course of a test. The analysis is limited to the region of profile change (active zone) encompassing the dune and berm up to a certain offshore limit beyond which the observed bed elevation changes are only minor and affect the sediment volume balance very little. The exact cross-shore location of the offshore limit is somewhat arbitrary and has been chosen in accordance with a sensitivity analysis of the computed volumetric changes. The water depth at the offshore integration limit is selected to be on the order of the

initial dune crest elevation above SWL and is also close to the average of the spectral significant wave height H_{mo} during a test.

The volumetric changes are expressed per unit width and are obtained by integrating the difference between two profiles measured at different time levels over the entire active zone corresponding to the cross-shore limit plotted in Figures 3.5 to 3.7. Cumulative volume changes per unit width are computed with respect to the initial bottom profile $z_{bi} = z_b(t = 0)$ for each test. Eroded volume V_e, deposited volume V_d, and total volume change V_c are calculated by numerical trapezoidal integration between integration limits $x_t = 16.0\,m$ and $x_e = 19.9\,m$ (Tables 3.14 - 3.16) where x_t is the offshore limit of significant profile change and x_e is the end point of profile measurements and the location of the vertical wall. Mathematically, the eroded volume in the entire active zone is

$$V_e(t) = \int_{x_t}^{x_e} \left[\Delta z\,(t,x)\right] dx \qquad \begin{cases} \Delta z & = z_{bi} - z_b \quad \text{if } z_{bi} > z_b \\ \Delta z & = 0 \qquad\qquad \text{if } z_{bi} \leq z_b \end{cases} \tag{3.3}$$

which is always positive or equal to zero. This sign convention for eroded volume has been chosen to facilitate intuitive comparison to collected overwash volume. In turn, the deposited volume in the entire active zone is

$$V_d(t) = \int_{x_t}^{x_e} \left[\Delta z\,(t,x)\right] dx \qquad \begin{cases} \Delta z & = 0 \qquad\qquad \text{if } z_{bi} \geq z_b \\ \Delta z & = z_{bi} - z_b \quad \text{if } z_{bi} < z_b \end{cases} \tag{3.4}$$

which is always negative or equal to zero. The sum of (3.3) and (3.4) gives the volume change in the zone of $x = 16.0 - 19.9\ m$

$$V_c(t) = V_e(t) + V_d(t) \tag{3.5}$$

which is positive for net erosion and negative for net deposition. It has to be noted that all values of sand volume computed from profile changes include a void portion associated with the porosity $n_p = 0.4$ of the sediment used in the experiment.

Table 3.14: *Profile sand volume changes (cm^2) for 18 runs of BD test.*

	Cumulative			Individual Run		
Run	V_e	V_d	V_c	ΔV_e	ΔV_d	ΔV_c
BD1	325	-469	-144	325	-469	-144
BD2	448	-421	27	123	48	171
BD3	491	-430	61	43	-9	34
BD4	540	-427	113	49	3	52
BD5	609	-411	198	69	16	85
BD6	727	-388	338	118	23	140
BD7	887	-362	525	160	26	187
BD8	1171	-268	903	283	94	378
BD9	1428	-231	1197	258	37	295
BD10	1777	-231	1545	348	0	348
BD11	2052	-225	1827	276	6	282
BD12	2285	-220	2065	233	5	238
BD13	2471	-216	2256	186	5	190
BD14	2605	-213	2392	134	3	137
BD15	2696	-219	2477	91	-6	84
BD16	2794	-220	2574	98	-1	97
BD17	2875	-225	2650	81	-5	76
BD18	2978	-218	2760	103	7	110

Units are cm^2 because volume (cm^3) is given per unit width (cm).
The offshore integration limit $x_t = 16\,m$ with average $z_b(x_t) = -0.22\,m$.

In addition to the cumulative values of eroded volume V_e, deposited volume V_d and their sum V_c, the changes that occurred in each individual 400-s run are also listed in Tables 3.14 - 3.16 where the incremental volumes ΔV_e, ΔV_d, and ΔV_c are

Table 3.15: *Profile sand volume changes (cm^2) for 12 runs of WD test.*

	Cumulative			Individual Run		
Run	V_e	V_d	V_c	ΔV_e	ΔV_d	ΔV_c
WD1	1196	-894	302	1196	-894	302
WD2	1363	-954	409	167	-60	107
WD3	1513	-961	553	150	-7	144
WD4	1760	-952	809	247	9	256
WD5	2165	-917	1248	404	35	439
WD6	2525	-852	1673	361	64	425
WD7	2773	-803	1971	248	50	298
WD8	2965	-730	2236	192	73	265
WD9	3075	-679	2396	109	51	160
WD10	3144	-635	2509	69	44	113
WD11	3220	-602	2618	76	33	109
WD12	3297	-570	2727	77	32	109

Units are cm^2 because volume (cm^3) is given per unit width (cm).
The offshore integration limit $x_t = 16\,m$ with average $z_b(x_t) = -0.22\,m$.

Table 3.16: *Profile sand volume changes (cm^2) for 15 runs of SD test.*

	Cumulative			Individual Run		
Run	V_e	V_d	V_c	ΔV_e	ΔV_d	ΔV_c
SD1	223	-188	35	223	-188	35
SD2	294	-205	89	71	-17	54
SD3	339	-201	138	45	4	49
SD4	452	-185	267	113	16	129
SD5	671	-157	514	219	28	247
SD6	1037	-116	921	367	40	407
SD7	1353	-95	1258	315	21	337
SD8	1599	-65	1534	247	29	276
SD9	1793	-41	1752	194	24	218
SD10	1961	-36	1926	168	06	174
SD11	2073	-39	2034	112	-3	108
SD12	2193	-38	2155	121	0	121
SD13	2292	-44	2247	98	-6	92
SD14	2423	-39	2384	132	5	137
SD15	2581	-48	2533	158	-9	149

Units are cm^2 because volume (cm^3) is given per unit width (cm).
The offshore integration limit $x_t = 16\,m$ with average $z_b(x_t) = -0.22\,m$.

computed by subtracting the respective cumulative value of the preceding run from that of the present run.

$$\left.\begin{aligned} \Delta V_e(i) &= V_e(i) - V_e(i-1) \\ \Delta V_d(i) &= V_d(i) - V_d(i-1) \\ \Delta V_c(i) &= V_c(i) - V_c(i-1) \end{aligned}\right\} \quad \text{for} \quad i = 1, 2, \ldots n \tag{3.6}$$

Here, i is an integer counter representing the run number up to the total number of runs, n, in each test (e.g. $n = 18$ for the BD test). For $i = 1$, the incremental volumes in (3.6) equal the volumes measured in the first run since $V_e(0) = V_d(0) = V_c(0) = 0$. In the following, the values given in Tables 3.14 - 3.16 are examined in more detail.

One important point to remember is that the volume of sand contained in the profile between the integration limits x_t and x_e is not conserved. At the landward boundary x_e the sediment transport is only out of the system in the form of overwash which decreases the sand volume contained in the active zone. Hence, it should come as no surprise that for all three tests in this experiment, the volume changes V_c and ΔV_c are almost always positive (net erosion) since large amounts of sand are taken out of the system by means of overwash. The only exception is the first run of test BD where net deposition occurred (Table 3.14). This can be explained by a combination of factors: First, BD1 is part of the initial profile adjustment (Section 3.2.1) where most of the sand that eroded from areas of the dune and berm was simply deposited seaward in the active zone. Only very little sand was removed as overwash in this stage of the test (see Section 3.3). Second, BD1 was the first test of the experiment which means that the initial profile which was constructed arbitrarily adjusted to the imposed wave and water level conditions, even offshore of the integration limit x_t, leading to a net influx of sediment through the offshore boundary.

In order to understand the listed values of cumulative deposition volume, V_d, and incremental deposition volume during each individual run, ΔV_d, one has to remember that V_d simply represents the amount of sand deposited between x_t and x_e as given by (3.4) referenced to the initial profile. Positive values for ΔV_d signify that the deposited area is reduced during the present run. Negative values of ΔV_d, on the other hand, show that the deposited area increased during the present run.

This way of representing profile volume changes becomes clearer when comparing the actual incremental volume changes, ΔV_c, with the incremental erosion volumes, ΔV_e. If they are both positive and similar in value, most of the volume changes are due to erosion in the active zone; if ΔV_c is much smaller than ΔV_e, a considerable amount of deposition occurred for a part of the profile during the respective run.

The initial profiles for the BD, WD, and SD tests were constructed using identical amounts of sand between the cross-shore limits x_t and x_e. At the end of each test the total reduction in sand volume per unit width within these limits was approximately the same: After run BD18, WD12, and SD15, the cumulative volume changes V_c were 2760, 2727, and 2533 cm^2, respectively. In the next sections, the analysis of the collected sediment volumes of overwash is presented including comparisons with the measured volumetric profile changes discussed above.

3.3 Overwash

Water and sediment were transported over the crest of the impermeable vertical wall behind the dune by wave overtopping during each test run. This overwash was then forced through a horizontal streamer trap retaining the sand particles by means of a fine polyester fabric mesh (Section 2.4). The overtopped water was collected, measured and, if necessary, pumped back into the main tank to keep the SWL constant during a run. The analysis of each collected sand sample included its wet weight immediately after the collection and its dry weight after 12 hours of oven drying. In addition, a sieve analysis was performed for each sample to obtain sediment grain size distributions and characteristic sediment parameters for every run. Overwash sediment volume per unit width, V_{bs}, was estimated using the entire dry weight of a sample and dividing it by the density of quartz sand $\rho_s = 2.6\, g/cm^3$ and the width of the flume ($115\, cm$) where V_{bs} is the volume per unit width of the overwash sand without voids (bedload + suspended load). Water volume is comprised of two parts including the amount overtopped and measured during a run and the amount stored in the wet overwash sand. The water volume per unit width, V_{wo}, was obtained by dividing the measured volume (cm^3) by the flume width of $115\, cm$.

3.3.1 Transport Rates

In Figure 3.8 the overwash results from tests BD, WD, and SD are compared using the time series of the sediment (bedload + suspended load) transport rate q_{bs}, the water transport (wave overtopping) rate q_o and their ratio q_{bs}/q_o. These rates (cm^2/s) represent averages over the respective run lasting $400\, s$ and each data point

is plotted at the middle of the respective 400-s run interval with

$$\begin{aligned} q_{bs} &= \frac{V_{bs}}{400\ s} \\ q_o &= \frac{V_{wo}}{400\ s} \end{aligned} \tag{3.7}$$

where V_{bs} and V_{wo} are the corresponding volumes per unit width. Kobayashi et al. (1996) suggested the ratio q_{bs}/q_o to be approximately 4% on the basis of their smaller-scale experiments using sand with $d_{50} = 0.38\,mm$ in comparison to the present sand with $d_{50} = 0.18\,mm$.

The evolution of the measured transport rates over the crest of the vertical wall shows how wave overtopping and onshore sediment transport change as the dune erodes. In general, the overall shapes of the evolution curves plotted in Figure 3.8 are fairly similar for the BD, WD, and SD tests but the curves are shifted in time due to the respective initial dune geometry for each test. Besides the apparent time shift, the main difference between the three tests is the overwash rate during the first run where q_{bs} and q_o are much larger for WD than for BD and SD due to the relatively large water depth at the toe of the wide dune for WD as discussed in Section 3.2.1. After this initial spike the rates are reduced to similar levels in all three tests. After the initial profile adjustment due to offshore sand movement the wave overtopping rate and the overwash rate were reduced in run WD2 because of the decrease of the seaward slope of the dune.

In order to simplify the analysis of the results shown in Figures 3.5, 3.6, 3.7, and 3.8 we separate the observed dune profile and overwash evolution process into three phases:

Phase 1: Sediment eroded from the dune through scarping and slumping processes was predominantly transported in the offshore direction. The offshore sand

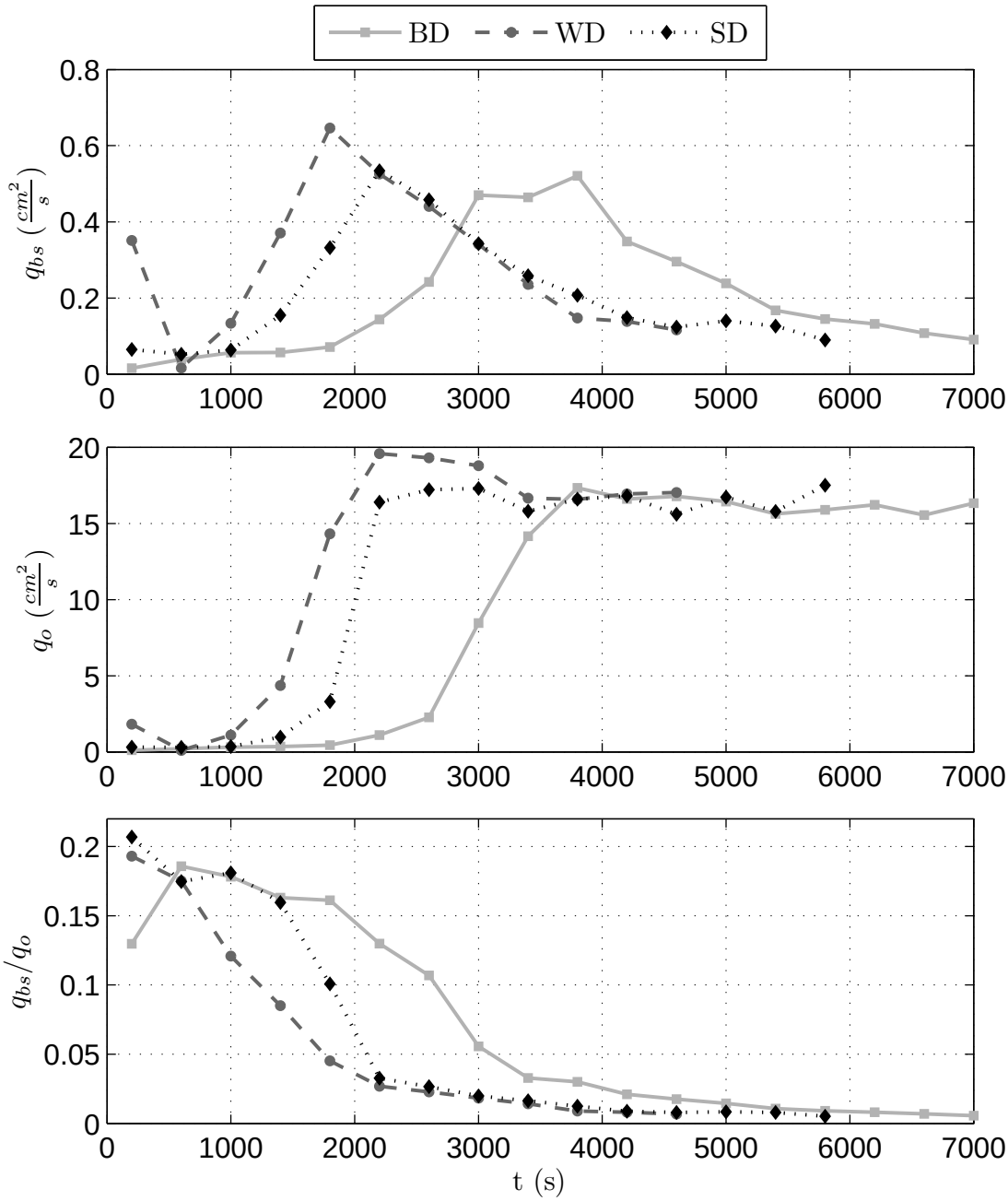

Figure 3.8: *Overwash transport rate parameters as a function of time t for BD, WD, and SD tests. The top two panels show the sand transport rate q_{bs} (bedload + suspended load) and water transport rate q_o, respectively. Their ratio is depicted in the bottom panel. Data points are averages over the respective 400-s run.*

transport smoothed out the dune and beach profile and caused onshore migration and moderate lowering of the dune crest of less than 5 cm. Apart from the initial WD run, profile volume changes ΔV_c stayed below $150\,cm^2$. Only limited wave overtopping and sediment overwash occurred ($q_o < 2\,\frac{cm^2}{s}$, $q_{bs} < 0.2\,\frac{cm^2}{s}$) but the sediment concentration based on the ratio q_{bs}/q_o was above 10%.

Phase 2: Wave overtopping and sediment overwash increased rapidly as a result of the rapid dune crest lowering. The value of ΔV_c reached peak values of 378, 439, and $407\,cm^2$ for the BD, WD, and SD tests, respectively. Sediment overwash q_{bs} also increased to maximum values in excess of $0.5\,cm^2/s$ in each test and the wave overtopping rate q_o reached its highest level at the end of this phase with maxima between 17 and $20\,cm^2/s$. This caused complete destruction of the dune during which its crest was lowered to the level of the vertical wall crest while migrating seaward. A horizontal beach platform in front of the vertical wall was all that remained from the dune.

Phase 3: The beach in front of the vertical wall continued to erode until the SWL reached the vertical wall. First, the horizontal beach was continuously narrowed, followed by the overall lowering of the entire nearshore profile. Wave overtopping stayed at a high, fairly constant level ($q_o > 15\,cm^2/s$) but sediment overwash decreased to values around $0.1\,cm^2/s$ at the end of each test due to the influence of the wall obstacle. The sediment concentration of the collected overwash was reduced to approximately 0.5%.

Table 3.17 breaks down the BD, WD, and SD tests according to the three evolution phases where run numbers and durations are given for each test and each phase. The effects of the impermeable vertical wall at the landward end of the beach profile are discussed for each phase. During phase 1 the wall effects were probably

negligible since the dune was still intact with the crest level well above the crest of the vertical wall. The flow of water and the sediment transport on the landward slope of the dune were not hindered by the presence of the wall. In phase 2 the wall started to play a role in the formation of the previously described horizontal beach by keeping profile elevations constant at the wall's crest level right in front of the wall. Both hydrodynamics and overwash were affected strongly by the presence of the vertical wall in phase 3.

Table 3.17: *Phases of profile and overwash evolution for BD, WD, and SD tests.*

Phase	**Description**	**BD**	**WD**	**SD**
1	Dune erosion and crest lowering by predominantly seaward sediment transport and limited overwash	BD1−BD6 ($0 - 2400\ s$)	WD1−WD3 ($0 - 1200\ s$)	SD1−SD4 ($0 - 1600\ s$)
2	Dune destruction by rapidly increasing wave overtopping and sediment overwash over vertical wall	BD7−BD9 ($2400 - 3600\ s$)	WD4−WD5 ($1200 - 2000\ s$)	SD5−SD6 ($1600 - 2400\ s$)
3	Beach erosion in front of vertical wall with constant wave overtopping and decreasing sediment overwash	BD10−BD18 ($3600 - 7200\ s$)	WD6−WD12 ($2000 - 4800\ s$)	SD7−SD15 ($2400 - 6000\ s$)

The present experiment may correspond to a dune in front of a seawall or a dune with a relatively steep landward slope located on a low backshore. For these cases, sediment transported landward is lost from the dune profile. In accordance with listed run numbers in Table 3.17 for each test the measured profiles separating the three evolution phases are plotted in Figures 3.9 to 3.11 for the visual inspection of the three phases.

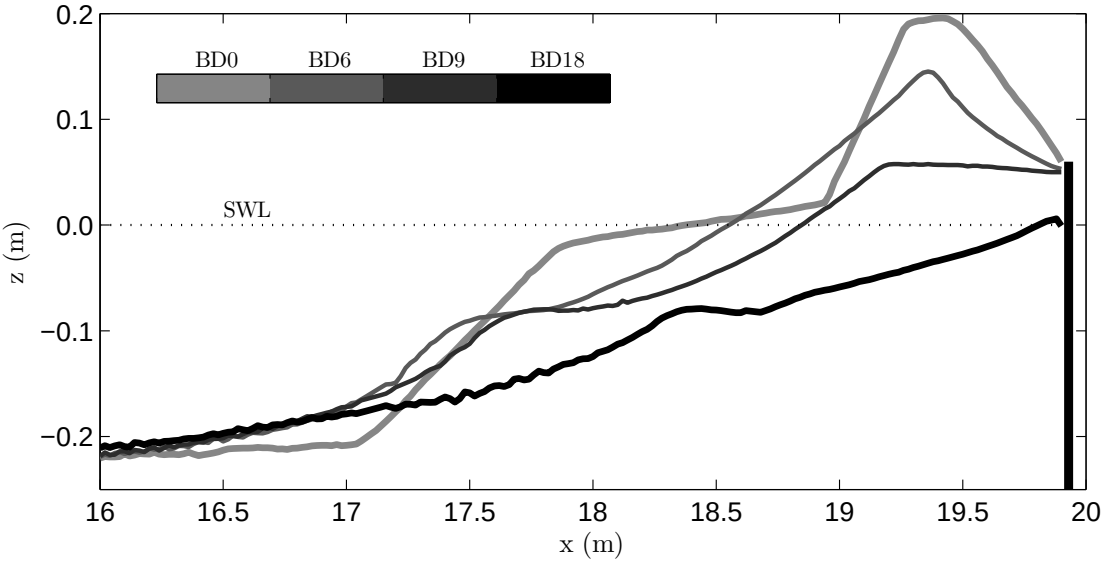

Figure 3.9: *Four measured profiles of BD test separating three evolution phases.*

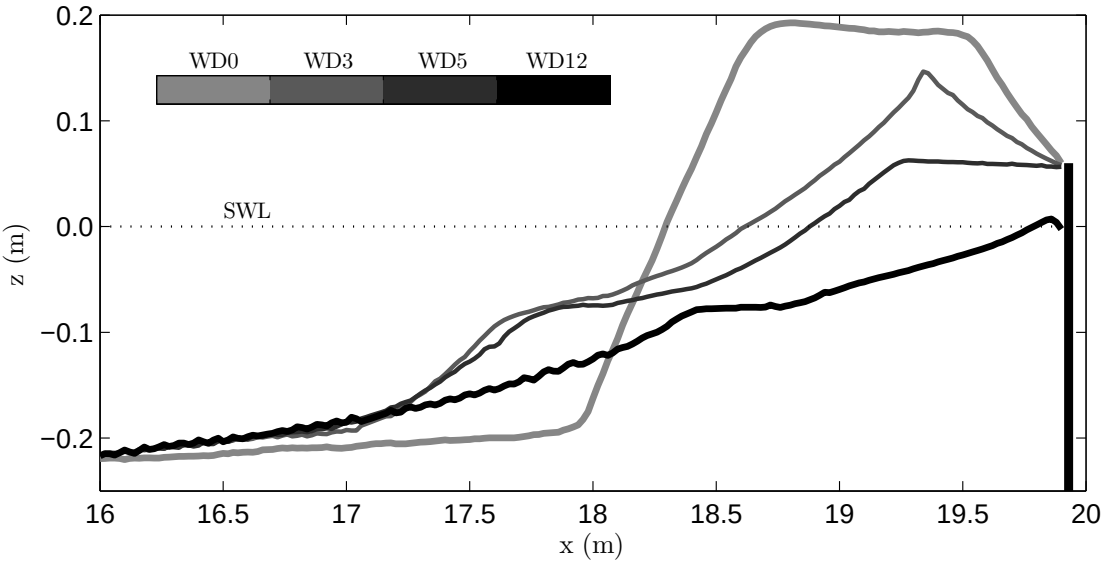

Figure 3.10: *Four measured profiles of WD test separating three evolution phases.*

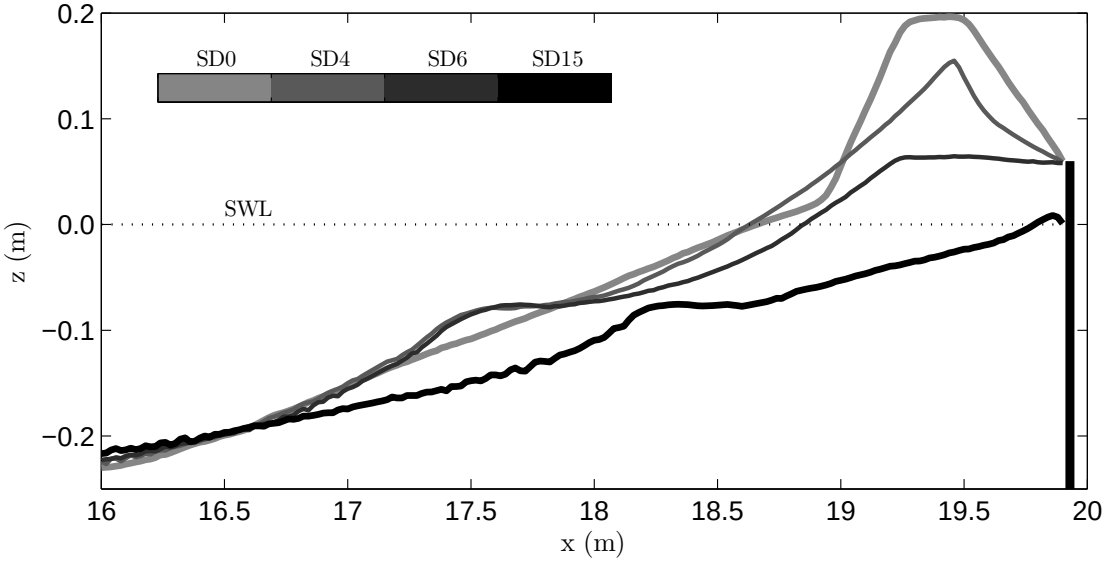

Figure 3.11: *Four measured profiles of SD test separating three evolution phases.*

3.3.2 Overwash Volume and Profile Change Relationship

Sand distributed over a beach profile occupies a certain volume depending on the voids surrounding individual grains. The actual porosity (n_p) depends on grain sizes, grain shapes and degree of compaction. For our analysis the porosity is assumed to be $n_p = 0.4$ based on previous tests (Section 2.1.1). Since sediment overwash is measured by dry weight in our experiment, we must differentiate between overwash volume excluding voids, V_{bs} (bedload and suspended load), and sand overwash volume including voids, $V_{so} = V_{bs}/(1 - n_p)$. When comparing measured profile changes to collected sand overwash volume it is necessary to include the characteristic void portion included in the profile volume change per unit width tabulated in Tables 3.14, 3.15, and 3.16. Figure 3.12 shows this comparison for cumulative volume measurements where V_e and V_c are the measured cumulative profile erosion and the volume change per unit width, respectively. V_{cso} is the measured cumulative sediment overwash volume per unit width starting from the first run.

The plotted curves all have a characteristic S-shape since the gradients of the

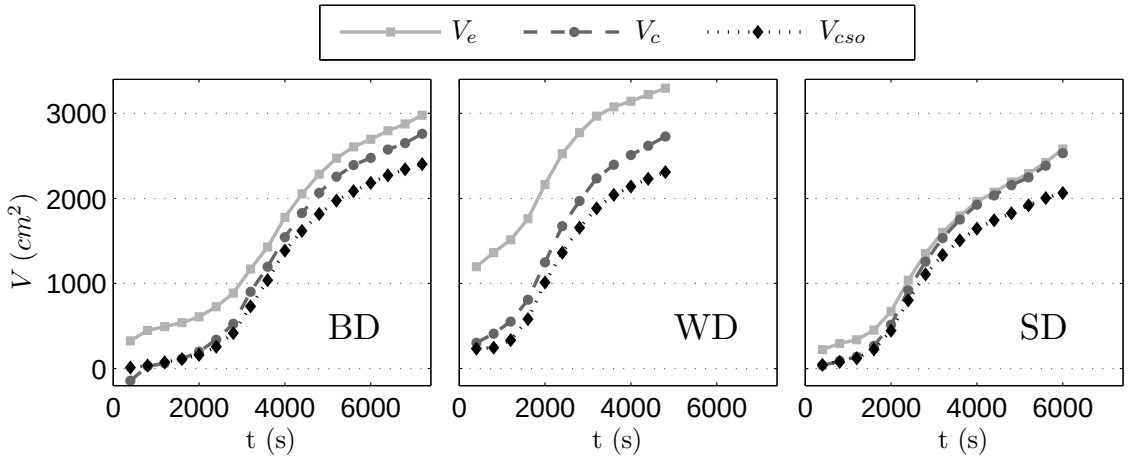

Figure 3.12: *Cumulative erosion and overwash parameters.*

cumulative values increased significantly during phase 2 of the profile and overwash evolution before decreasing again toward the end of the tests after the dune was destroyed. The sediment overwash volume V_{cso} correlates well with the positive (erosion) profile change volume V_c but their difference increases toward the end of the respective tests. In each test, the final V_c value is larger than the final V_{cso} value by 357, 419, and 470 cm^2 for the BD, WD, and SD tests, respectively, which corresponds to 13%, 15%, and 18% of the respective final V_c value. This difference represents the sediment volume transported offshore past the integration limit $x_t = 16\,m$ during each test. Integrating the profile changes in the offshore region ($x = 0$ to $16\,m$) supports this conclusion since V_c in that region has values of -273, -380, and $-633\,cm^2$ for the BD, WD, and SD tests, respectively. These negative values indicate minor offshore deposition. The remaining net balances between the volume changes in the active zone and the offshore region are 84, 39, and $-163\,cm^2$ for the BD, WD, and SD tests, respectively. This corresponds to a change in bottom elevation of less than $1\,mm$ over the entire profile which is well within the given accuracy limit of the profile measurements (Section 2.3).

The difference between cumulative erosion volume V_e and volume change

V_c in the active zone is the deposited volume (V_d in Tables 3.14, 3.15, and 3.16). This difference decreases toward the end of each run but its absolute value varies greatly depending on the initial test geometry. Test WD, for example, shows a large difference between V_e and V_c since most of the material that eroded from the dune during the initial profile adjustment is deposited inside the active zone right in front of the dune. Test SD, on the other hand, shows practically no deposition at the end of the test compared to the initial profile since the gradual slope in front of the dune already resembles the deposition pattern observed in the two other tests fairly closely.

The ratio of V_{cso} and V_e indicates the overwash contribution to the eroded sand volume and is displayed in Figure 3.13. This information is useful in determining the evolution of the predominant transport direction. Initial offshore transport and redistribution of sediment in the zone of $x = 16.0 - 19.9\,m$ is followed by increased overwash contribution due to the increased wave overtopping. Towards the end of each test the ratio levels out between 0.6 and 0.8 which means that up to 80% of the volume eroded from the initial profile eventually moved onshore to be collected as overwash.

In the following, the comparison between profile change and sediment overwash volume is compared using their incremental values. The sand overwash volume V_{so} was measured for each run and is compared to the incremental profile erosion volume ΔV_e and profile volume change ΔV_c in Figure 3.14. The two latter values represent changes that occurred in each 400-s run.

Figure 3.14 reveals that major differences between the three volume measures are only apparent during the first two runs of each test where ΔV_e and ΔV_c deviated significantly due to large deposition values (Tables 3.14 to 3.16) and V_{so} was adjusting to the new profile geometries. The collected overwash volume V_{so} is related to

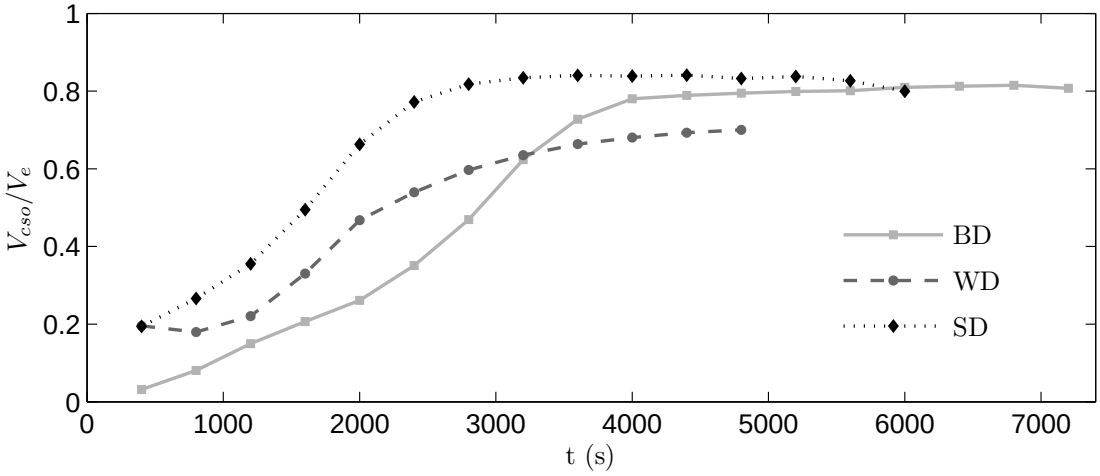

Figure 3.13: *Ratio of cumulative sand overwash volume V_{cso} and profile erosion volume V_e.*

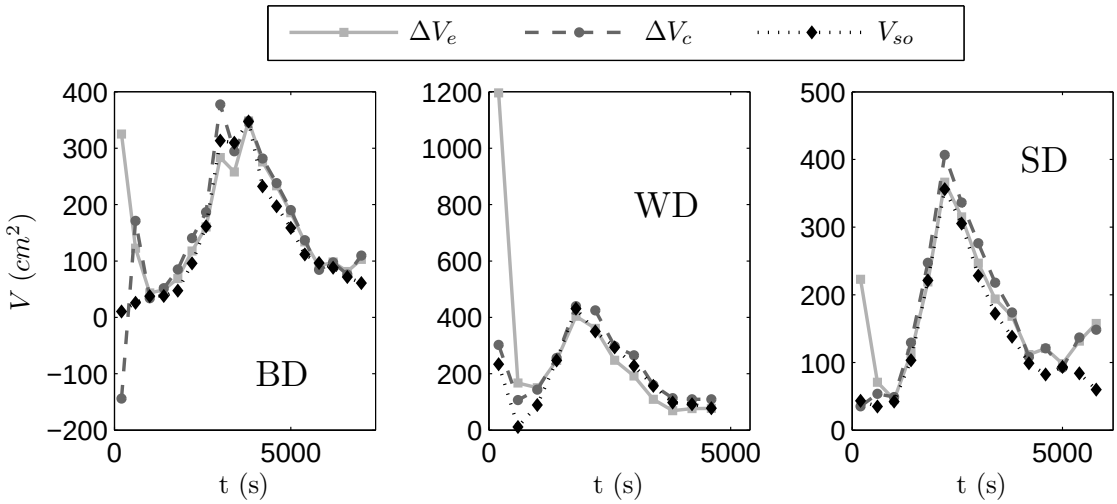

Figure 3.14: *Sand overwash volume V_{so} for each run compared to incremental profile erosion (ΔV_e) and volume change (ΔV_c) for each run.*

the overwash sediment transport rate q_{bs} by (3.7) and thus follows the same evolution pattern with increasing values until the dune is destroyed completely, followed by decreasing values up to the end of each test. ΔV_e and ΔV_c follow this trend closely which shows that the measured profile evolution is predominantly caused by wave-induced overwash.

The ratios of the incremental overwash volume to the respective profile change parameters are compared for all three tests in the two panels of Figure 3.15 with $V_{so}/\Delta V_e$ in the top panel and $V_{so}/\Delta V_c$ in the bottom panel. For most runs the ratio $V_{so}/\Delta V_c$ (bottom panel) stays fairly close to, but slightly below, unity which implies that sand removed from the active profile zone is mostly collected as overwash during each run. Again, the exception is the initial period of profile adjustment where eroded material is deposited within the active zone rather than transported over the vertical wall into the sediment trap. The pattern for the ratio $V_{so}/\Delta V_e$ (top panel) is similar, however, the values deviate more from unity since deposition volumes within the active zone are not considered. Values well below unity during the first few runs of each test are artifacts of the initial profile adjustment and values above unity further into the tests show that some of the eroded volume is not collected as overwash but rather deposited within the profile integration limits or transported offshore outside the active zone (only if $V_{so}/\Delta V_c$ is also above unity for the same run).

In addition to the graphical display of the measured parameters, the most important overwash values are listed in Tables 3.18, 3.19, and 3.20 for the BD, WD, and SD test series, respectively. In summary, the dune erosion and its crest lowering in this experiment was caused by the onshore sediment transport over the dune crest after the initial profile adjustment.

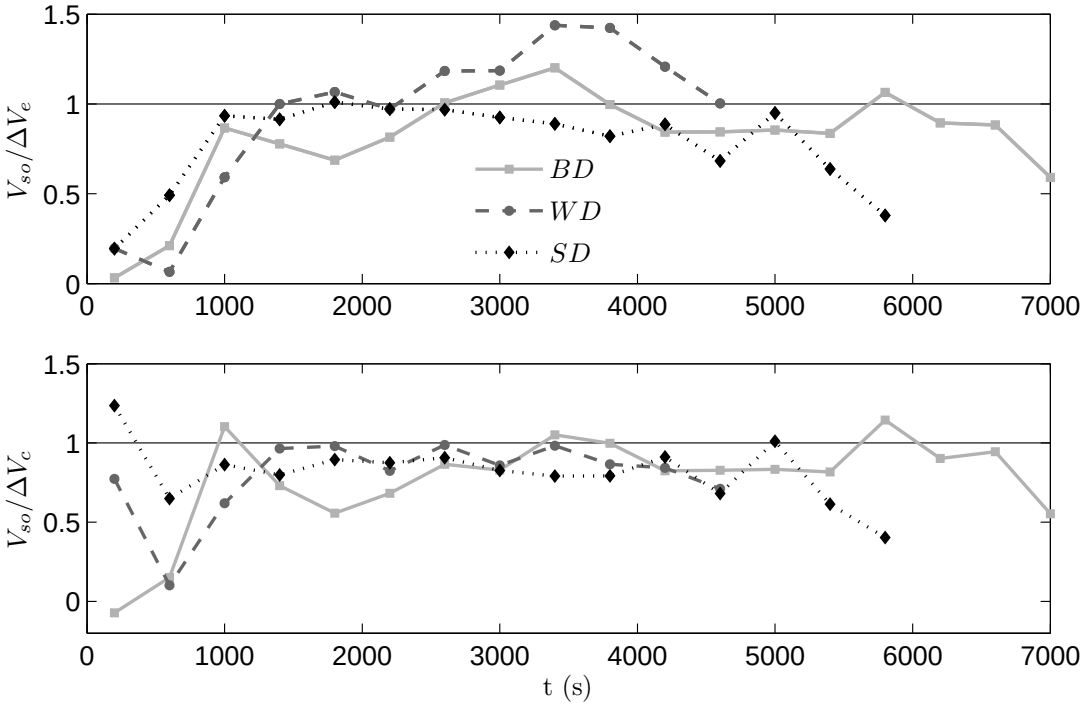

Figure 3.15: *Ratio of overwash sediment volume V_{so} and incremental profile erosion volume ΔV_e (top panel) and ratio of V_{so} and incremental volume change ΔV_c (bottom panel).*

Table 3.18: *Sand and water overwash data for 18 runs of test BD.*

Test	q_{bs} $\left(\frac{cm^2}{s}\right)$	q_{wo} $\left(\frac{cm^2}{s}\right)$	V_{cso} (cm^2)	V_{cso}/V_e $(-)$	V_{so} (cm^2)	$V_{so}/\Delta V_e$ $(-)$	$V_{so}/\Delta V_c$ $(-)$
BD1	0.02	0.12	10	0.03	10.2	0.03	-0.07
BD2	0.04	0.21	36	0.08	25.9	0.21	0.15
BD3	0.06	0.32	74	0.15	37.5	0.87	1.10
BD4	0.06	0.35	112	0.21	37.9	0.78	0.73
BD5	0.07	0.44	159	0.26	47.4	0.69	0.56
BD6	0.14	1.11	255	0.35	95.9	0.82	0.68
BD7	0.24	2.27	416	0.47	161.4	1.01	0.87
BD8	0.47	8.46	730	0.62	313.3	1.11	0.83
BD9	0.46	14.17	1039	0.73	309.6	1.20	1.05
BD10	0.52	17.33	1386	0.78	347.2	1.00	1.00
BD11	0.35	16.61	1619	0.79	232.4	0.84	0.82
BD12	0.30	16.78	1816	0.79	197.0	0.84	0.83
BD13	0.24	16.44	1975	0.80	158.8	0.85	0.83
BD14	0.17	15.63	2086	0.80	111.7	0.84	0.82
BD15	0.14	15.90	2183	0.81	96.6	1.06	1.14
BD16	0.13	16.22	2271	0.81	88.0	0.89	0.90
BD17	0.11	15.55	2343	0.81	71.7	0.88	0.95
BD18	0.09	16.33	2403	0.81	60.7	0.59	0.55

3.3.3 Sediment Analysis

Grain size analyses have been carried out on the overwash sand in each run to investigate changes in the size distribution evolution that can be correlated with the measured overwash sediment transport rate q_{bs}. The evolution of characteristic grain size diameters d_{16} (16% finer by weight), d_{50} (median diameter), and d_{84} (84% finer by weight) obtained from the respective size distributions are shown in Figure 3.16 normalized by the reference diameter $d_r = 0.18\ mm$ which is the median diameter of the sand in the flume as listed in Table 2.1. Many different factors influence the size distribution of the overwash sediment. Amongst the most important ones are

Table 3.19: *Sand and water overwash data for 12 runs of test WD.*

Test	q_{bs} $\left(\frac{cm^2}{s}\right)$	q_{wo} $\left(\frac{cm^2}{s}\right)$	V_{cso} (cm^2)	V_{cso}/V_e $(-)$	V_{so} (cm^2)	$V_{so}/\Delta V_e$ $(-)$	$V_{so}/\Delta V_c$ $(-)$
WD1	0.35	1.82	234	0.20	234.0	0.20	0.77
WD2	0.02	0.09	245	0.18	10.9	0.07	0.10
WD3	0.13	1.10	334	0.22	89.0	0.59	0.62
WD4	0.37	4.36	581	0.33	247.1	1.00	0.97
WD5	0.65	14.32	1012	0.47	430.9	1.07	0.98
WD6	0.53	19.58	1362	0.54	350.4	0.97	0.82
WD7	0.44	19.31	1656	0.60	293.8	1.18	0.99
WD8	0.34	18.78	1884	0.64	227.5	1.19	0.86
WD9	0.24	16.66	2041	0.66	157.2	1.44	0.98
WD10	0.15	16.58	2139	0.68	98.1	1.42	0.87
WD11	0.14	16.94	2231	0.69	92.1	1.21	0.84
WD12	0.12	17.03	2308	0.70	77.6	1.00	0.71

the sediment overwash rate, the respective contribution of bedload and suspended load, and the state of the erosion progress.

Larger grains represented by d_{84}/d_r varied most with time. The evolution of d_{84}/d_r is most closely correlated with the sediment transport rate q_{bs}. As the rate increases so does the mobilization of larger grains. During minor overwash events in the early stage of each test, the flow of overtopping water may not be strong enough to carry the larger grains located on the dune surface into the sand trap. The ratio d_{50}/d_r stays fairly constant but slightly above unity since silt particles are not included in the grain size distribution of the collected overwash samples. The evolution of the grain size distribution may be related to the mobility and availability of different grain sizes but the detailed sediment dynamics are uncertain.

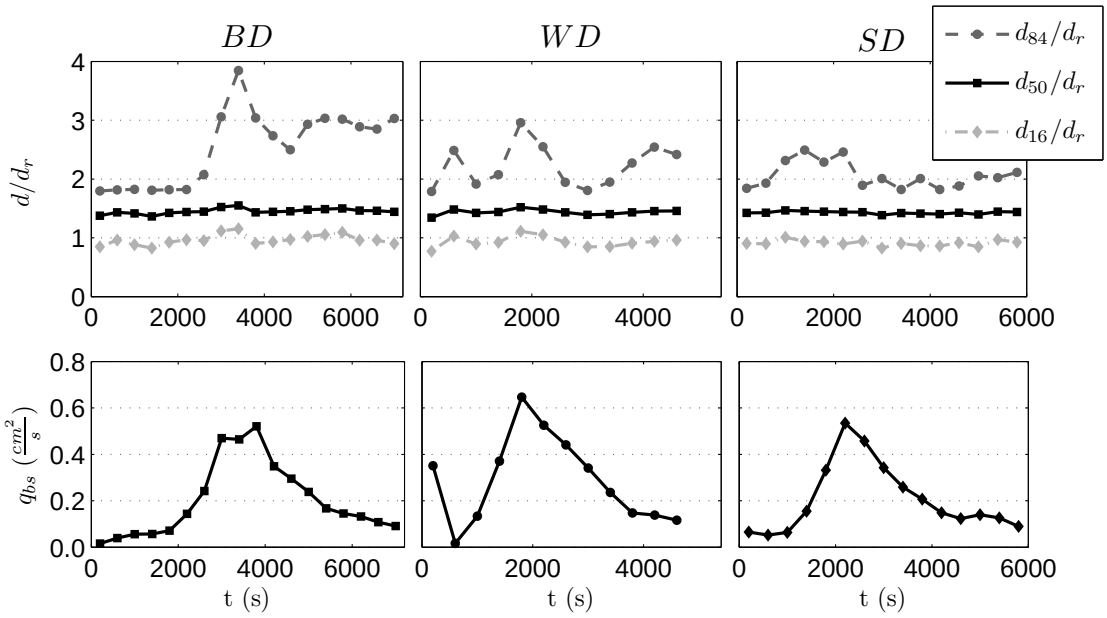

Figure 3.16: *Evolution of characteristic grain diameters of overwash sediment normalized by reference diameter $d_r = 0.18$ mm (top panels). Indices indicate the percentage of sand finer by weight (e.g. d_{50} = median diameter). The measured sediment transport rate q_{bs} (bottom panels) correlates best with d_{84}/d_r.*

Table 3.20: *Sand and water overwash data for 15 runs of test SD.*

Test	q_{bs} $\left(\frac{cm^2}{s}\right)$	q_{wo} $\left(\frac{cm^2}{s}\right)$	V_{cso} (cm^2)	V_{cso}/V_e $(-)$	V_{so} (cm^2)	$V_{so}/\Delta V_e$ $(-)$	$V_{so}/\Delta V_c$ $(-)$
SD1	0.07	0.31	43	0.19	43.3	0.19	1.24
SD2	0.05	0.30	78	0.27	34.8	0.49	0.65
SD3	0.06	0.35	120	0.36	42.3	0.93	0.86
SD4	0.15	0.97	224	0.49	103.2	0.91	0.80
SD5	0.33	3.29	445	0.66	221.4	1.01	0.89
SD6	0.53	16.40	801	0.77	356.1	0.97	0.88
SD7	0.46	17.22	1106	0.82	305.3	0.97	0.91
SD8	0.34	17.29	1335	0.83	228.2	0.92	0.83
SD9	0.26	15.80	1507	0.84	172.3	0.89	0.79
SD10	0.21	16.59	1645	0.84	137.9	0.82	0.79
SD11	0.15	16.81	1744	0.84	98.8	0.89	0.91
SD12	0.12	15.60	1826	0.83	82.3	0.68	0.68
SD13	0.14	16.72	1919	0.84	93.3	0.95	1.01
SD14	0.13	15.79	2003	0.83	84.0	0.64	0.61
SD15	0.09	17.50	2063	0.80	59.8	0.38	0.40

Chapter 4

NUMERICAL MODEL CSHORE

This chapter describes the main components of the depth-averaged cross-shore model CSHORE (Kobayashi et al., 2010). The following sections explain the mathematical formulation of the combined wave and current model in CSHORE and the extension of the computation domain to the wet and dry zone of the bottom profile using a probabilistic approach. Finally, a modified sediment transport model is presented for the improved prediction of the major overwash events in the present experiment.

4.1 Combined Wave and Current Model

The time-averaged cross-shore numerical model developed by Kobayashi et al. (2009) is extended here to include wave and current interactions in order to account for the onshore water flux due to wave overtopping. In the following, use is made of linear wave and current theory (e.g., Mei, 1989). The impermeable bottom elevation $z_b(x)$, the still water level S above $z = 0$, and the measured values of T_p, $\overline{\eta}$, and σ_η at $x = 0$ for each test are specified as input. The still water level was constant and $S = 0$ in the present experiment. The computation marches landward to predict the cross-shore variations of $\overline{\eta}$ and σ_η and the wave overtopping rate q_o at the landward end of the crest as shown in Figure 4.1.

The time-averaged continuity equation for the impermeable bottom requires that the time averaged volume flux is constant and equal to q_o. The current velocity felt by waves is given by $q_o/\overline{h}$ where $\overline{h}$ = mean water depth given by $\overline{h} = (S + \overline{\eta} - z_b)$

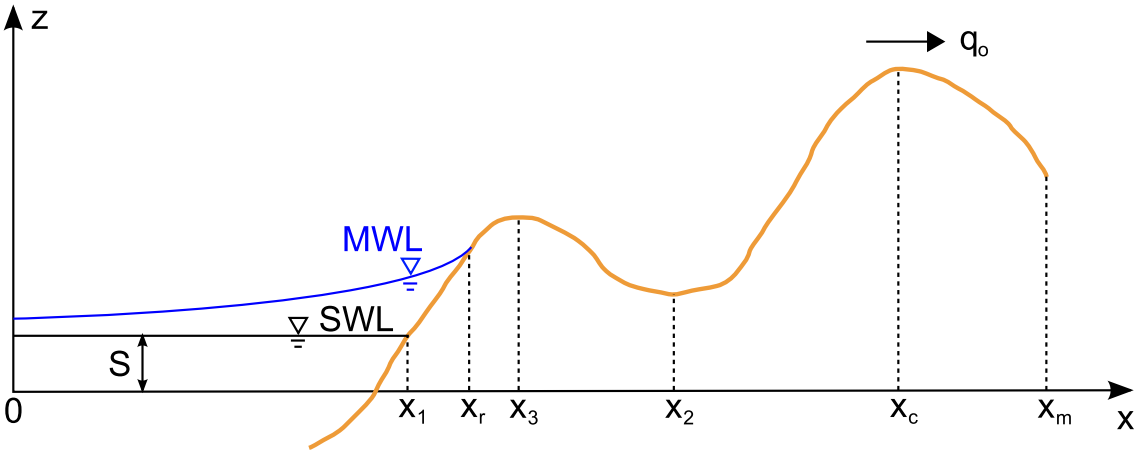

Figure 4.1: *Transition from wet model ($x < x_r$) to wet and dry model ($x > x_1$) for dune overwash prediction.*

where the overbar denotes time averaging. The representative wave period for irregular waves is assumed to be the spectral peak period T_p. The dispersion relation for linear waves in the presence of the current $q_o/\overline{h}$ is expressed as

$$\omega = kg\ tanh\left(k\overline{h}\right) \quad ; \quad \omega + k\, q_o\, /\, \overline{h} = \omega_p \tag{4.1}$$

where ω = intrinsic angular frequency; k = wave number; g = gravitational acceleration; and ω_p = absolute angular frequency given by $\omega_p = 2\pi/T_p$. The wave period T for waves moving with the current $q_o/\overline{h}$ is given by $T = 2\pi/\omega$. Equation (4.1) can be solved iteratively to obtain k and ω for known ω_p, $\overline{h}$, and q_o. The phase velocity C and the group velocity C_g are given by

$$C = \omega/k \ ; \quad C_g = \frac{C}{2}\left[1 + \frac{2k\overline{h}}{sinh\left(2k\overline{h}\right)}\right] \tag{4.2}$$

The effect of the current in Equation (4.1) becomes important in very shallow water where the current $q_o/\overline{h}$ may become as large as the phase velocity.

The cross-shore fluid velocity is represented by the depth-averaged velocity U

whose probability distribution is assumed to be Gaussian. The mean and standard deviation of U are denoted by $\overline{U}$ and σ_U. Linear progressive wave theory in finite depth is used to obtain

$$\sigma_U = C\,\frac{\sigma_\eta}{\overline{h}} \quad ; \qquad \frac{g\,\sigma_\eta^2}{C} + \overline{h}\,\overline{U} = q_o \tag{4.3}$$

where $g\,\sigma_\eta^2/C$ is the onshore volume flux induced by waves. The relations in Equation (4.3) are used to obtain σ_U and $\overline{U}$ for known C, $\overline{h}$, σ_η, and q_o. The time-averaged return flow velocity $\overline{U}$ is negative (offshore) and the wave overtopping rate q_o (onshore) reduces the return flow velocity.

The time-averaged momentum equation is written as

$$\frac{d}{dx}\left(S_{xx} + \frac{\rho\,q_o^2}{\overline{h}}\right) + \rho\,g\,\overline{h}\,\frac{d\overline{\eta}}{dx} + \tau_b = 0 \tag{4.4}$$

with

$$S_{xx} = \rho\,g\,\sigma_\eta^2\left(2\frac{C_g}{C} - \frac{1}{2}\right) \quad ; \qquad \tau_b = \frac{1}{2}\,\rho\,f_b\,\sigma_U^2\,G_2 \tag{4.5}$$

where S_{xx} = cross-shore radiation stress; ρ = fluid density; τ_b = time-averaged bottom shear stress; f_b = bottom friction factor which is allowed to vary spatially; and G_2 = analytical function of $\overline{U}/\sigma_U$ given by Kobayashi et al. (2007). The computed results are not sensitive for f_b of the order of 0.01 and use is made of $f_b = 0.015$ as in Kobayashi et al. (2009). The mean water level $\overline{\eta}$ is induced by the radiation stress S_{xx} and the volume flux q_o. If $S_{xx} = 0$ and $b = 0$, Equation (4.4) yields $\left[\overline{U^2}/\,(2g) + \overline{\eta}\right]$ = constant where $q_o = \overline{h}\,\overline{U}$ in the absence of waves. These simple equations are normally used to analyze steady flow over a weir (e.g., Henderson, 1966). The mean water level $\overline{\eta}$ decreases landward with the landward increase of $\overline{U}$ in the absence of waves. Equation (4.4) mainly determines the cross-shore variation of $\overline{\eta}$.

In order to predict the cross-shore variation of σ_η, in the presence of the

volume flux q_o, the wave action equation is expressed as

$$\frac{d}{dx}\left(\frac{F_x}{\omega}\right) = -\frac{D_B + D_f}{\omega} \tag{4.6}$$

with

$$F_x = \rho\, g\, \sigma_\eta^2 \left(C_g + \frac{q_o}{\overline{h}}\right) \quad ; \quad D_B = \frac{\rho\, g\, a_B\, Q\, H_B^2}{4\, T} \quad ; \quad D_f = \frac{1}{2}\, \rho\, f_b\, \sigma_U^3\, G_3 \tag{4.7}$$

where F_x = cross-shore wave energy flux including the effect of q_o; D_B, and D_f = energy dissipation rate per unit horizontal area due to wave breaking, and bottom friction, respectively; a_B = empirical parameter introduced by Kobayashi et al. (2007) to account for the effect of the bottom slope on D_B; Q = fraction of breaking waves given by Battjes and Stive (1985); H_B = breaker height for the estimation of D_B; and G_3 = analytical function of $\overline{U}/\sigma_U$ given by Kobayashi et al. (2007). The current effect on wave breaking is simply accounted for in Equation (4.7) using the wave period T obtained from Equation (4.1). Likewise, the equations for a_B and H_B given by Kobayashi et al. (2007) are modified to use the wave number k obtained from Equation (4.1).

The landward marching computation using Equations (4.1) - (4.7) is continued as long as the computed $\overline{h}$ and σ_η are positive but terminated at the landward end of the crest located at $x = x_c$. This end location of the computation is denoted as x_r. For the emerged crest shown in Figure 4.1, this location is on the seaward slope where $\overline{h}$ is less than $1\,cm$. Equations (4.1) - (4.7) based on linear Gaussian wave theory are not valid in the zone which is not always wet. A probabilistic model is developed for this intermittently wet and dry zone.

4.2 Probabilistic Model for Wet and Dry Zone

The time-averaged cross-shore continuity and momentum equations derived from the nonlinear shallow-water wave equations are expressed as (Kobayashi et al., 1989)

$$\overline{hU} = q_o \tag{4.8}$$

$$\frac{d}{dx}\left(\overline{hU^2} + \frac{g}{2}\overline{h^2}\right) = -gS_b\overline{h} - \frac{1}{2}f_b\overline{|U|U} \quad ; \qquad S_b = \frac{dz_b}{dx} \tag{4.9}$$

where h and U = instantaneous water depth and cross-shore velocity, respectively; and S_b = bottom slope. The instantaneous water depth h at given x is described probabilistically rather than in the time domain. Kobayashi et al. (1998) analyzed the probability distributions of the free surface elevations measured in the shoaling, surf and swash zones. The measured probability distributions were shown to be in agreement with the exponential gamma distribution which reduces to the Gaussian distribution offshore and the exponential distribution in the lower swash zone. The assumption for the Gaussian distribution has simplified the model based on Equations (4.1) - (4.7) in the wet zone significantly.

The assumption of the exponential distribution is made here to simplify the model in the wet and dry zone. The probability density function $f(h)$ is expressed as

$$f(h) = \frac{P_w^2}{\overline{h}}\, exp\left(-P_w\,\frac{h}{\overline{h}}\right) \qquad \text{for} \quad h > 0 \tag{4.10}$$

with

$$P_w = \int_0^\infty f(h)\,dh \quad ; \qquad \overline{h} = \int_0^\infty h\,f(h)\,dh \tag{4.11}$$

where P_w = wet probability for the water depth $h > 0$; and $\overline{h}$ = mean water depth for the wet duration. The dry probability of $h = 0$ is equal to $(1 - P_w)$. The mean water depth for the entire duration is equal to $P_w\overline{h}$. The overbar in Equations (4.8) and (4.9) indicates averaging for the wet duration only. The free surface elevation $(\eta - \overline{\eta})$ above MWL is equal to $(h - \overline{h})$. The standard deviations of η and h are the

same and given by

$$\frac{\sigma_\eta}{\overline{h}} = \left(\frac{2}{P_w} - 2 + P_w\right)^{0.5} \tag{4.12}$$

which yields $\sigma_\eta = \overline{h}$ for $P_w = 1$. This equality was supported by the depth measurements in the lower swash zone by Kobayashi et al. (1998) who assumed $P_w = 1$ in Equation (4.10).

The cross-shore velocity U may be related to the depth h in the wet and dry zone and expressed as

$$U = \alpha\sqrt{gh} + U_s \tag{4.13}$$

where α = positive constant; and U_s = steady velocity which is allowed to vary with x. The steady velocity U_s is included to account for offshore return flow on the seaward slope and the downward velocity increase on the landward slope. Holland et al. (1991) measured the bore speed and flow depth on a barrier island using video techniques and obtained $\alpha \simeq 2$ where the celerity and fluid velocity of the bore are assumed to be approximately the same. Tega and Kobayashi (1996) computed wave overtopping of dunes using the nonlinear shallow-water wave equations and showed $\alpha \simeq 2$ for the computed U and h. As a result, use may be made of $\alpha = 2$ as a first approximation. Using Equations (4.10) and (4.13), the mean $\overline{U}$ and standard deviation σ_U of the cross-shore velocity U can be expressed as

$$\overline{U} = \frac{\sqrt{\pi}}{2}\,\alpha\left(P_w\, g\,\overline{h}\right)^{0.5} + P_w U_s \tag{4.14}$$

$$\sigma_U^2 = \alpha^2 g\,\overline{h} - 2\left(\overline{U} - U_s\right)\left(\overline{U} - P_w U_s\right) + P_w\left(\overline{U} - U_s\right)^2 \tag{4.15}$$

Equation (4.13) is substituted into Equations (4.8) and (4.9) which are averaged for the wet duration using Equation (4.10). The continuity equation (4.8) yields

$$\frac{3\sqrt{\pi}\,\alpha}{4}\,\overline{h}\left(\frac{g\,\overline{h}}{P_w}\right)^{0.5} + U_s\,\overline{h} = q_o \tag{4.16}$$

After lengthy algebra, the momentum equation (4.9) is expressed as

$$\frac{d}{dx}\left(B\frac{g\,\overline{h}^2}{P_w}+\frac{q_0^2}{\overline{h}}\right)=-g\,S_b\,\overline{h}-\frac{f_b}{2}\,\alpha^2\,g\,\overline{h}\,G_b(r) \tag{4.17}$$

with

$$B=\left(2-\frac{9\pi}{16}\right)\alpha^2+1\ ;\quad r=\frac{3\sqrt{\pi}}{4}\,\frac{U_s\overline{h}}{q_o-U_s\overline{h}} \tag{4.18}$$

where the parameter B is related to the momentum flux term on the left hand side of Equation (4.9). The function $G_b(r)$ in Equation (4.17) is given by

$$\begin{aligned} G_b(r) &= 1+\sqrt{\pi}\,r+r^2 && \text{for} \quad r\geq 0 \\ G_b(r) &= 2\,exp\,(-r^2)-r^2-1+\sqrt{\pi}\,r\,[2\,erf(r)+1] && \text{for} \quad r<0 \end{aligned} \tag{4.19}$$

where erf is the error function. The function G_b increases monotonically with the increase of r and $G_b = 0$ and 1 for $r = -0.94$ and 0.0. For $r < -1.5$, $G_b \simeq -(1+\sqrt{\pi}\,r+r^2)$.

Equations (4.16) and (4.17) are used to predict the cross-shore variation of $\overline{h}$ and U_s for assumed q_o where σ_η, $\overline{U}$, and σ_U are computed using Equations (4.12), (4.14) and (4.15), respectively. It is necessary to estimate the wet probability P_w empirically. To simplify the integration of Equation (4.17), the following formula is adopted:

$$P_w=\left[(1+A)\left(\frac{\overline{h}_1}{\overline{h}}\right)^n-A\left(\frac{\overline{h}_1}{\overline{h}}\right)^3\right]^{-1}\ ;\quad A=\frac{q_o^2}{Bg(\overline{h}_1)^3} \tag{4.20}$$

where $\overline{h}_1$ = mean water depth at the location of $x = x_1$ where $P_w = 1$; n = empirical parameter for P_w; A = parameter related to the rate q_o normalized by the depth $\overline{h}_1$ where water is present always. The transition from the wet ($P_w = 1$ always) zone to the wet and dry ($P_w < 1$) zone may be taken at $x_1 = x_{SWL}$ where x_{SWL} is the cross-shore location of the still water shoreline of an emerged crest. Figure

4.1 illustrates the notations used in the following where the crest location x_c is the highest and most landward location. Equation (4.20) is assumed to be valid on the upward slope in the region of $x_1 \leq x \leq x_c$. It is noted that ponding of water in the trough zone near $x = x_2$ is neglected in the present version of CSHORE.

Integration of Equation (4.17) for P_w given by Equation (4.20) for the upward slope starting from $\overline{h} = \overline{h}_2$ at $x = x_2$ yields $\overline{h}(x)$

$$B_n \left(1 + A\right) \overline{h}_1 \left(\frac{\overline{h}_1}{\overline{h}_2}\right)^{n-1} \left[\left(\frac{\overline{h}_2}{\overline{h}}\right)^{n-1} - 1\right] = z_b\left(x\right) - z_b\left(x_2\right) + \frac{\alpha^2}{2} \int_{x_2}^{x} f_b \, G_b \, dx \quad (4.21)$$

where $B_n = B(2-n)/(n-1)$; and $z_b(x)$ = bottom elevation at the cross-shore location x. If no downward slope exists in the region of $x_1 \leq x \leq x_c$, the starting location x_2 is taken as $x_2 = x_1$ and $\overline{h}_2 = \overline{h}_1$ in Equation (4.21). The mean water depth $\overline{h}$ at given x is computed by solving Equation (4.21) iteratively where the function G_b given by Equation (4.19) depends on r defined in Equation (4.18). The empirical parameter n is taken to be in the range of $1 < n < 2$ so that $B_n > 0$. Kobayashi et al. (2010) calibrated n using 107 tests on wave overtopping of a dike in the form of $n = 1.01 + 0.98\left[tanh\left(A\right)\right]^{0.3}$ where $1.01 \leq n \leq 1.99$.

On the downward slope in the region of $x_1 < x < x_c$ or in the region of $x > x_c$, the wet probability P_w is assumed to be constant

$$P_w = \text{constant} = P_3 \quad (4.22)$$

where P_3 is the computed wet probability at the seaward end of the downward slope located at $x = x_3$ in Figure 4.1. Substituting Equation (4.22) into Equation (4.17) and integrating the resulting equation from x_3 to x, the mean depth $\overline{h}\left(x\right)$ is

expressed as

$$\frac{\overline{h}}{\overline{h}_3} - 1 + \frac{9\pi\alpha^2}{64B}\left[\left(\frac{\overline{h}_3}{\overline{h}}\right)^2 - 1\right] = \frac{P_3}{2B\overline{h}_3}\left[z_b\left(x_3\right) - z_b\left(x\right) - \frac{\alpha^2}{2}\int_{x_3}^{x} f_b\, G_b\, dx\right] \quad (4.23)$$

where $\overline{h}_3$ is the computed mean depth at $x = x_3$.

The wave overtopping rate q_o is predicted by imposing $U_s = 0$ in Equation (4.16) at the crest location x_c

$$q_o = \frac{3\sqrt{\pi}\,\alpha}{4}\,\overline{h}_c\left(\frac{g\overline{h}_c}{P_c}\right)^{0.5} \qquad \text{at} \quad x = x_c \quad (4.24)$$

where $\overline{h}_c$ and P_c are the computed mean depth $\overline{h}$ and wet probability P_w at x_c. The mean depth $\overline{h}$ in the region of $x > x_c$ is given by Equation (4.23) with $\overline{h}_3 = \overline{h}_c$ and $P_3 = P_c$.

For assumed q_o, the landward marching computation of $\overline{h}$, σ_η, $\overline{U}$, and σ_U is initiated using the wet model from the seaward boundary $x = 0$ to the landward limit located at $x = x_r$. The landward marching computation is continued using the wet and dry model from the location of $x = x_{SWL}$ where $\overline{h} = \overline{h}_1$ to the landward end of the computation domain or until the mean depth $\overline{h}$ becomes less than $0.001\,cm$. The rate q_o is computed using Equation (4.24). This landward computation starting from $q_o = 0$ is repeated until the difference between the computed and assumed values of q_o is less than 1%. This convergence is normally obtained after several iterations. The computed values of $\overline{h}$, σ_η, $\overline{U}$, and σ_U by the two different models in the overlapping zone of $x_{SWL} < x < x_r$ (see Figure 4.1) are averaged to smooth the transition from the wet zone to the wet and dry zone.

4.3 Sediment Transport Model

The above time-averaged probabilistic model may not be very accurate but provides the hydrodynamic input required for the following sediment transport

model. For the prediction of sediment transport on beaches, the effect of a roller on the steep front of a breaking wave is included in the combined wave and current model based on Equations (4.1) - (4.7) because the roller effect increases the offshore return current and improves the agreement of the measured and computed profile evolutions (Kobayashi et al., 2008). For coastal structures with steeper slopes, the roller effect does not necessarily improve the accuracy of the predicted wave overtopping rate probably because the roller does not develop over a relatively short distance on the steep slope. The equation of roller energy is used to compute the cross-shore variations of the roller volume flux and its energy dissipation rate D_r in the same way as in the computation of dune erosion made by Kobayashi et al. (2009) for the case of no overwash.

Kobayashi et al. (2010) compared CSHORE with 207 tests for wave overtopping and overflow on fixed levees as well as 8 data sets for dune profile evolution with no or minor overwash. The agreement was mostly within a factor 2. However, their model underpredicts the major overwash events in the present experiment. The computed values of the bedload transport rate q_b and the suspended load transport rate q_s indicate that suspended load is dominant for this experiment. Consequently, the formula for q_s is modified. In the following, the sediment transport formulas proposed by Kobayashi et al. (2008) for the wet zone are summarized and modified for the wet and dry zone including major overwash.

The probability P_b of sediment movement under the Gaussian velocity U in the wet zone is estimated assuming that the sediment movement occurs when the absolute value of the instantaneous bottom shear stress exceeds the critical shear stress corresponding to the critical Shields parameter of 0.05. The probability P_s of sediment suspension is estimated assuming that sediment suspension occurs when the turbulent velocity associated with the instantaneous energy dissipation rate due to bottom friction exceeds the sediment fall velocity. If the estimated P_s exceeds

P_b, use is made of $P_s = P_b$ to ensure that sediment suspension occurs only when sediment movement occurs.

The time-averaged bedload transport rate q_b is expressed as

$$q_b = b\, P_b\, G_s\, \sigma_U^3 \,/\, [g\,(s-1)] \tag{4.25}$$

where b = empirical bedload parameter; G_s = empirical function of the bottom slope S_b and the upper limit 0.63 of the sand slope; and s = sediment specific gravity. The bedload parameter b has been calibrated to be in the range of 0.001 - 0.004 using available water tunnel and flume tests on horizontal bottoms for which $G_s = 1$. The computed profile evolutions and transport rates presented in the following are based on $b = 0.002$ (Kobayashi et al., 2009) but are not very sensitive to b because suspended load is computed to be dominant.

The time-averaged cross-shore suspended sediment transport rate q_s is expressed as

$$q_s = \left(a\overline{U} + a_o U_o\right) V_s \tag{4.26}$$

with

$$U_o = \frac{q_o}{\overline{h}} \tag{4.27}$$

$$V_s = P_s\, V_{Bf} \left(1 + S_b^2\right)^{0.5} \tag{4.28}$$

$$V_{Bf} = \frac{e_B D_B + e_f D_f}{\rho\, g\,(s-1)\, w_f} \tag{4.29}$$

where a = suspended load parameter of the order of 0.2 under the action of waves and wave-induced currents; a_o = empirical parameter with $a_o = 0$ corresponding to the computations carried out by Kobayashi et al. (2010); U_o = onshore current due to the wave overtopping rate q_o, which is significant only in the zone of very small water depth $\overline{h}$; V_s = suspended sediment volume per unit horizontal area; V_{Bf} = potential suspended sediment volume on a horizontal bottom when $P_s = 1$; e_B and

e_f = suspension efficiencies for the energy dissipation rates D_r and D_f, previously calibrated as $e_B = 0.005$ and $e_f = 0.01$; and w_f = sediment fall velocity.

Kobayashi et al. (2009) adjusted the parameter $a = \left(0.2 + \sqrt{S_b/0.63}\right)$ for the upward slopes $S_b > 0$ to increase the offshore suspended sand transport where the return (undertow) current $\overline{U}$ is negative (offshore). The version of CSHORE used by Kobayashi et al. (2009, 2010) did not include the overtopping term $a_o U_o V_s$ in Equation (4.26). Overwash was empirically modeled by setting $a = 1$ in the region of $\overline{U} > 0$ where unidirectional flow over the dune crest was assumed due to lack of measured overwash data. The adjustment for $a = 1$ improved the agreement with available profile change data for minor overwash. Overtopping and overwash rates were measured in the present experiment, leading to the modified suspended sediment transport equation in Equation (4.26). The calibrated value of the empirical parameter a_0 for the present experiment ranges from 1.3 to 1.8 (see Chapter 5) and can be specified in the CSHORE input file. For other cases and field data a_o needs to be adjusted according to the severity of overwash. Chapter 6 compares the present version of CSHORE with the laboratory and field profile data utilized by Kobayashi et al. (2010).

Kobayashi et al. (2009) included an intuitive scarping procedure for the steep slope $S_b > 0.63$ exposed to occasional wave runup because Equations (4.25) and (4.26) were proposed for the wet zone seaward of the mean water shoreline located at $x = x_r$ in Figure 4.1. For the wet and dry zone added to the present version of CSHORE, the probability density function $f(h)$ of the instantaneous water depth h is assumed to be exponential and given by Equation (4.10). The instantaneous velocity U in the wet and dry zone is assumed to be expressed by Equation (4.13).

The probability P_b of sediment movement is obtained for the probability distribution of U based on Equations (4.10) and (4.13). The movement of sediment particles represented by the median diameter d_{50} is assumed to occur when the

instantaneous bottom shear stress given by $0.5\,\rho\,f_b\,U^2$ exceeds the critical shear stress $\rho\,g\,(s-1)\,d_{50}\,\psi_c$ with the critical Shields parameter $\psi_c = 0.05$. The probability P_b of sediment movement is then the same as the probability of $|U| > U_{cb}$ with $U_{cb} = \left[2\,g\,(s-1)\,d_{50}\,\psi_c\,f_b^{-1}\right]^{0.5}$ and is given by

$$P_b = P_w \qquad \text{for } U_s > U_{cb} \tag{4.30}$$

$$P_b = P_w\,exp\left[-\frac{P_w\,(U_{cb}-U_s)^2}{\alpha^2\,g\,\overline{h}}\right] \qquad \text{for } |U_s| \leq U_{cb} \tag{4.31}$$

$$P_b = P_w\left\{1 - exp\left[-\frac{P_w\,(U_{cb}+U_s)^2}{\alpha^2\,g\,\overline{h}}\right] + exp\left[-\frac{P_w\,(U_{cb}-U_s)^2}{\alpha^2\,g\,\overline{h}}\right]\right\} \text{ for } -U_s > U_{cb} \tag{4.32}$$

where the upper limit of P_b is the wet probability P_w because no sediment movement occurs during the dry duration. On the other hand, sediment suspension is assumed to occur when the instantaneous turbulent velocity estimated as $(f_b/2)^{1/3}|U|$ exceeds the sediment fall velocity w_f. The probability P_s of sediment suspension is then the same as the probability of $|U| > U_{cs}$ where $U_{cs} = w_f(2/f_b)^{1/3}$. The probability P_s is given by Equations (4.30) - (4.32) with U_{cb} replaced by U_{cs}.

The bedload transport rate q_b is estimated using Equation (4.25) where the parameter b in the wet and dry zone is chosen so that the values of q_b computed for the two different zones are the same at the still water shoreline located at $x = x_{SWL}$. The suspended sediment transport rate q_s is estimated using Equation (4.26) where V_{Bf} in the wet and dry zone is assumed to be constant and chosen so that the suspended sediment volume V_s is continuous at $x = x_{SWL}$. The assumption of constant V_{Bf} may be reasonable because suspended sediment in the swash zone tends to remain suspended. The suspended sediment volume V_s per unit horizontal area given in Equation (4.28) normally decreases landward because the probability P_s of sediment suspension is limited by the wet probability P_w which decreases landward.

Finally, the cross-shore sediment transport rates q_s and q_b computed for the wet zone and the wet and dry zone are averaged in the overlapping zone of $x_{SWL} \leq x \leq x_r$ for the smooth transition between the two zones. The landward limit of the computation is taken as the location of the mean water depth $\overline{h} = d_{50}$ or the landward end of the computation domain. The continuity equation of bottom sediment is solved numerically to obtain the bottom elevation at the next time level (Kobayashi et al., 2009). This computation procedure is repeated starting from the initial bottom profile until the end of each profile evolution computation. The computation time is on the order of 10^{-3} of the profile evolution time.

Chapter 5

COMPARISON OF NUMERICAL MODEL WITH EXPERIMENT

This chapter shows the comparison of CSHORE with the collected experimental data (Chapter 3). Input parameters for CSHORE are discussed briefly before the comparison of the hydrodynamics, profile evolution, wave overtopping and overwash rates. Additional computed results on hydrodynamics and sediment transport are presented in Appendices A and B.

5.1 Input Parameters

The numerical model CSHORE (Chapter 4) is used to predict hydrodynamic variables, profile evolution, overtopping, and overwash rates measured in the experiment. Input parameters are listed in Table 5.1. They are the same as those used by Kobayashi et al. (2009) except for the breaker ratio parameter γ which is reduced from 0.8 to 0.6 to improve the agreement between the measured and computed free surface standard deviation σ_η. This reduction of γ may be related to the gentler beach slope in the present experiment. Comparison is made with detailed laboratory measurements of free-surface elevations at 70 cross-shore locations over a barred beach profile (Boers, 1996) in a similar sand-bed wave flume as shown in Figure 5.1 where the agreement is better for $\gamma = 0.6$. In addition, the empirical parameter a_o given in Equation (4.26) needs to be specified as input. Calibration of a_o for the present experiment using the measured profile evolution, the measured

overtopping rate q_o and the overwash rate $q_{bs} = (q_b + q_s)$ at the vertical wall has yielded values of $a_o = 1.3$, 1.7, and 1.8 for the BD, WD, and SD tests, respectively. The mean value of a_o is 1.6 for this experiment.

Uniform nodal spacing ($\Delta x = 2\,cm$) is used and the bottom elevation at the landward end of the computation domain (vertical wall crest) is fixed for the computations. Apart from the parameters listed in Table 5.1, numerical model input includes the initial bottom elevation $z_b(x)$ and the measured values of T_p, $\overline{\eta}$, and σ_η at $x = 0$ corresponding to the location of WG1 in the experiment.

Table 5.1: *CSHORE input parameters for overwash experiment.*

Parameter	Value	Description
Δx	$0.02\ m$	cross-shore nodal spacing
γ	0.6	breaker parameter
d_{50}	$0.18\ mm$	median sand diameter
w_f	$0.02\ m$	fall velocity
s	2.6	specific gravity
e_B	0.005	breaking wave efficiency
e_f	0.01	bottom friction efficiency
a	0.2	suspended load parameter for slope $S_b = 0$
a_o	$1.3 - 1.8$	overtopping parameter (calibrated)
$tan(\varphi)$	0.63	limiting sand slope
b	0.002	bedload parameter

5.2 Hydrodynamics

Measured cross-shore variations of $\overline{\eta}$, σ_η, $\overline{U}$, σ_U, and P_w (Tables 3.4 - 3.13) are compared to CSHORE results for all 45 runs comprising tests BD, WD, and SD.

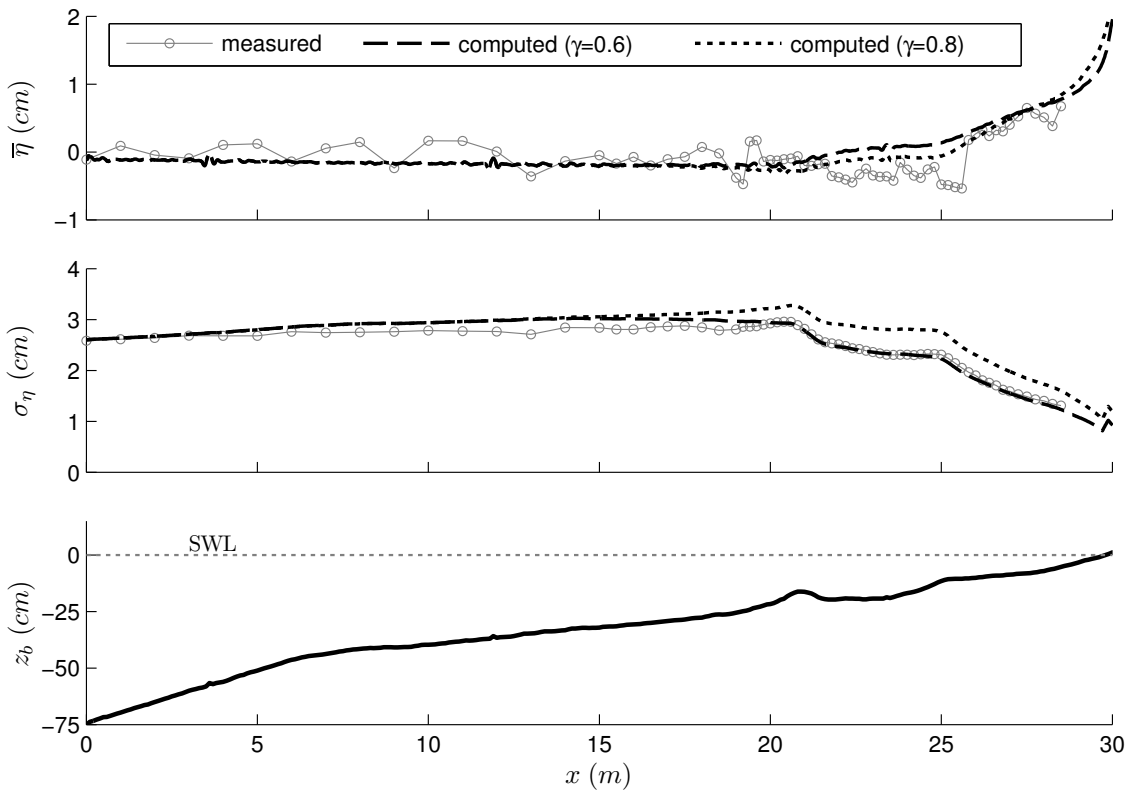

Figure 5.1: *Comparison of CSHORE with detailed hydrodynamic measurements over a barred sand beach in a wave flume (Boers, 1996). The standard deviation σ_η is best represented for $\gamma = 0.6$.*

Additionally, the measured and computed cross-shore variations of the mean water depth $\overline{h}$ and the ratio $\sigma_\eta/\overline{h}$ are shown. The individually calibrated values of a_o for each test are used for the hydrodynamic comparisons. In the following figures, circles represent measured values during each 400-s run and solid lines denote computed values at the end of each run for the entire computation domain ($x = 0 - 19.9\,m$). Circles and solid lines are shaded from light gray to black according to run number in order to illustrate changes over time.

Figures 5.2, 5.3, and 5.4 show the comparison of $\overline{\eta}$, $\overline{h}$, σ_η, and ratio $\sigma_\eta/\overline{h}$ for the BD, WD, and SD tests, respectively. The measured values of $\overline{\eta}$, σ_η, and T_p at $x = 0$ are specified as the boundary conditions for each run. Hence, the agreement between measured and computed values at wave gauges WG1-WG3 is excellent. Only the measured values of σ_η at WG3 are up to 5 mm higher than expected. WG3 was mounted on a threaded rod connected to a stepper motor for calibration (Section 2.2). This fixture was less sturdy than the other gauge fixtures which may have resulted in some gauge vibration during a run, consequently leading to slightly larger σ_η values. This problem has been fixed for future experiments.

For all three tests the agreement of measured and computed $\overline{\eta}$ and $\overline{h}$ is very good at all WG locations. On the dune, the computed mean depth $\overline{h} = (\overline{\eta} - z_b)$ becomes less than $1\,cm$. Inspecting the values for the BD test (Figure 5.2) in more detail shows that the measured free surface standard deviation σ_η, representing the wave height, decreases landward of WG4 at $x = 8.3\,m$ due to irregular wave breaking but shows a local maximum at the foot of the berm (WG7 at $x = 17.1\,m$). This peak becomes less prominent with the profile evolution and smoothing. The computed σ_η remains in good agreement at WG4. Landward of WG5 the model starts to underpredict σ_η with a maximum deviation of less than $6\,mm$ from the measured data at the most landward gauge in each run. This deviation is related to the rapidly changing profile in the berm and dune region. The first data point

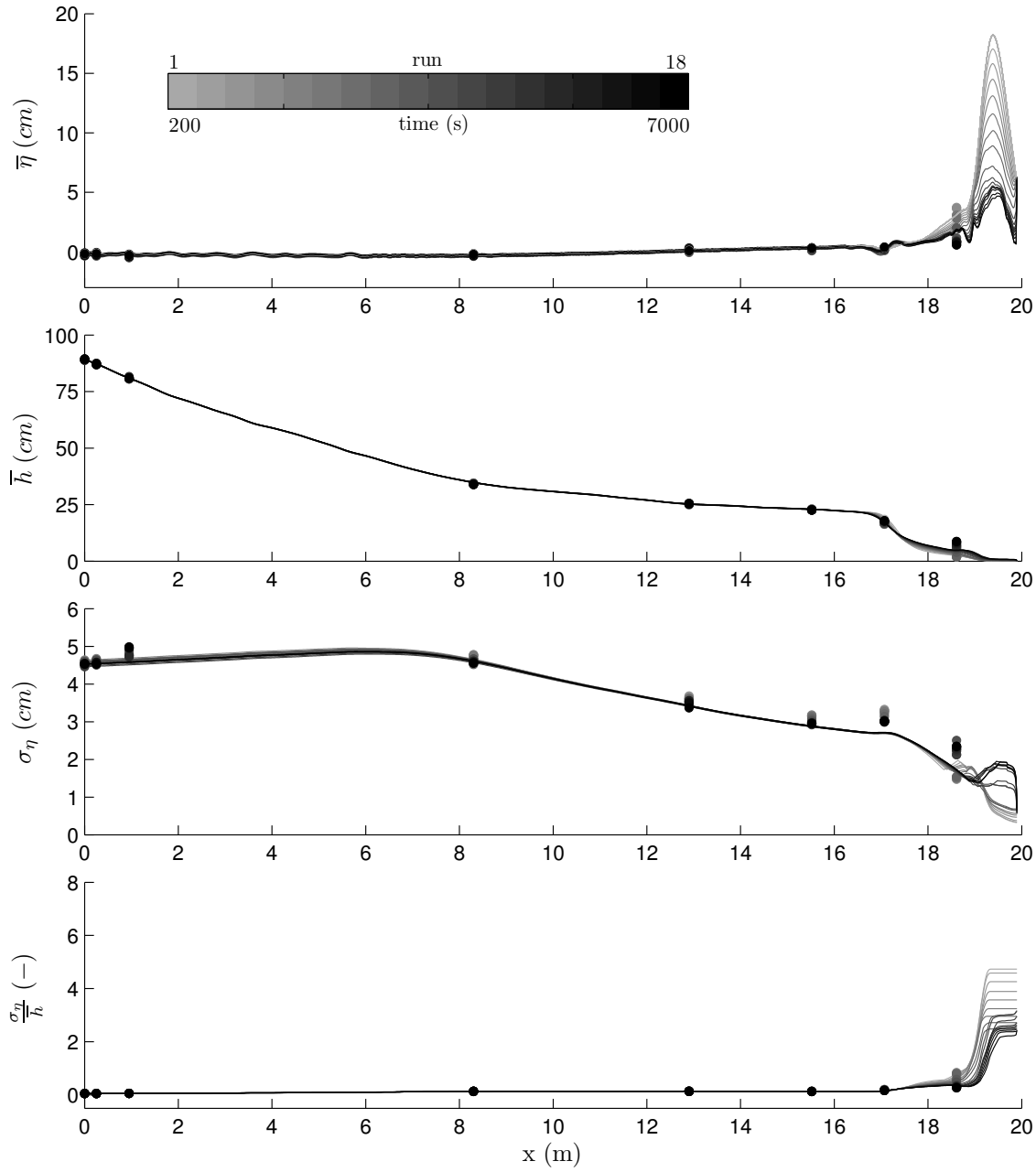

Figure 5.2: *Measured (circles) and computed (lines) mean free surface elevation $\overline{\eta}$, mean water depth $\overline{h}$, free surface standard deviation σ_η, and ratio $\sigma_\eta/\overline{h}$ for all 18 runs of the BD test. Gray shades denote run number and corresponding time at the middle of each 400-s run.*

(BD1) for WG8 is not available due to gauge failure during BD1.

Despite the large initial profile changes in the WD test (see Section 5.3), the comparison of CSHORE with the measured data for $\overline{\eta}$, $\overline{h}$, and $\sigma_\eta/\overline{h}$ (Figure 5.3) shows exceptionally good agreement, even for WG8 ($x = 18.6\,m$) which was initially located on the dune crest $20\,cm$ above SWL where z_b changed by more than $10\,cm$ during WD1. The measured values of σ_η for the WD test are represented fairly well up to WG5. At WG6, WG7, and WG8 the model slightly underpredicts σ_η by up to $6\,mm$. Only run WD1 exhibits much larger underprediction at WG7 and WG8 due to the underpredicted rapid dune profile changes at these locations as explained later in this chapter. The agreement improves significantly after WD1.

Test SD exhibits the least profile changes in front of the dune since the initial slope is close to equilibrium for the present wave conditions. Hence, the agreement between measured data and computed values is good for all runs (Figure 5.4). Similarly to the BD and WD tests, the measured local maximum in σ_η at WG7 is underpredicted by less than $7\,mm$ in all runs of the SD test. Errors for σ_η at WG8 fall in the same range but with larger underprediction towards the end of the test. Measured values of $\overline{\eta}$, $\overline{h}$, and $\sigma_\eta/\overline{h}$ are predicted very well for WG1 - WG7 with only minor discrepancies at WG8. The measured and computed ratios $\sigma_\eta/\overline{h}$ improve in agreement towards the end of the SD test since CSHORE results for $\overline{h}$ change from underprediction during the first few runs to overprediction at the end of the test while the computation for σ_η is slightly below the measurements in all runs. It should be noted that the hydrodynamic variables in the zone of the large profile change ($18.7\,m < x < 19.9\,m$) were not measured although the computed variations are large in this zone.

Figures 5.5, 5.6, and 5.7 show the mean and standard deviation of the measured cross-shore velocity component u at the two ADV instrument locations for

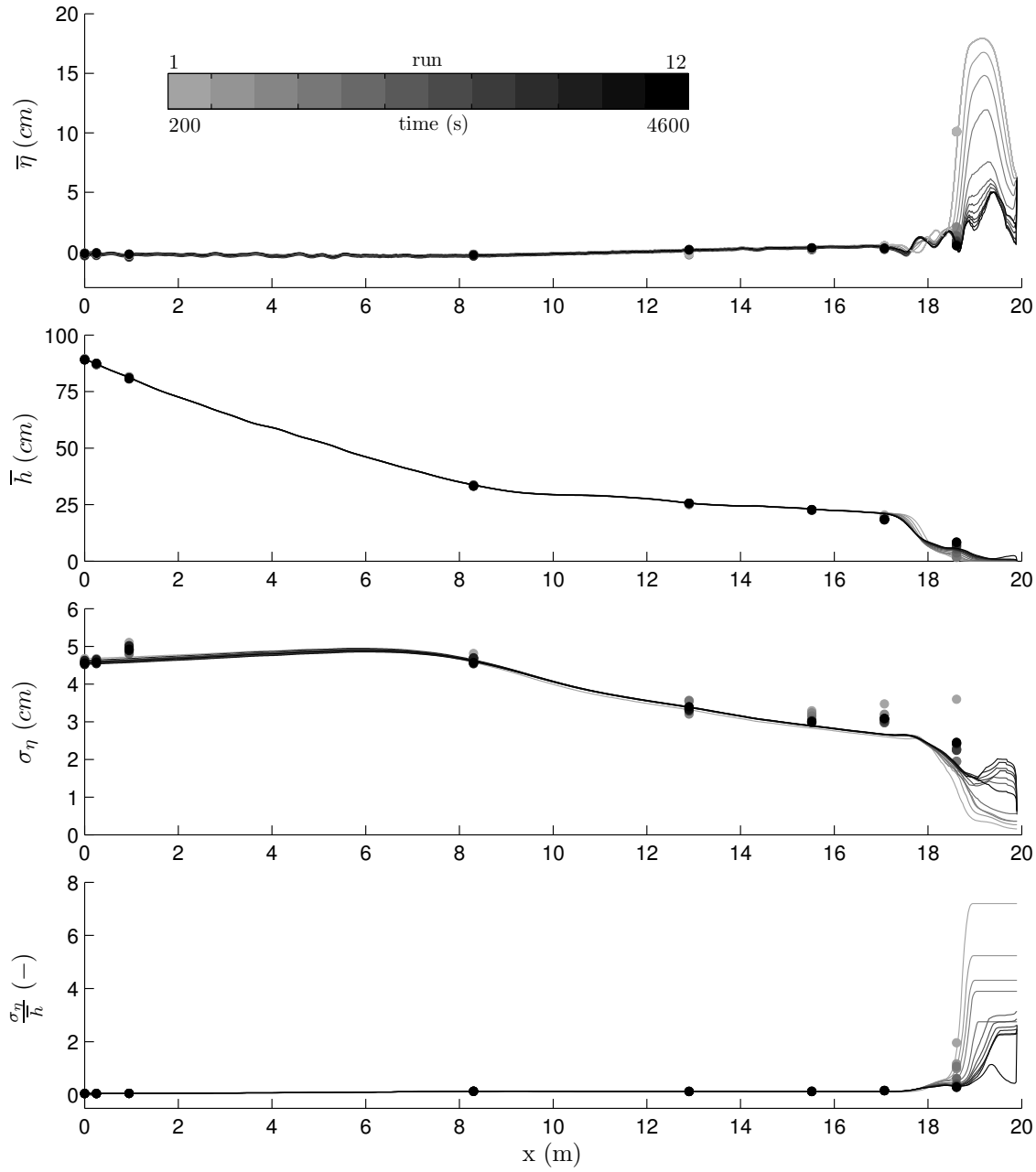

Figure 5.3: *Measured (circles) and computed (lines) mean free surface elevation $\overline{\eta}$, mean water depth $\overline{h}$, free surface standard deviation σ_η, and ratio $\sigma_\eta/\overline{h}$ for all 12 runs of the WD test. Gray shades denote run number and corresponding time at the middle of each 400-s run.*

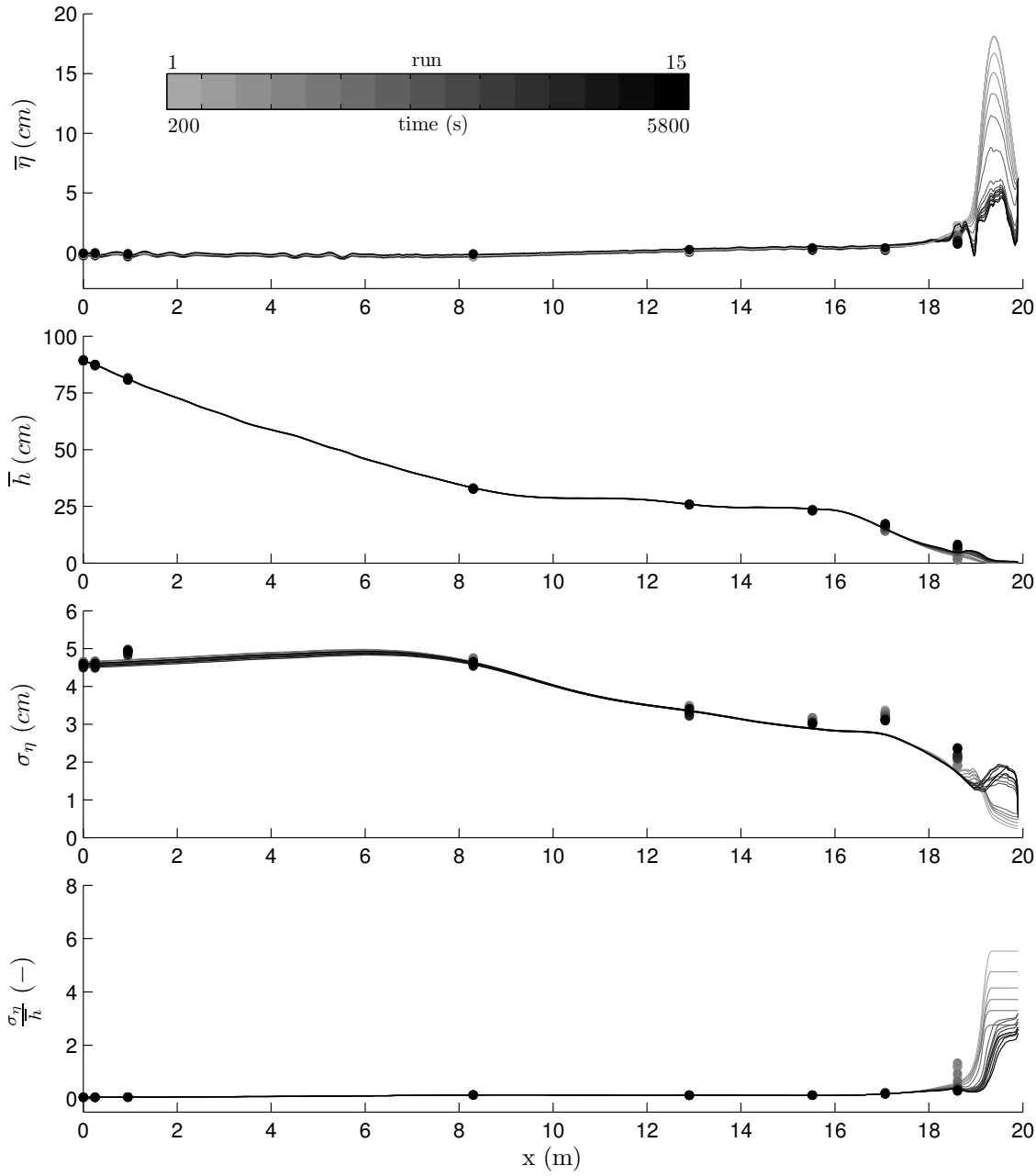

Figure 5.4: *Measured (circles) and computed (lines) mean free surface elevation $\overline{\eta}$, mean water depth $\overline{h}$, free surface standard deviation σ_η, and ratio $\sigma_\eta/\overline{h}$ for all 15 runs of the SD test. Gray shades denote run number and corresponding time at the middle of each 400-s run.*

every run of the BD, WD, and SD tests as circles. In addition, the computed cross-shore distribution of the mean $\overline{U}$ and standard deviation σ_U of the depth-averaged cross-shore velocity landward of $x = 12\,m$ are plotted as solid lines. The three figures show that the measured values of $\overline{U}$ at the locations of ADV1 ($x = 12.9\,m$) and ADV2 ($x = 17.0\,m$) are in good agreement with the computed results with only slight overprediction by less than $3\,cm/s$ in certain runs. Differences may be attributed to the fact that the measurements represent only a single point in the vertical velocity profile at 2/3 of the local water depth below SWL.

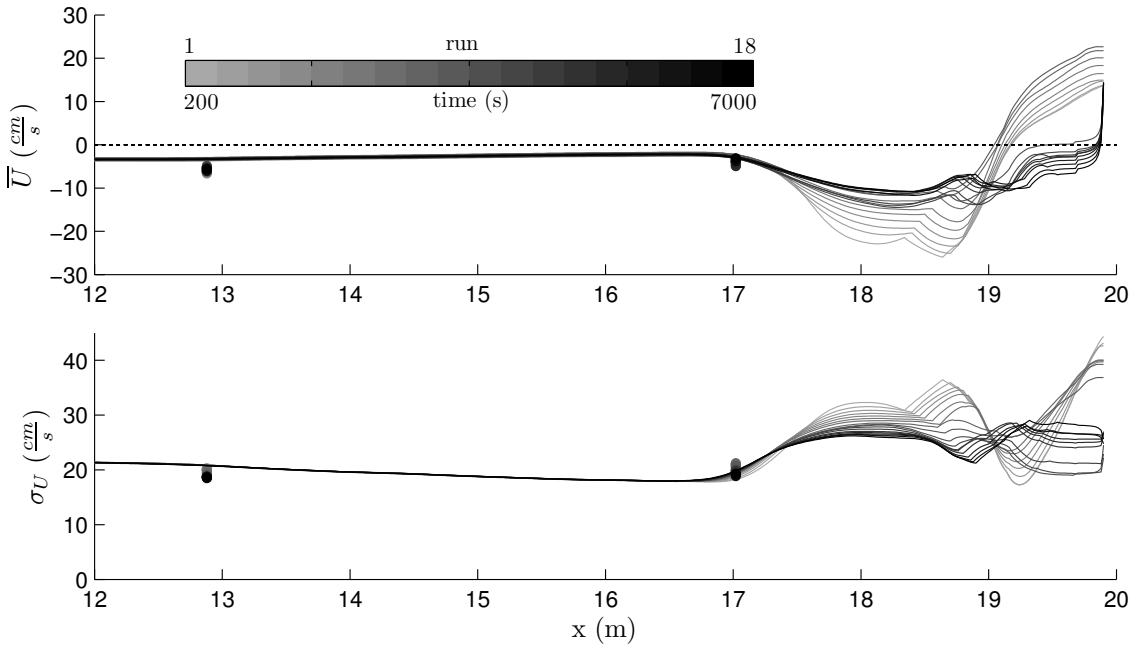

Figure 5.5: *Measured (circles) and computed (lines) mean and standard deviation of the cross-shore velocity U for all 18 runs of the BD test. The measured velocity at 2/3 of the local water depth below SWL is assumed to correspond to the computed depth-averaged velocity. Gray shades denote run number and corresponding time at the middle of each 400-s run.*

The computed offshore (negative) return current $\overline{U}$ is small on the beach and increases near the SWL shoreline before $\overline{U}$ becomes onshore (positive) on the dune due to overtopping. This cross-shore distribution of $\overline{U}$ is characteristic for phases

1 and 2 of the profile and overwash evolution (Table 3.17) and is visible in the top panels of all three figures. In phase 3, $\overline{U}$ remains mainly negative on the eroding beach in front of the increasingly exposed vertical wall. Only at the location of the wall does $\overline{U}$ change sign to positive (onshore) as a result of wave overtopping of the wall. The magnitude of the computed small negative return current on the seaward beach remains fairly constant in all runs of the three tests with values between -3 and $-4\,cm/s$. Landward of $x = 17\,m$ the computed values show significant variations in accordance with the rapidly changing dune profiles.

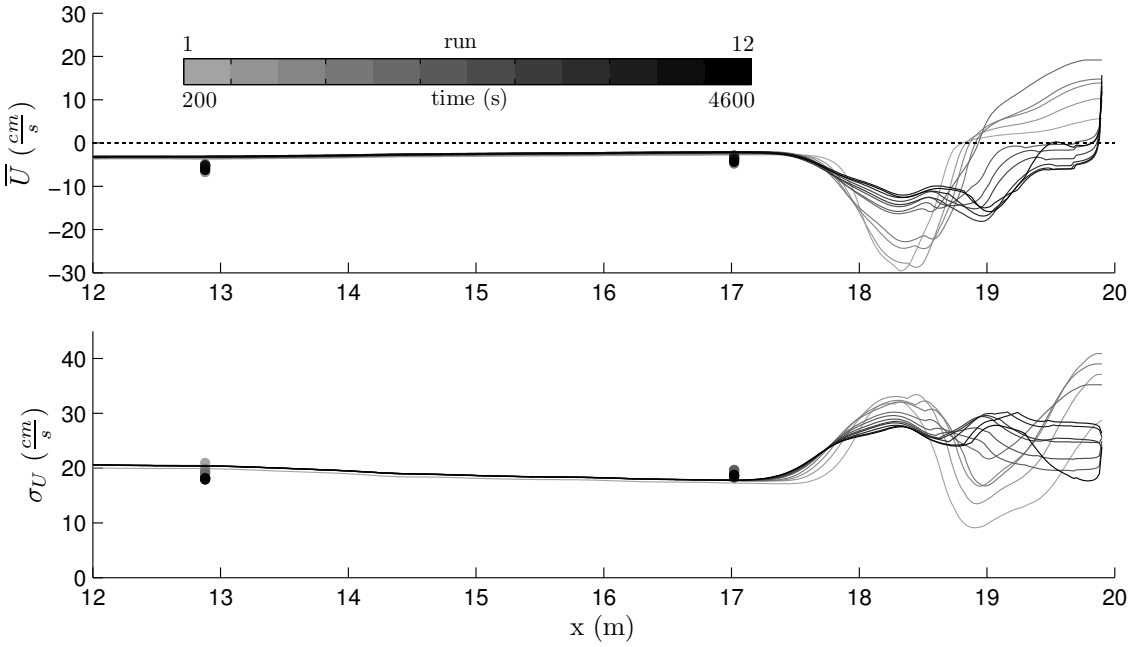

Figure 5.6: *Measured (circles) and computed (lines) mean and standard deviation of the cross-shore velocity U for all 12 runs of the WD test. The measured velocity at 2/3 of the local water depth below SWL is assumed to correspond to the computed depth-averaged velocity. Gray shades denote run number and corresponding time at the middle of each 400-s run.*

The velocity standard deviation σ_U decreases landward inside the surf zone and increases in very shallow water except in the vicinity of the dune crest where a drop occurs due to $U_s = 0$ in Equation (4.15). This drop becomes less pronounced

as the dune is eroded. Measured values of σ_U compare well to the computed results with maximum differences of less than $3\,cm/s$ at the ADV2 location ($x = 17\,m$) for the SD test (Figure 5.7) where the local water depth was smaller than for the BD and WD tests due to the sloping beach.

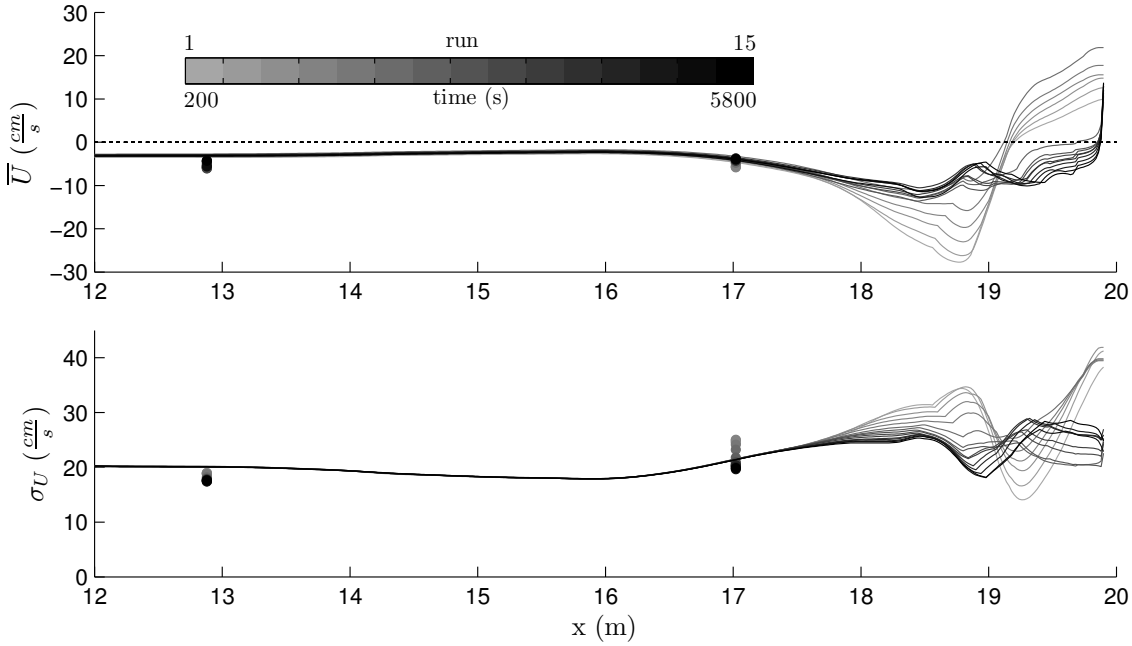

Figure 5.7: *Measured (circles) and computed (lines) mean and standard deviation of the cross-shore velocity U for all 15 runs of the SD test. The measured velocity at 2/3 of the local water depth below SWL is assumed to correspond to the computed depth-averaged velocity. Gray shades denote run number and corresponding time at the middle of each 400-s run.*

Figures 5.8, 5.9, and 5.10 display the comparison of measured and computed wet probability P_w landward of $x = 16\,m$ for the BD, WD, and SD tests, respectively. Conceptually, P_w is unity in the wet zone seaward of the SWL shoreline, decreases rapidly landward, and approaches a constant value landward of the dune crest in this experiment. Only WG8 during the first couple of runs in each test was located in the zone landward of the SWL shoreline where P_w is less than unity. The measured wet probability data at the WG8 location is based on the technique developed in Section

3.1.1 with results presented in Table 3.10. The computed cross-shore variations of P_w are calculated using Equations (4.20) and (4.22) for the wet and dry zone.

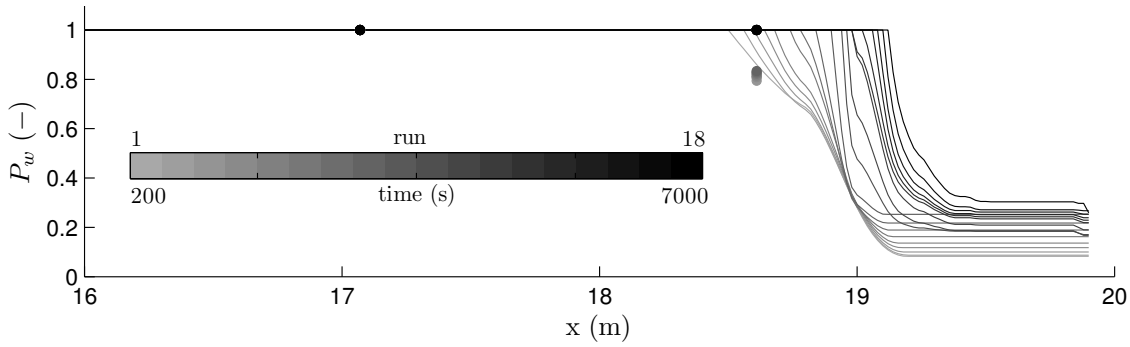

Figure 5.8: *Measured (circles) and computed (lines) wet probability P_w for all 18 runs of the BD test. Gray shades denote run number and corresponding time at the middle of each 400-s run.*

For the BD test (Figure 5.8) the computed P_w starts to decrease from unity close to the WG8 location for the first few runs and matches very well with the measured data. The drop in computed P_w value moves landward and happens more sudden as the test continues but the constant value on the backdune tends to increase with increasing run number due to the lowering of the profile. The rapid drop in computed P_w landward of the SWL shoreline is located slightly offshore from the WG8 location in WD1 and WD2 (Figure 5.9) due to the underpredicted erosion at the dune face. At the end of phase 2 (WD5) the drop occurs just landward of WG8 where P_w is still unity. The computed wet probability at WG8 is still unity in SD1 compared to a measured value of 0.88 (Table 3.10) since the drop in computed P_w values occurs about 15 cm landward of WG8.

In general, CSHORE is accurate enough to predict the measured hydrodynamic variables as was the case with previous comparisons. Discrepancies only occur at locations of poorly-predicted rapid profile change during the initial adjustment of the profiles in BD1 and WD1. More detailed measurements of free-surface elevation and flow velocities in the dune region are needed to improve CSHORE further.

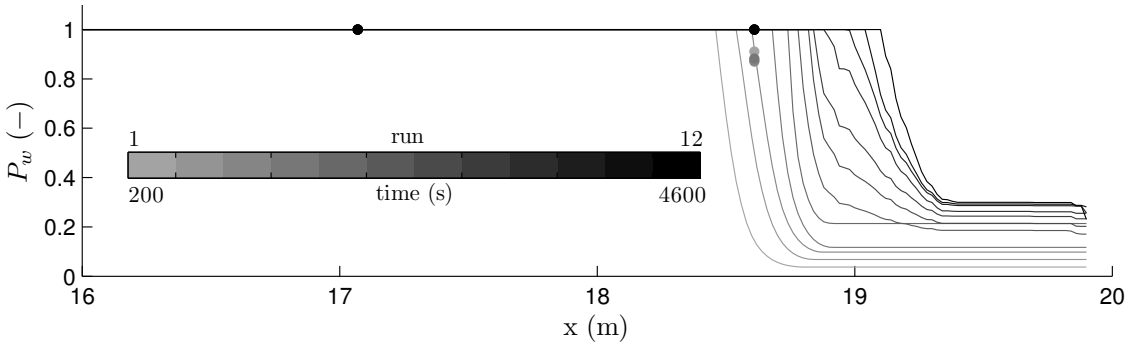

Figure 5.9: *Measured (circles) and computed (lines) wet probability P_w for all 12 runs of the WD test. Gray shades denote run number and corresponding time at the middle of each 400-s run.*

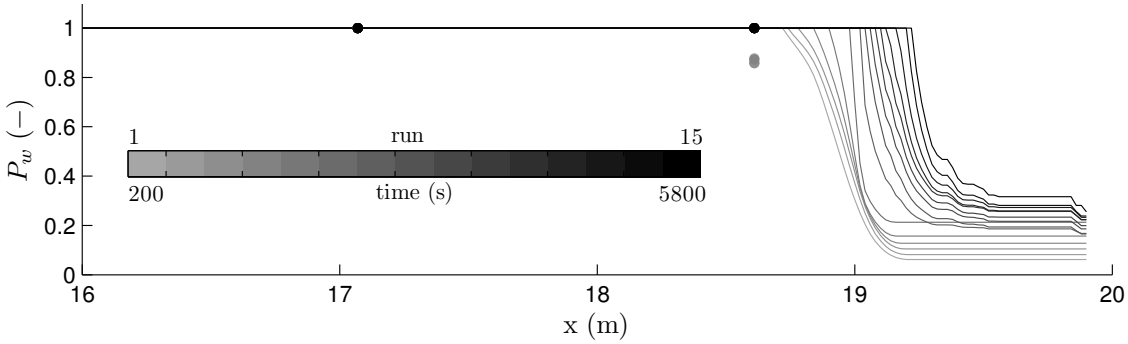

Figure 5.10: *Measured (circles) and computed (lines) wet probability P_w for all 15 runs of the SD test. Gray shades denote run number and corresponding time at the middle of each 400-s run.*

Additional computed cross-shore variations of hydrodynamic variables include energy flux and dissipation terms, radiation stress and bottom friction, intrinsic wave period, breaking wave fraction, and roller volume flux. These variables with no corresponding data are plotted in Appendix A for every run of the BD, WD, and SD tests.

5.3 Profile Evolution

Accurate profile evolution prediction is essential for assessing risks and predicting damages to coastal areas. Figure 5.11 compares the measured and computed bottom elevations at the end of phases 1, 2, and 3 for the BD, WD, and SD tests. Computed results corresponding to $a_o = 0$ in Equation (4.26) are represented by dashed lines. Neglecting the overtopping term $(a_o q_o/\overline{h})$ which becomes significant in very shallow water over the dune during the transition from minor to major overwash, leads to highly underpredicted dune profile changes. Including the overtopping term in the suspended sediment transport equation yields much better agreement for the profile evolution in phases 1 and 2. The overtopping parameter a_o was calibrated for the three tests based on the best combination of profile change and overwash rate prediction. Results using the calibrated values $a_o = 1.3$, 1.7, and 1.8 for the BD, WD, and SD tests, respectively, are displayed by dotted lines in Figure 5.11.

The modified CSHORE model predicts the profile evolution for phases 1 and 2 fairly well, but beach erosion in front of the exposed wall for phase 3 is underpredicted considerably. The reason for this underprediction may be related to the fact that the present numerical model does not account for the effects of the wall on the hydrodynamics and sediment transport on the beach in front of the exposed wall. The instrument deployment in this experiment, which was initially intended for phases 1 and 2 only, is not suited for examining the wall effects in phase 3.

Plotting the computed profiles using the average of the calibrated values for a_o shows that their evolution z_b is not sensitive to small changes in a_o within the

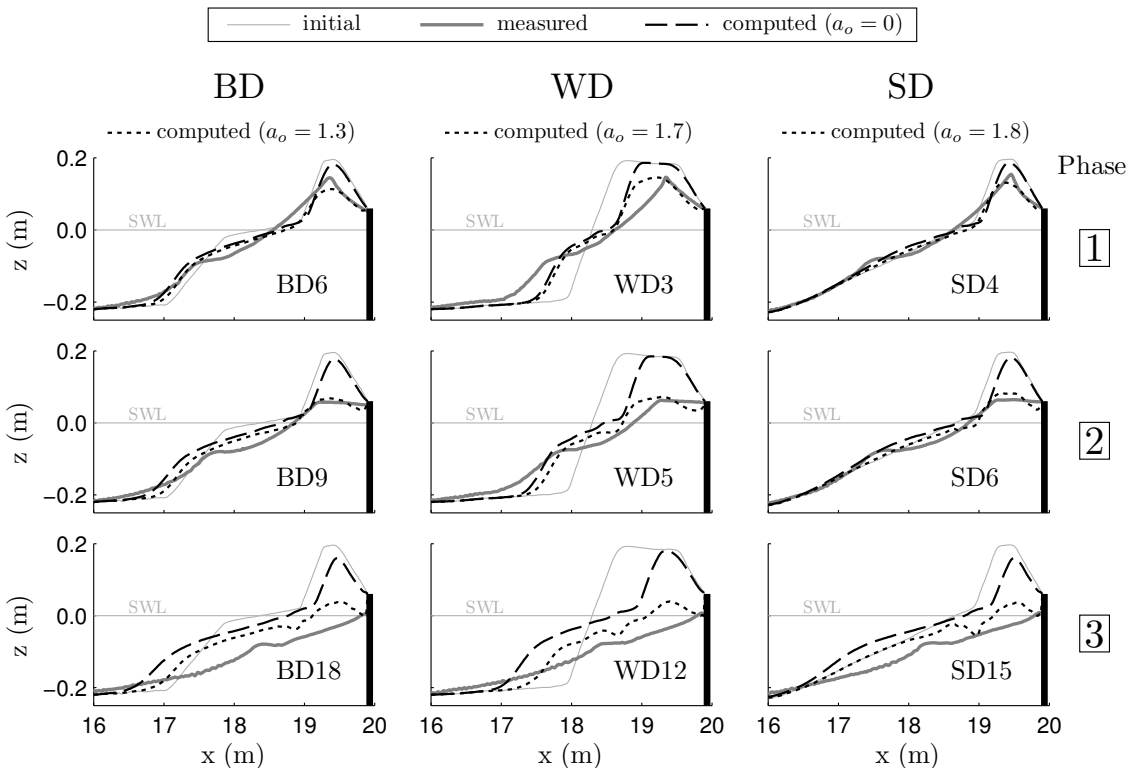

Figure 5.11: *Measured and computed dune profiles at the end of phases 1, 2, and 3 for BD (left), WD (middle), and SD (right) tests with and without parameter a_o. For $a_o = 0$ profile changes are highly underpredicted in this experiment with major overwash.*

calibrated limits (Figure 5.12). In fact, except for minor differences, the computed profile evolutions for $a_o = 1.6$ are almost identical to the results using the individually calibrated values of a_o ranging from 1.3 to 1.8 for the 3 tests.

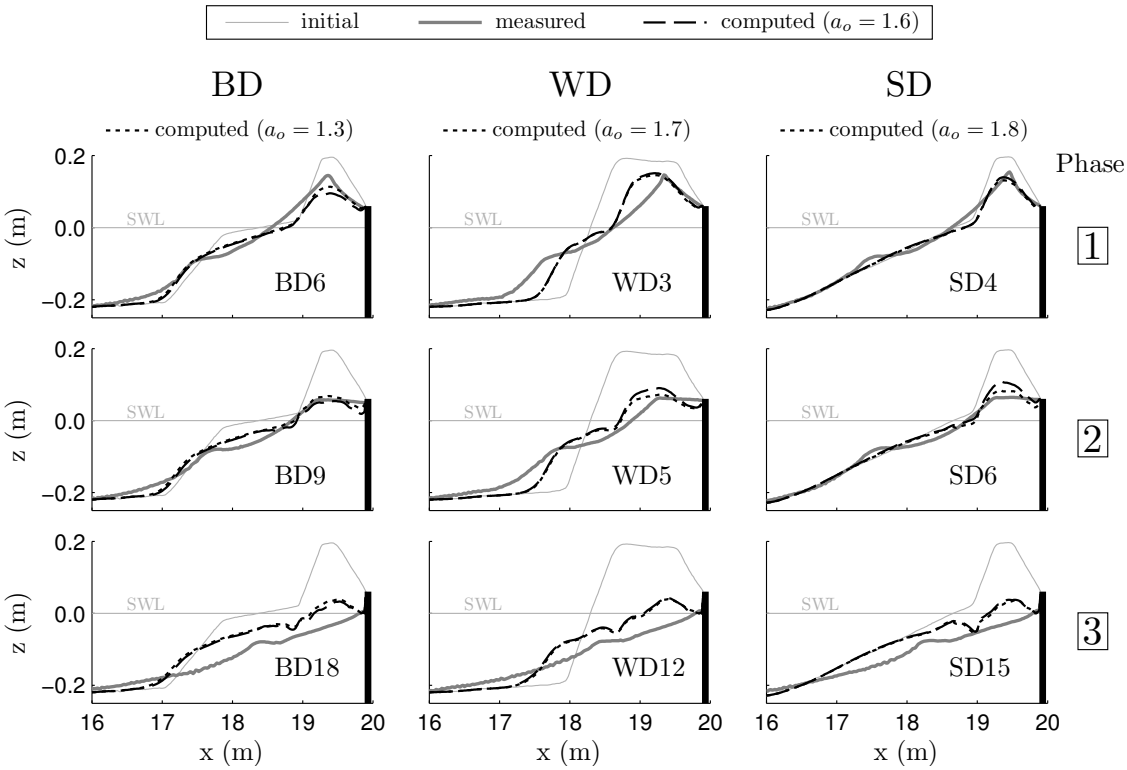

Figure 5.12: *Measured and computed dune profiles at the end of phases 1, 2, and 3 for BD (left), WD (middle), and SD (right) tests for individually calibrated and average calibrated values of a_o. The comparison of computed profiles using the average calibrated value of $a_o = 1.6$ with the individually calibrated values for each test shows that profile evolution is not sensitive to the choice of a_o within the specified limits of $1.3 \leq a_o \leq 1.8$.*

5.4 Wave Overtopping and Overwash Rates

The average wave overtopping rate q_o and sediment overwash rate q_{bs} during each 400-s run have been determined from the collected water and sand transported over the vertical wall behind the dune. In addition to q_o, CSHORE computes the cross-shore distribution of the bedload transport rate q_b and the suspended load transport rate q_s where $q_{bs} = (q_b + q_s)$ at the end of the computation domain corresponds to the measured sediment transport rate over the wall.

Figure 5.13 shows the measured and computed temporal variations of the wave overtopping rate q_o (top panels) and the sediment transport rate q_{bs} (bottom panels) for the BD, WD, and SD tests. Vertical lines demarcate evolution phases 1, 2, and 3 as listed in Table 3.17. The computed rates are displayed for $a_o = 0$ (dashed lines) and for the individually calibrated a_o values (dotted lines). Without the overtopping parameter, CSHORE cannot predict the rapid transition from minor to major overwash leaving the wave overtopping rate at a fairly constant value throughout each test. The sediment transport rate over the wall is practically non-existent. The calibrated overtopping parameter a_o yields a much better representation of the measured q_o and q_{bs}. Even though the numerical model tends to overpredict q_o and q_{bs} before the transition, and underpredicts q_{bs} after the transition, the transition from minor to major overwash is modeled more precisely, especially the magnitude and location of the peak for both rates.

For the BD test, computed q_o values are high initially but approach the measured value in phase 3 after the peak at the end of phase 2. The computed sediment transport rate follows the measured evolution fairly well but slightly underpredicts its peak right after phase 2. The WD test numerical results show a good representation of q_o, especially the magnitude of the constant overtopping rate during phase 3. Initial and peak q_{bs} values are very close to the measured ones but the drop in overwash transport rate after the initial WD run is not reproduced by the

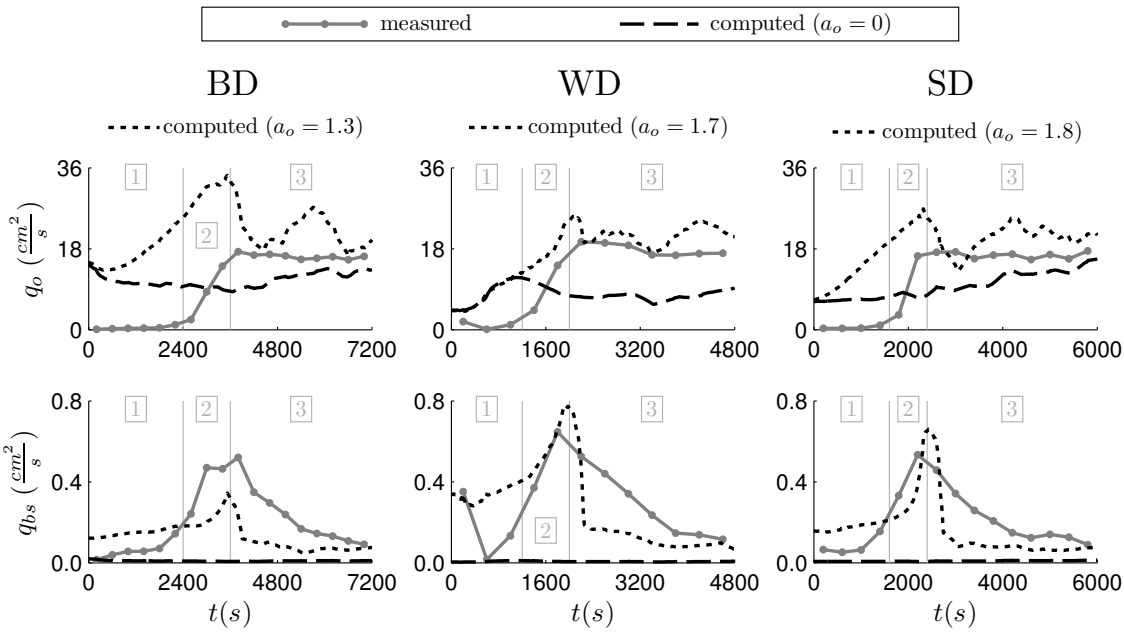

Figure 5.13: *Measured and computed wave overtopping rate q_o (top) and sand overwash rate q_{bs} (bottom) for BD (left), WD (middle), and SD (right) tests at the vertical wall with and without parameter a_o. Vertical lines demarcate the three evolution phases. Introducing the individually calibrated a_o for each test improves the agreement between measured and computed rates q_o and q_{bs}.*

model. The SD test comparison of the transport rates is similar to that of the WD test with very good representation of the constant overtopping rate in phase 3 and the transition and peak of the sediment transport rate in phase 2. The computed transition from minor to major overwash (phase 2) is sensitive to the parameter a_o as illustrated in Figure 5.14 in which computed results using the individually calibrated values of a_o are plotted together with results corresponding to the average a_o value of 1.6. Especially the time shift of the peak is evident.

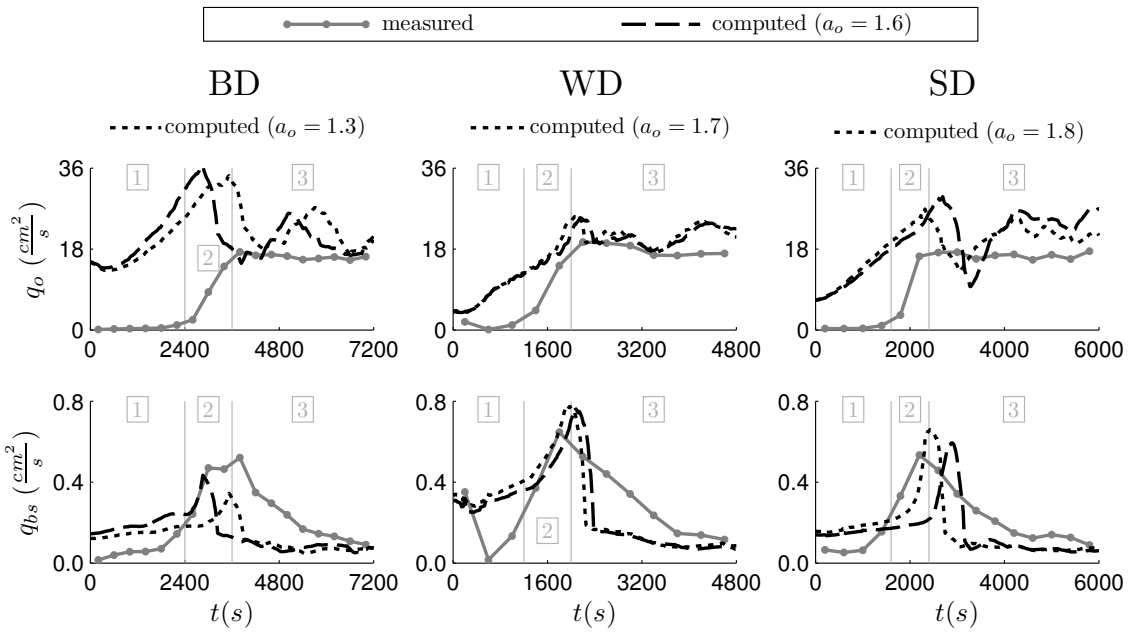

Figure 5.14: *Measured and computed wave overtopping rate q_o (top) and sand overwash rate q_{bs} (bottom) for BD (left), WD (middle), and SD (right) tests. Vertical lines demarcate the three evolution phases. The comparison of computed profiles using the average calibrated value of $a_o = 1.6$ with the individually calibrated values for each test shows that q_o and q_{bs} are more sensitive to the choice of a_o than the profile evolution is.*

Accurate prediction of q_o and q_{bs} is very difficult because of the small water depth and velocity above the moveable bed in the wet and dry zone, which is the reason why q_o and q_{bs} were measured in this experiment. Comparing the degree of

agreement in Figures 5.12 and 5.14, it is obvious that the prediction of both hydrodynamics and sediment transport is more difficult than the prediction of bottom elevation change alone. Further CSHORE results pertaining to sediment transport computations are presented in Appendix B. The cross-shore distribution of the sediment movement and suspension probabilities is plotted for every run of the BD, WD, and SD tests alongside with the volume of suspended sediment per unit area. In addition, the computed bedload q_b and suspended load q_s transport rates are plotted individually.

Chapter 6

VERIFICATION OF CSHORE WITH ADDITIONAL PROFILE DATA

Kobayashi et al. (2010) used the previous version of CSHORE to assess profile changes measured in two laboratory studies and at three field sites. The laboratory studies included two tests with no or minor overtopping by Kobayashi et al. (2009) and three dune erosion tests by van Gent (2008). The field measurements comprised pre- and post-storm surveys of Delaware and Maryland beaches (Wise et al., 1996). In the following, CSHORE is compared to these measured data to show that the present version of the program can predict profile evolution in the laboratory and in the field with similar accuracy as the previous version even if no or only little overtopping occurs. Increased flexibility in the present CSHORE is achieved by adjusting the parameter a_o to the prevailing overtopping and overwash conditions.

6.1 Laboratory Dune Data

Kobayashi et al. (2009) conducted two small-scale experiments on berm and dune erosion for a high and narrow berm (Experiment H) as well as a low and wide berm (Experiment L). The sand volume for the different berms was approximately the same. The median diameter, fall velocity, specific gravity, and porosity of the fine sand were $0.18\,mm$, $2.0\,cm/s$, 2.6 and 0.4, respectively. The significant wave height and spectral peak period were approximately $19\,cm$ and $2.6\,s$, respectively. The still water level S above the datum corresponding to the initial water level

at time $t = 0$ was varied by an increment of 5 or $10\,cm$ during each experiment that lasted 6.11 hours to simulate the changing water level during a storm. Figures 6.1 and 6.2 compare the measured and computed profiles at time $t = 2.0$, 3.67, and $6.11\,h$ starting from the initial profile at $t = 0$ for Experiments H and L, respectively. Measured initial profile and profile at each plotted time level are displayed as solid lines whereas computational results are shown as dashed lines. The maximum still water level (SWL) was $15\,cm$ above the datum during $t = 3.0 - 3.67\,h$. For the profile evolution comparison, $a_o = 0.1$ yielded the best result. This value is one order of magnitude lower than the values in the experiment with major overwash (Chapter 5) because only minor wave overtopping occurred during the maximum still water level in Experiment H and L. Erosion on the dune face above SWL and corresponding deposition below SWL is slightly overpredicted at all time time levels.

The agreement of the dune profile evolution in Figure 6.1 and the agreement in Figure 6.2 are similar to those presented by Kobayashi et al. (2010) using the numerical model without the overtopping term $a_o U_o V_s$ in Equation (4.26) but with parameter a set to unity in the unidirectional flow zone of $\overline{U} > 0$ over the dune crest (Section 4.3). The computed cross-shore variations of the sediment transport rates q_b and q_s given by Equations (4.25) and (4.26) indicate that the dune erosion in Experiments H and L was caused predominantly by the offshore transport of suspended sand seaward of the dune crest.

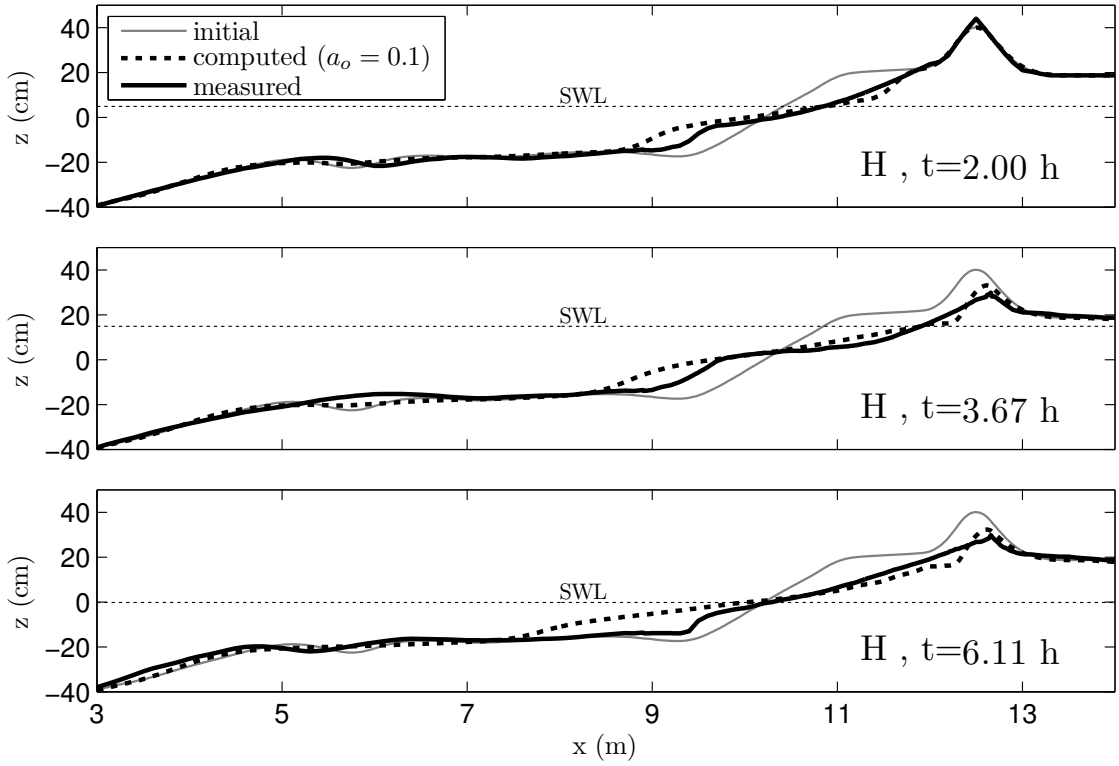

Figure 6.1: *Measured and computed profiles for Experiment H.*

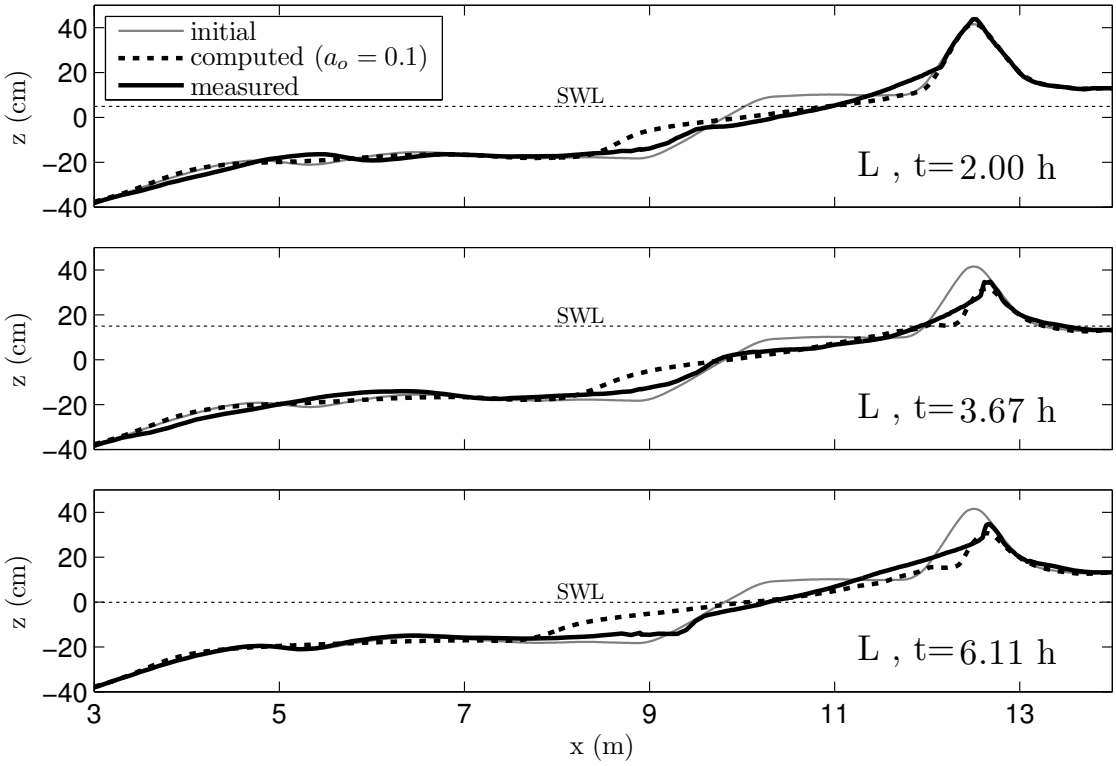

Figure 6.2: *Measured and computed profiles for Experiment L.*

Comparison is also made with the large-scale dune erosion tests by van Gent (2008). The median diameter, fall velocity, specific gravity and porosity of the fine sand used in these tests were $0.20\,mm$, $2.5\,cm/s$, 2.65 and 0.4, respectively. The still water level was constant in three tests $T01$, $T02$ and $T03$. The spectral peak period was 4.9, 6.1 and 7.3 s for tests $T01$, $T02$ and $T03$. The significant wave height was 1.41, 1.49 and 1.52 m for tests $T01$, $T02$ and $T03$. The duration of each test was 6 hours. Figure 6.3 compares the measured and computed profiles at the end ($t = 6\,h$) of the three tests where $a_o = 0.1$ is chosen since little or no overwash occurred. The numerical model underpredicts the dune erosion and corresponding depositional area in contrast to the comparison shown in Figures 6.1 and 6.2. The agreement in Figure 6.3 is similar to that obtained by Kobayashi et al. (2010) using the scarping procedure with no wet and dry zone. The present computation reaches the landward end located at $x = 184\,m$ but the computed overtopping and overwash rates are essentially zero. The present explicit modeling of the sediment transport on the steep dune face does not cause sufficient dune erosion perhaps because the computed offshore transport of suspended sediment at the toe of the eroding dune face is underpredicted.

The laboratory profile data presented in this section do not pertain to major overwash. The comparisons are useful in assessing the validity of the present CSHORE version. The present version of CSHORE with the modified suspended sediment transport equation (4.26) can predict profile evolution for laboratory situations ranging from no wave overtopping and overwash to major wave overtopping and overwash if the parameter a_o is calibrated. In the following section, comparisons with field data are presented.

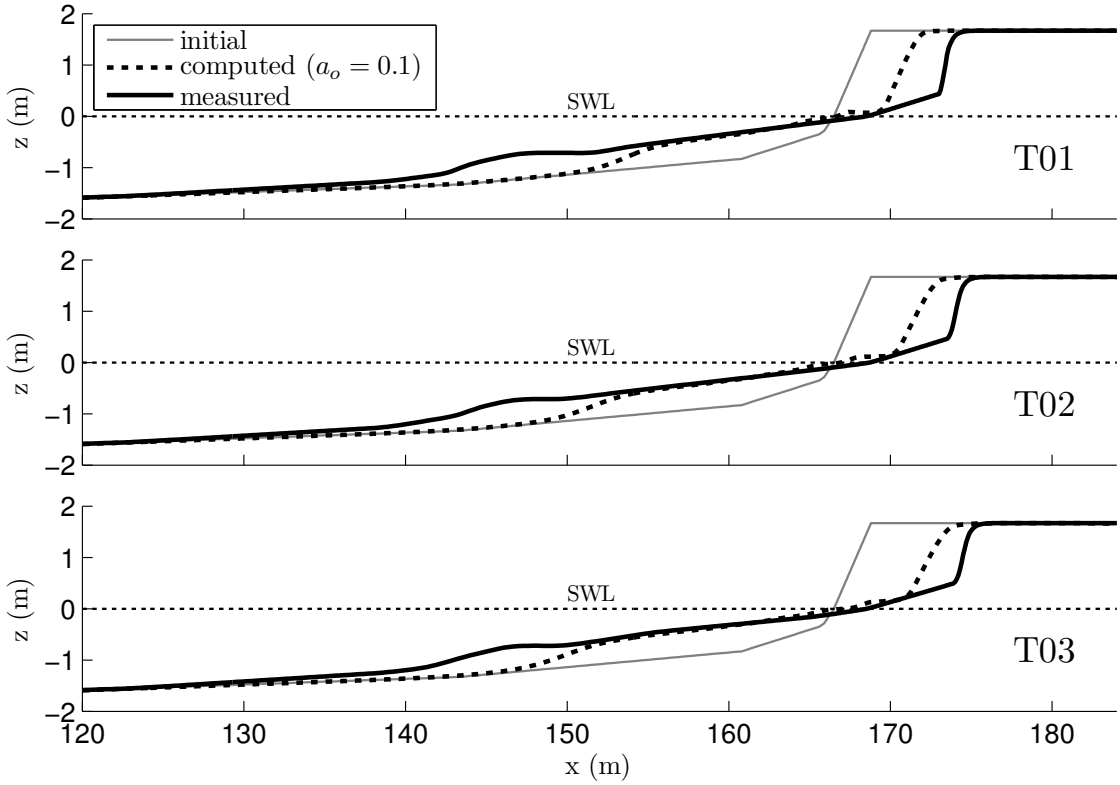

Figure 6.3: *Measured and computed profiles for tests T0, T1, and T3.*

6.2 Field Dune Data

Only few field data sets describing overwash of dunes are available. They are limited to pre- and post-storm profile measurements with considerable time lag between surveys. Flow velocities on the backdune, overtopping and overwash rates during dune overwash have not been measured in the field. This lack of measured hydrodynamic variables makes the numerical model calibration for such cases more difficult. In the following, CSHORE is compared with field data of overwashed dune profiles obtained at two locations at Ocean City, Maryland and one location at Dewey Beach, Delaware (Wise et al., 1996).

The beach at Ocean City, Maryland was impacted by the 30 October 1991 storm, 11 November 1991 storm, and 4 January 1992 storm after a major beach nourishment project. Wave and water elevation time series were measured at a depth of approximately 10 m. This location is taken as the seaward boundary $x = 0$ for the CSHORE computation. The October storm lasted about 4 days, with a peak significant wave height of approximately $3\,m$ and a peak water level of $1.5\,m$ above the datum $z = 0$ taken as the National Geodetic Vertical Datum (NGVD). The November storm lasted about 3 days with a peak significant wave height of $3\,m$ and a peak water level of $1.2\,m$. The January storm lasted about 3 days with a peak significant wave height of $4\,m$ and a peak water level of $2\,m$. The assumption of normally incident waves is made for lack of directional wave information. The median sand diameter was $d_{50} = 0.35\,mm$.

Figure 6.4 shows the comparison for Profile OJ86 in the report by Wise et al. (1996). The initial profile corresponds to the measured profile on 26 June 1991. The measured profile after the three storms was obtained on 11 January 1992. Measured pre and post storm profiles are displayed as thin and thick solid lines, respectively. The computation was carried out for the combined time series of the waves and water level for the three storms over the duration of 371 hours, neglecting the intervals

between the storms. Computed profiles are shown for IOVER=0 and IOVER=1 following Kobayashi et al. (2010). IOVER=0 corresponds to profile change computations including an empirical scarping procedure without wave overtopping and overwash (Kobayashi et al., 2009), whereas IOVER=1 computations include the wet and dry zone model (Section 4.2) with its overtopping and overwash formulations. Only the zone of noticeable profile changes is shown in this and subsequent figures. The dotted blue line shows the computed profile using $a_o = 0.1$ and the dash-dotted red line uses $a_o = 0.5$ to show the sensitivity of the field profile change to this parameter in Equation (4.26).

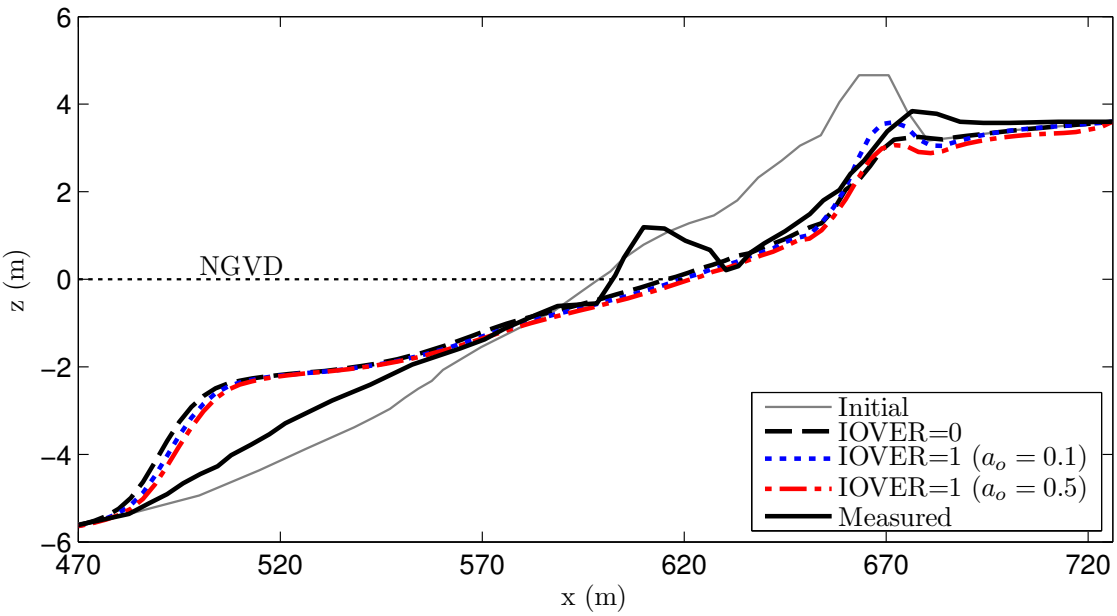

Figure 6.4: *Measured and computed beach profile (No.86) for Ocean City, MD. Surveys were conducted in June 1991 and January 1992. Computed profile evolution is based on the combined time series of three storms between the surveys.*

For $a_o = 0.1$ CSHORE predicts the dune crest elevation better but slightly underpredicts its onshore migration by approximately $10\,m$. For $a_o = 0.5$ dune erosion is overpredicted and the result is similar to IOVER=0. The present numerical model with $a_o = 0.1$ predicts the overwashed dune profile well but does not predict

the berm near the shoreline perhaps because the beach recovery after the January storm is not simulated. The computed wave overtopping rate q_o per unit width at the landward end located at $x = 726\,m$ is as large as $0.14\,m^2/s$ for a few hours. The corresponding suspended sand and bedload transport rates are $q_s = 1.6\,cm^2/s$ and $q_b = 0.25\,cm^2/s$. The present numerical model does not predict the deposition landward of the dune crest possibly because it does not include the lateral spreading and infiltration in the dry zone landward of the dune crest. The computed profiles for IOVER=0 and 1 indicate that the dune erosion for OJ86 must have been caused mostly by offshore sand transport.

Figure 6.5 shows the comparison for Profile NJ74 where the initial profile corresponds to the measured profile on 2 November 1991 after the October storm. The measured profile was surveyed on 11 January 1992. The computed profiles for IOVER=0 and 1 are based on the computations made for the combined time series of the waves and water level for the November and January storms over the duration of 168 hours. The computed profile for IOVER=1 ($a_o = 0.1$) shows very good agreement in dune crest elevation but the landward migration of the dune crest is not predicted. For $a_o = 0.5$ the computed profile is similar to IOVER=0 where the reduction in dune crest elevation is slightly overpredicted and the landward migration is not predicted. Using $a_o = 0.1$ results in computed q_o at the landward end ($x = 510\,m$) as large as $0.18\,m^2/s$ for a few hours. The corresponding sand transport rates are $q_s = 2.5\,cm^2/s$ and $q_b = 0.45\,cm^2/s$. The computed dune profile is in better agreement for IOVER=0 than for IOVER=1. The reduction of the dune crest height is predicted well for both IOVER=0 and IOVER=1 using the low value of $a_o = 0.1$, suggesting that the dune crest lowering must have been caused mostly by offshore sand transport.

Comparison is also made with dune erosion data with no dune crest lowering in the report by Wise et al. (1996). The beach at Dewey Beach, Delaware was

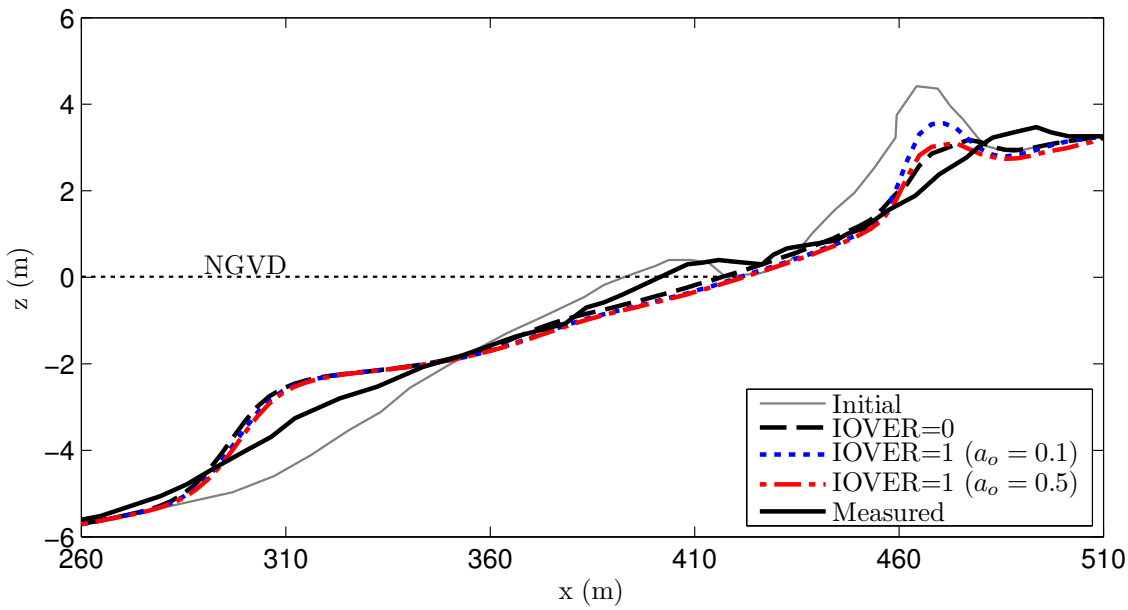

Figure 6.5: *Measured and computed beach profile (No.74) for Ocean City, MD. Surveys were conducted in November 1991 and January 1992. Computed profile evolution is based on the combined time series of two storms between the surveys.*

attacked by a storm on 10 December 1992. A wave gauge was located at a depth of 9 m off the coast of Dewey Beach. This location is taken as $x = 0$. This storm lasted about 4 days with a peak significant wave height of $4\,m$ and a peak water level of approximately $2\,m$. The median sand diameter was $d_{50} = 0.33\,mm$. The beach profile was surveyed on 29 October 1992 and 18 December 1992. Computation is made for the duration of 6 days only. Figure 6.6 shows the comparison for Dewey Beach profile 140. The storm completely eroded the berm and parts of the dune face in the initial profile and transported the sediment offshore. CSHORE computations for IOVER=1 are shown using $a_o = 0.1$ (dotted blue line) and $a_o = 0.5$ (dash-dotted red line). The computed profile for $a_o = 0.1$ indicates erosion of the landward slope of the dune where the computed bedload transport rate at the landward end located at $x = 459\,m$ is $q_b = 0.4\,cm^2/s$ for several hours. The corresponding computed suspended sand transport rate reaches maximum values of $q_s = 0.8\,cm^2/s$. The

computed result for $a_o = 0.5$ clearly overpredicts dune erosion and is shown here to indicate the sensitivity of the dune profile evolution to this parameter. Dune crest lowering is predicted by both IOVER=0 and 1 but the measured profiles did not show any crest lowering. This implies that the offshore sand transport rate on the seaward slope of the dune is overpredicted. The numerical model does not predict the seaward spreading of the deposited sand perhaps because of the assumption of normally incident waves and no longshore current. Longshore current increases the volume of suspended sediment which can be transported offshore by return (undertow) current.

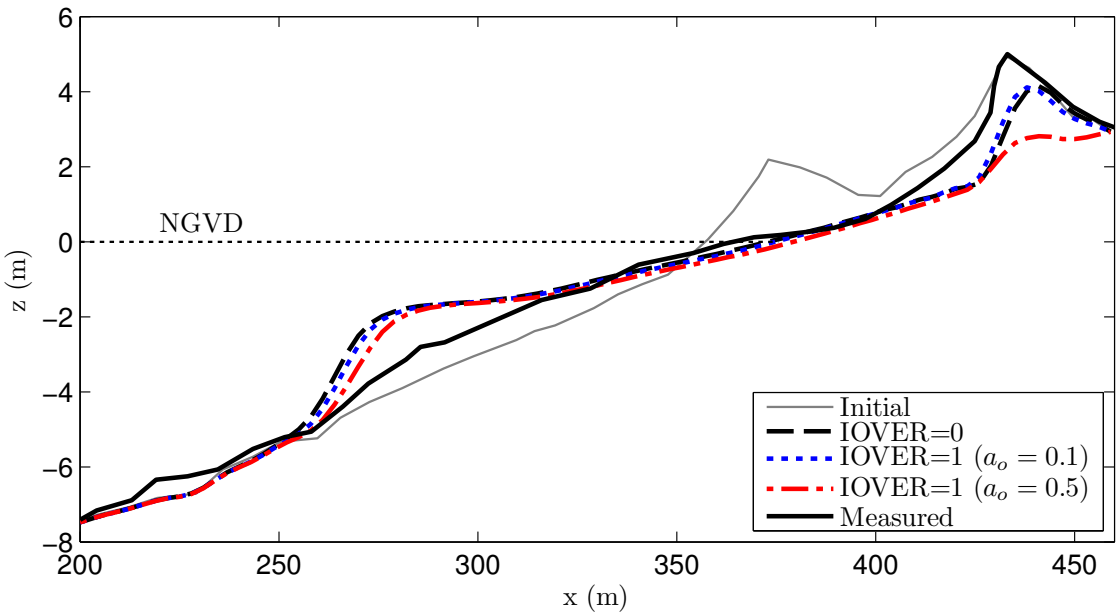

Figure 6.6: *Measured and computed beach profiles for Dewey Beach profile 140. Surveys were conducted in October and December 1992. Computed profile evolution is based on the time series of a 6-day storm in December 1992.*

The degree of the agreement for the field data in Figures 6.4 - 6.6 is similar to that for the laboratory data in Figures 6.1 and 6.2. The numerical model is not calibrated for the field data alone because of the additional assumptions made for the field data comparison such as the assumption of normally incident waves and no

profile change during the intervals before, between, and after the storms specified as input. Computation will need to be extended to the interval of beach recovery to assess the capability of the present numerical model in predicting beach recovery after a storm.

Chapter 7

CONCLUSIONS

Three different dune configurations with the same volume of fine sand were tested in a wave flume for their resilience against destruction by wave-induced overwash under the same wave conditions and constant water level. These configurations were a berm with a dune (BD), a wide dune (WD) and a slope in front of a dune (SD). A cross-shore array of eight capacitance wave gauges and two acoustic Doppler velocimeters provided hydrodynamic data during a total of 45 runs, each with 400 s of waves. Before and after each run, a laser line scanner system consisting of two distance lasers, a rotating mirror assembly and a motorized cart recorded detailed 3D bathymetry in high resolution in a continuous fashion. Water and sediment transported over the low-crested vertical wall behind the backdune were collected in a basin with a sand trap. The trapped sand volume and collected water volume were used to obtain the wave overtopping rate and onshore sediment transport rate for each run. The size distribution of the trapped sand was also analyzed. Each tests continued until the bottom elevation in front of the wall reached the still water level (SWL).

Three phases of the observed overwash and profile evolution processes were identified. The transition from minor to major overwash during phase 2 occurred rapidly after the initial profile adjustment in phase 1 dominated by dune scarping and offshore sediment transport. The effect of the wall became dominant only in phase 3 where the wave overtopping rate was limited by the crest height of the

exposed wall. The exposed wall was effective in reducing the onshore sand transport rate. No local scour occurred at the wall. This type of structure is effective in reducing flooding damage and sand overwash. The experiment has shown that if peak tide is reached rapidly during a storm, a berm-dune configuration (BD) will resist better against wave-induced overwash than a wide dune (WD) or a sloped dune (SD) configuration.

After modifying the sediment transport model used in the numerical model CSHORE, the measured hydrodynamics, profile change and overwash data are shown to be predictable for phases 1 and 2. Further work is needed to better parameterize sand suspension and onshore transport on the beach in front of the exposed wall during phase 3. The strong feedback of the rapid bathymetric change to the wave motion on the dune and exposed vertical wall makes the numerical modeling very challenging. Planned future experiments include detailed measurements on wet probability and hydrodynamics on the backdune and in front of the wall to gain a better insight into the complicated processes taking place in these locations. Continuing detailed laboratory experiments is essential in guiding the development of realistic numerical models.

The versatility of CSHORE is further demonstrated by comparing the numerical model results to additional laboratory experiments and available field data. Comparing CSHORE with three different laboratory experiments on wave overtopping and overwash of different intensities has shown that by adjusting the new overtopping parameter a_o in the suspended sediment transport formulation the model yields similar profile agreement for no, minor, and major overwash data. Field data on wave overtopping of dunes and associated overwash are rare. The comparison of CSHORE with pre- and post storm profiles at two sites of dune overwash and one site of dune erosion has shown that the good agreement of measured and computed profiles requires a_o values one order of magnitude smaller than for the comparison

of the major overwash experiment presented in Chapter 5. The reduced value of a_o for the previous laboratory experiments may be due to the fact that no or only minor overwash occurred. For the case of the field data with some overwash the neglected lateral spreading of overwash flow and overwash sediment on the landward side of the dune may be responsible for the required reduction of the parameter a_o to mimic the horizontally two-dimensional effect in this cross-shore one-dimensional model. Further improvements of the numerical model may require lateral spreading of overwash in the sediment transport formulation as well as the prediction of beach recovery after a storm.

Appendix A

COMPUTED HYDRODYNAMICS IN WET ZONE

A.1 Energy Flux and Dissipation Terms

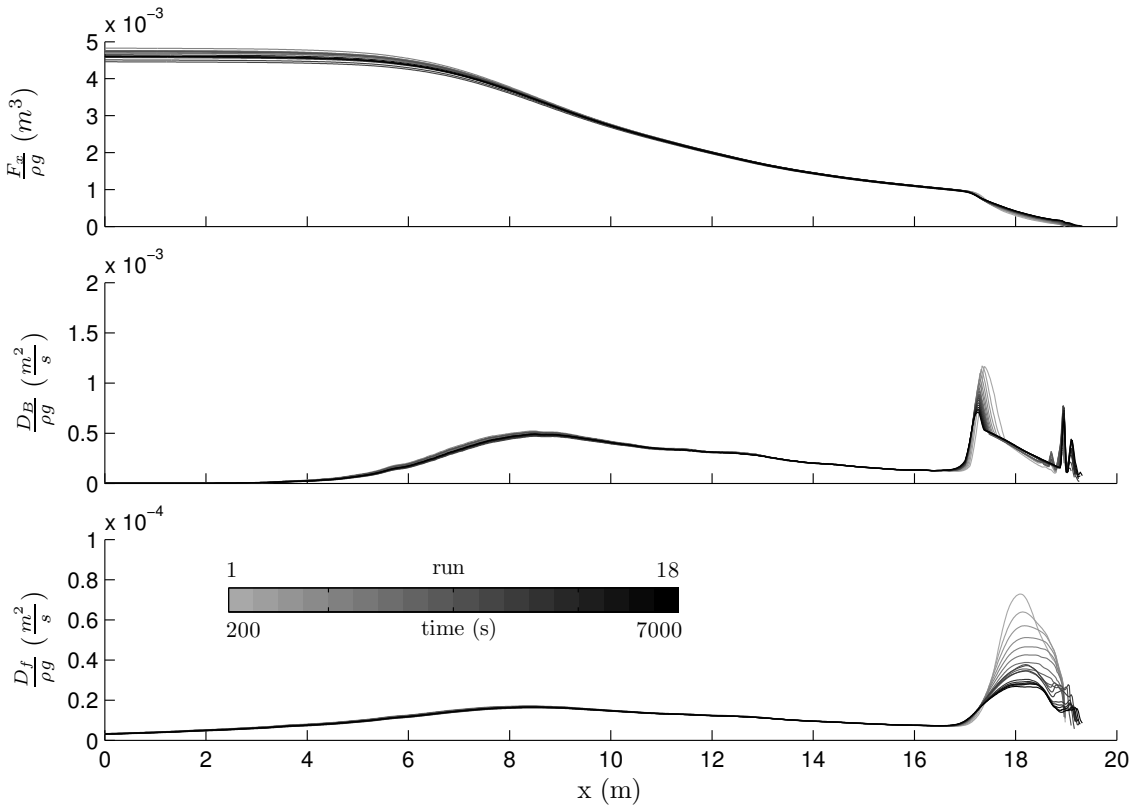

Figure A.1: *Computed cross-shore energy flux $F_x/\rho g$, dissipation due to wave breaking $D_B/\rho g$, and dissipation due to bottom friction $D_f/\rho g$ for all 18 runs of the BD test where CSHORE computes these variables in the wet zone divided by the unit water weight ρg. Gray shades denote run number and corresponding time at the middle of each 400-s run.*

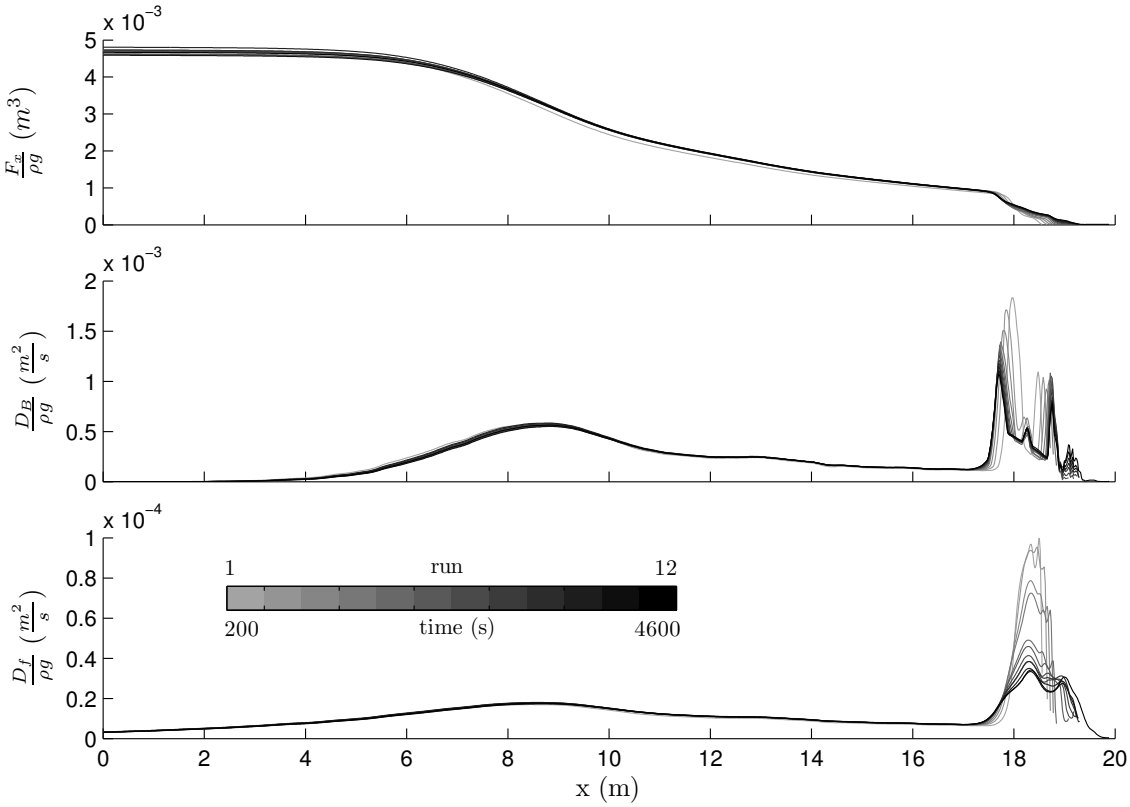

Figure A.2: *Computed cross-shore energy flux $F_x/\rho g$, dissipation due to wave breaking $D_B/\rho g$, and dissipation due to bottom friction $D_f/\rho g$ for all 12 runs of the WD test. Gray shades denote run number and corresponding time at the middle of each 400-s run.*

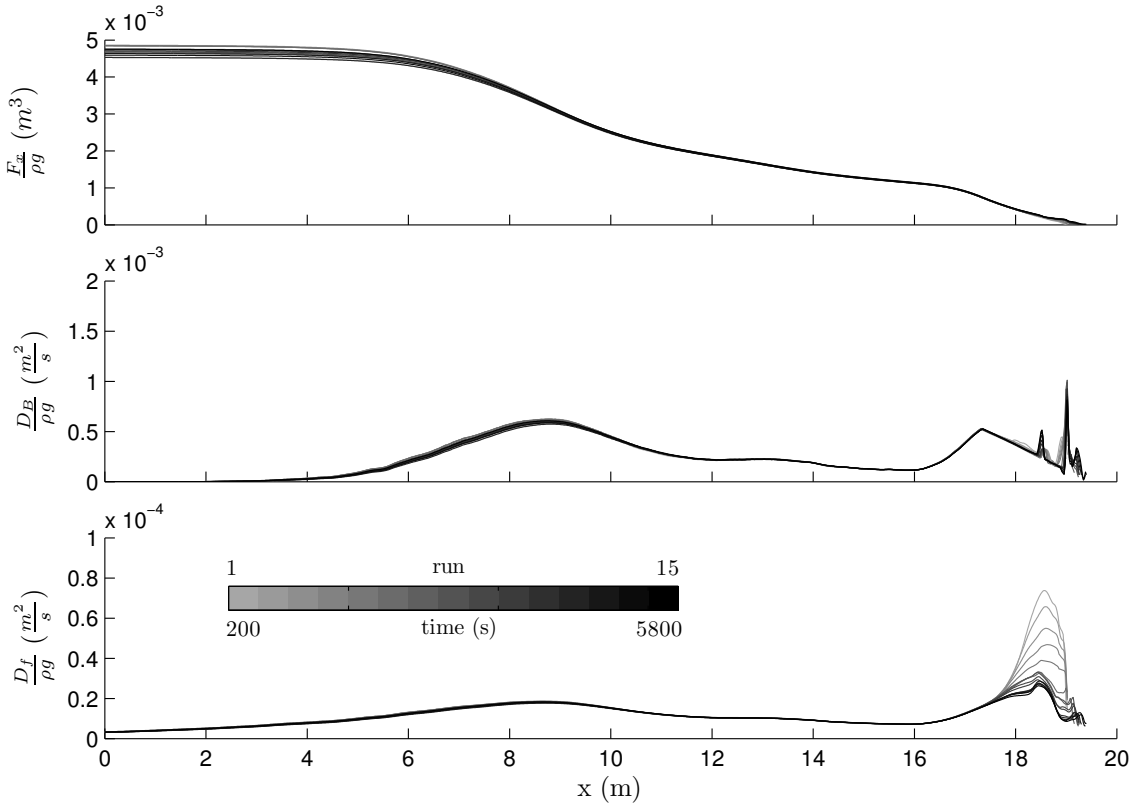

Figure A.3: *Computed cross-shore energy flux $F_x/\rho g$, dissipation due to wave breaking $D_B/\rho g$, and dissipation due to bottom friction $D_f/\rho g$ for all 15 runs of the SD test. Gray shades denote run number and corresponding time at the middle of each 400-s run.*

A.2 Radiation Stress Term and Bottom Friction

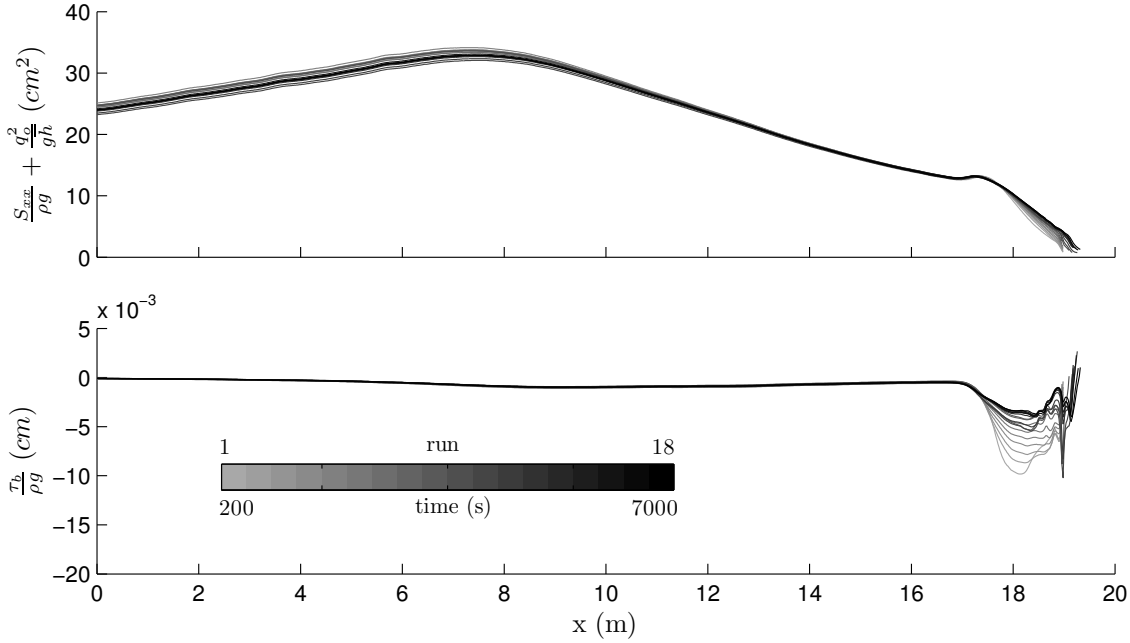

Figure A.4: *Computed cross-shore radiation stress term* $\left(\frac{S_{xx}}{\rho g} + \frac{q_o^2}{gh}\right)$ *and bottom shear stress* $\frac{\tau_b}{\rho g}$ *for all 18 runs of the BD test. Gray shades denote run number and corresponding time at the middle of each 400-s run.*

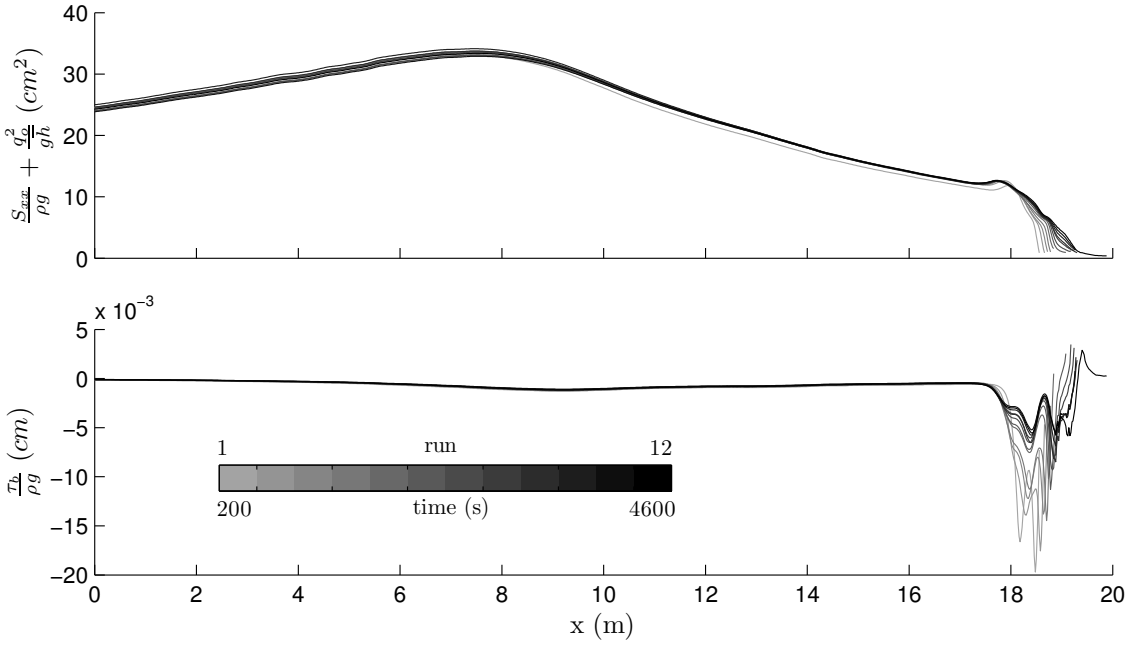

Figure A.5: *Computed cross-shore radiation stress term* $\left(\frac{S_{xx}}{\rho g} + \frac{q_o^2}{g\bar{h}}\right)$ *and bottom shear stress* $\frac{\tau_b}{\rho g}$ *for all 12 runs of the WD test. Gray shades denote run number and corresponding time at the middle of each 400-s run.*

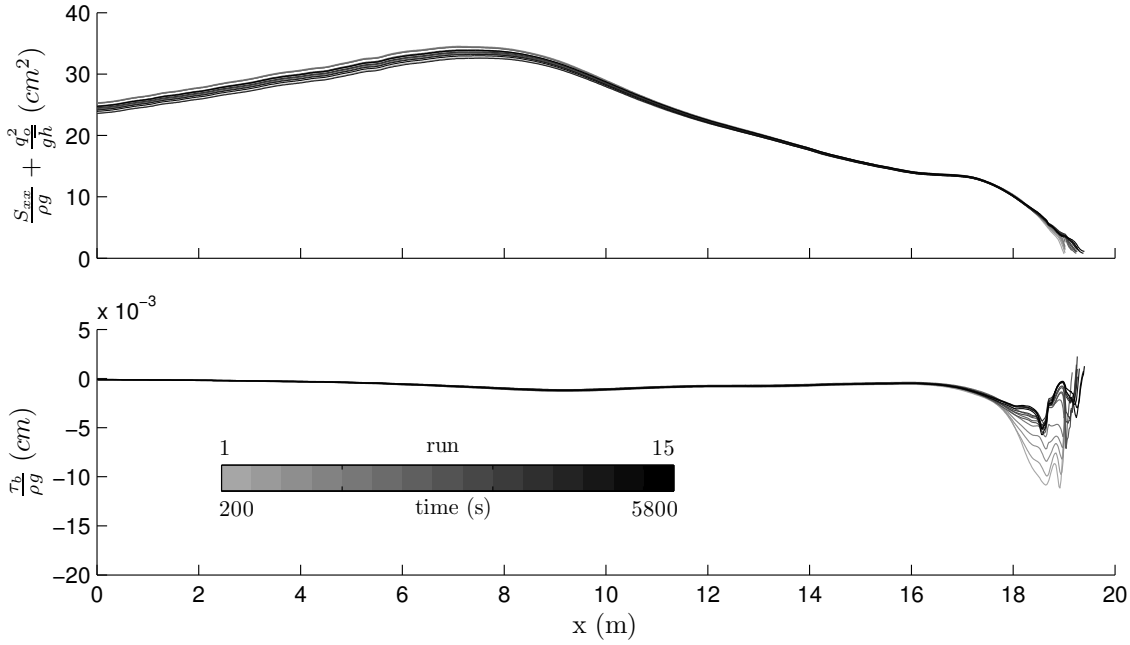

Figure A.6: *Computed cross-shore radiation stress term* $\left(\frac{S_{xx}}{\rho g} + \frac{q_o^2}{g\bar{h}}\right)$ *and bottom shear stress* $\frac{\tau_b}{\rho g}$ *for all 15 runs of the SD test. Gray shades denote run number and corresponding time at the middle of each 400-s run.*

A.3 Intrinsic Wave Period, Breaking Wave Fraction, and Roller Volume Flux

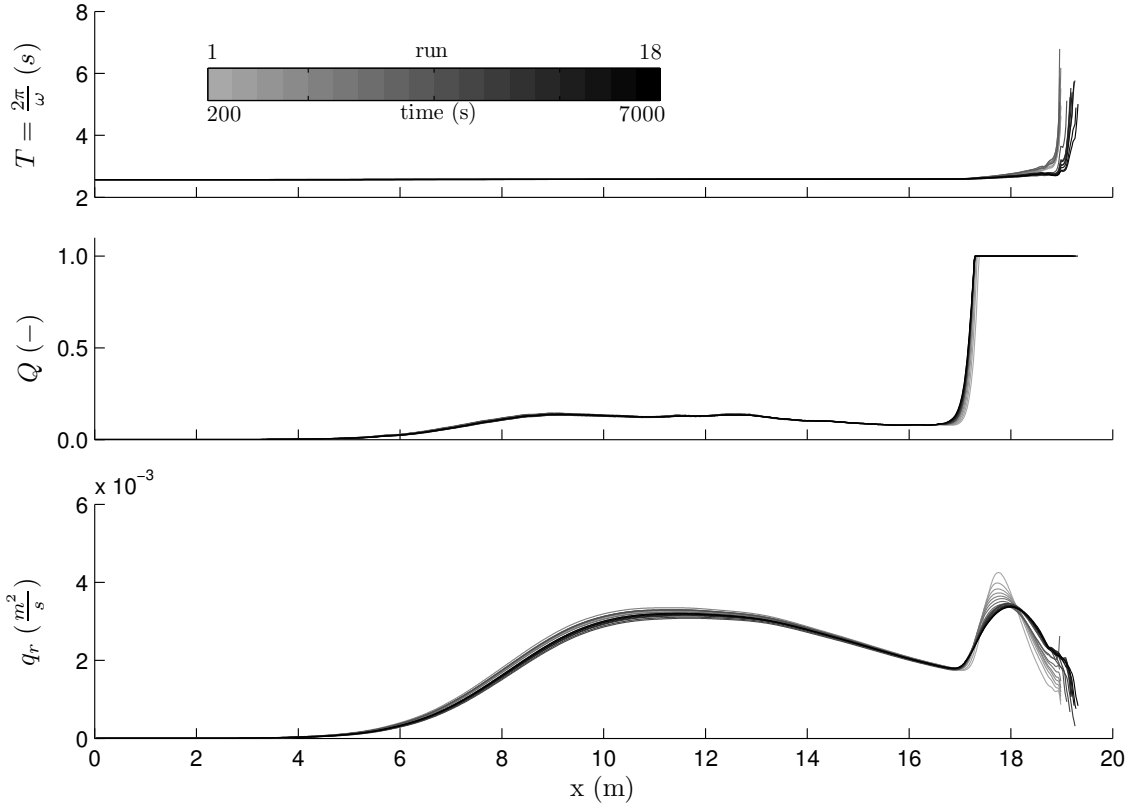

Figure A.7: *Computed intrinsic wave period $T = \frac{2\pi}{\omega}$, fraction of breaking waves Q, and roller volume flux q_r for all 18 runs of the BD test. Gray shades denote run number and corresponding time at the middle of each 400-s run.*

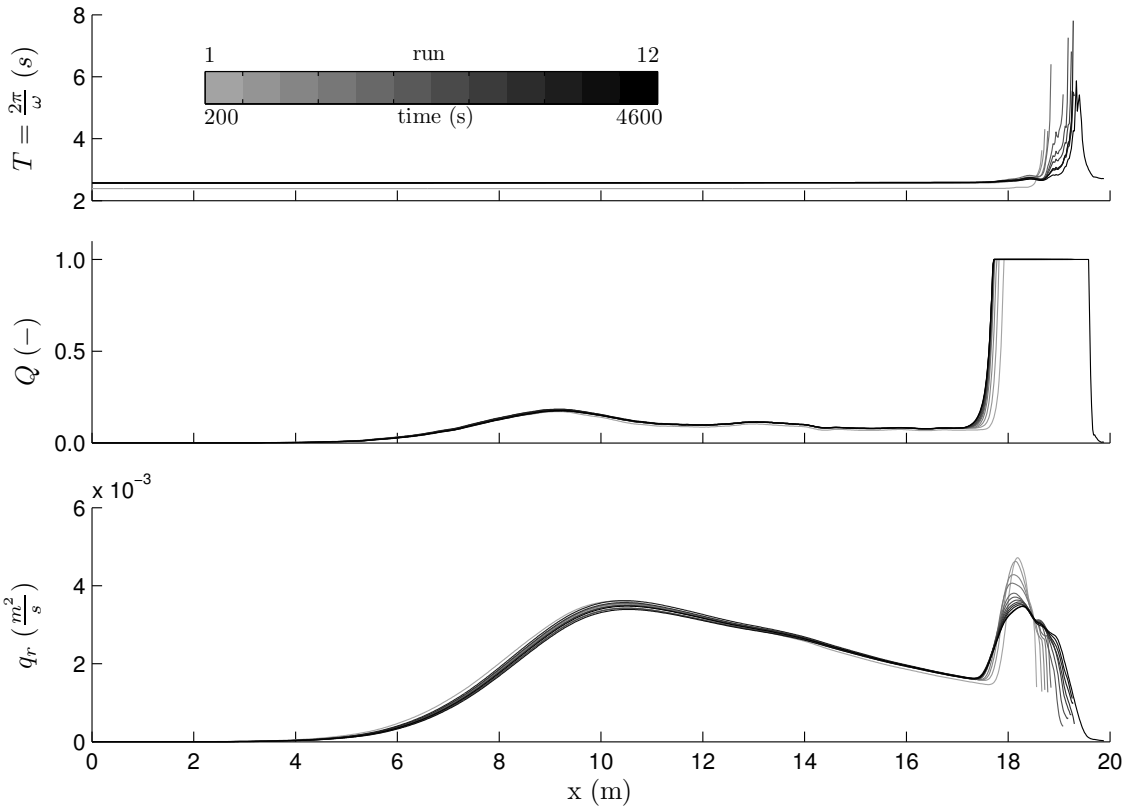

Figure A.8: *Computed intrinsic wave period $T = \frac{2\pi}{\omega}$, fraction of breaking waves Q, and roller volume flux q_r for all 12 runs of the WD test. Gray shades denote run number and corresponding time at the middle of each 400-s run.*

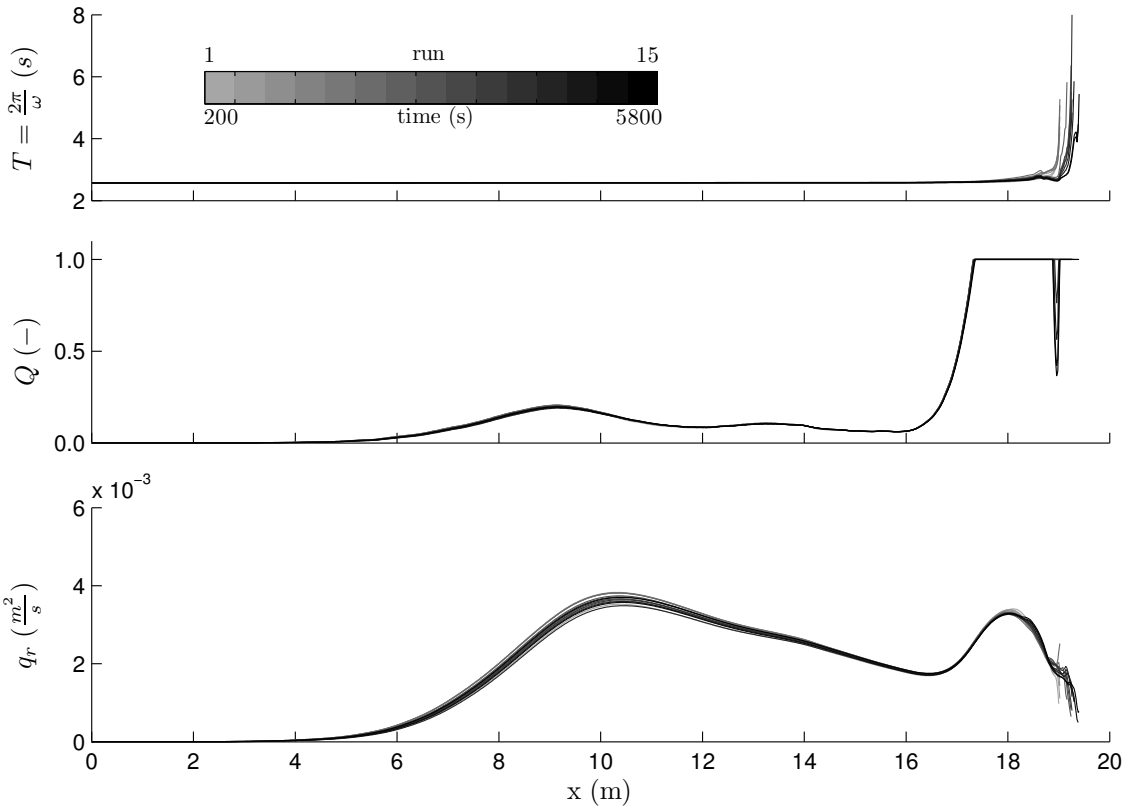

Figure A.9: *Computed intrinsic wave period $T = \frac{2\pi}{\omega}$, fraction of breaking waves Q, and roller volume flux q_r for all 15 runs of the SD test. Gray shades denote run number and corresponding time at the middle of each 400-s run.*

Appendix B

COMPUTED SEDIMENT TRANSPORT

B.1 Probability of Sediment Movement and Suspension and Suspended Volume

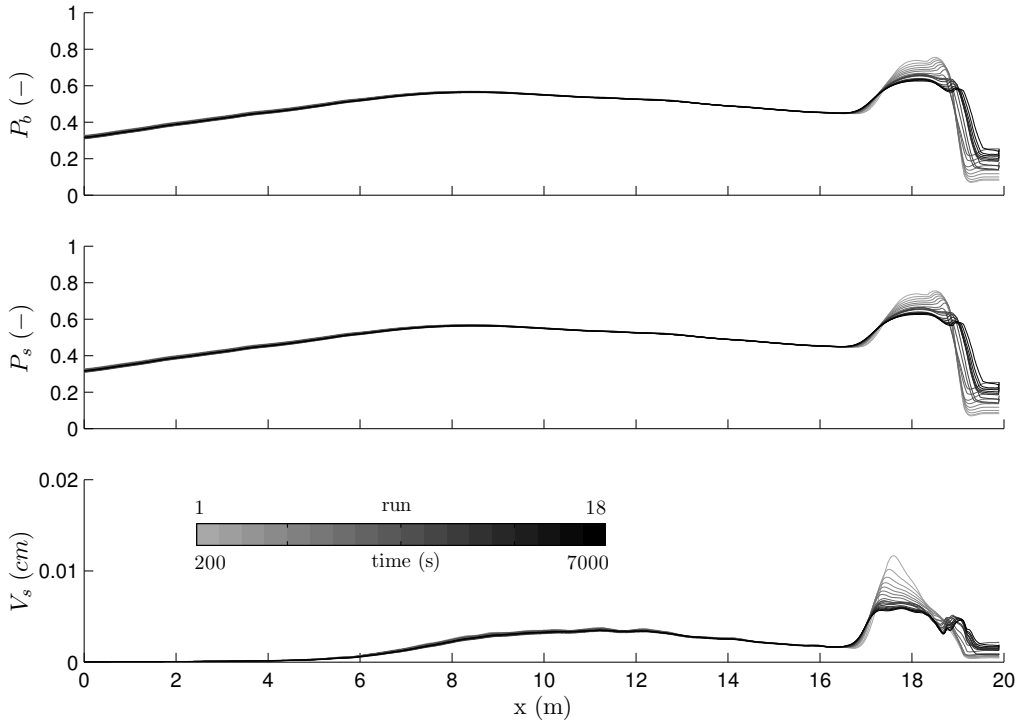

Figure B.1: *Computed probabilities of sediment movement P_b and suspension P_s and suspended sediment volume V_s per unit area for all 18 runs of the BD test. Gray shades denote run number and corresponding time at the middle of each 400-s run.*

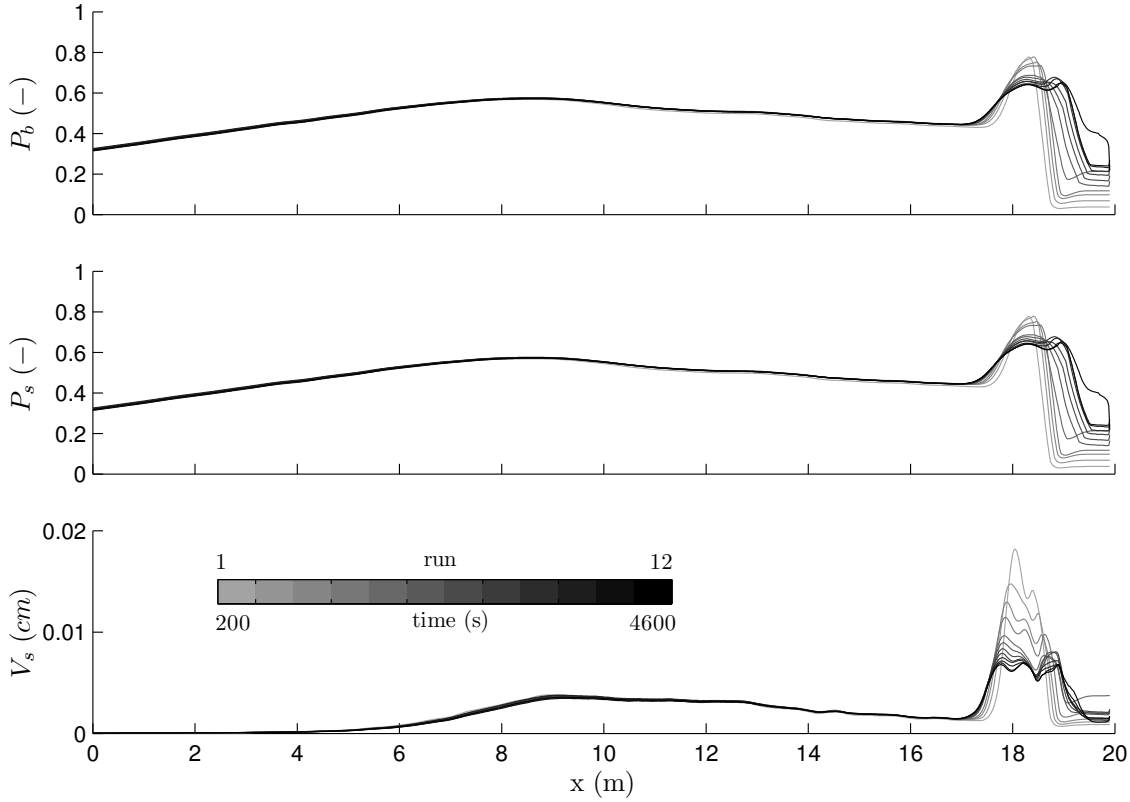

Figure B.2: *Computed probabilities of sediment movement P_b and suspension P_s and suspended sediment volume V_s per unit area for all 12 runs of the WD test. Gray shades denote run number and corresponding time at the middle of each 400-s run.*

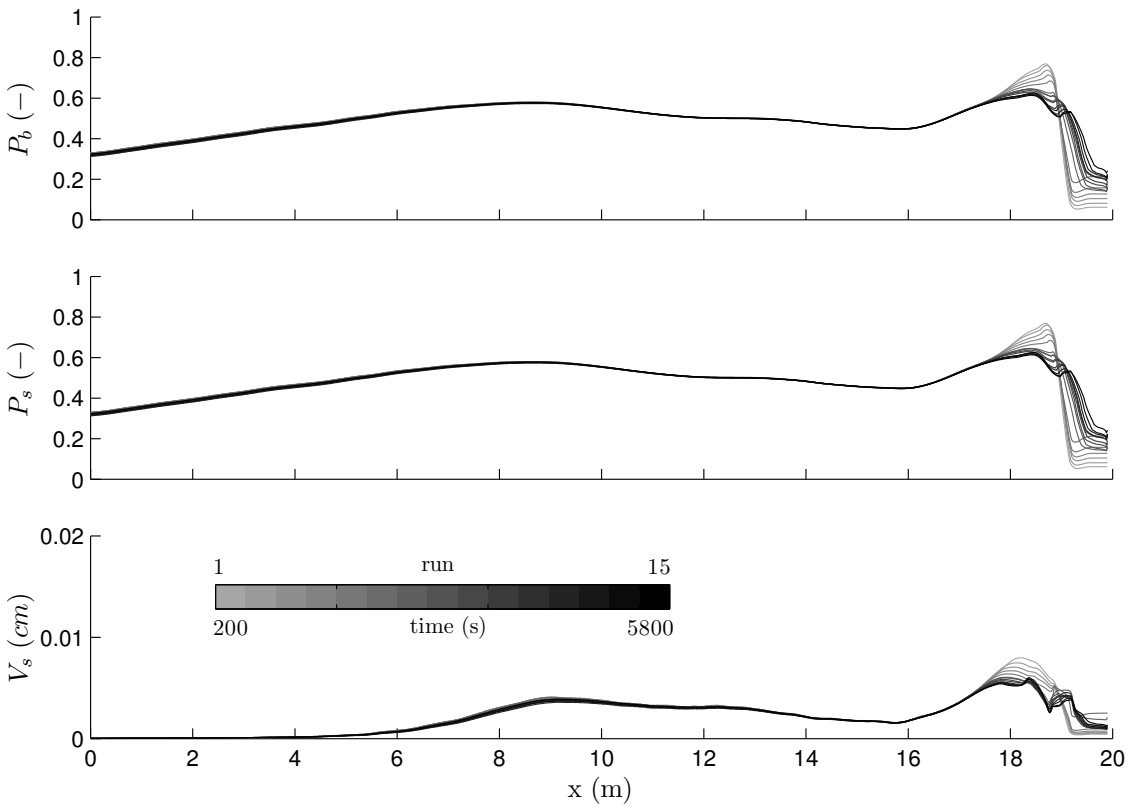

Figure B.3: *Computed probabilities of sediment movement P_b and suspension P_s and suspended sediment volume V_s per unit area for all 15 runs of the SD test. Gray shades denote run number and corresponding time at the middle of each 400-s run.*

B.2 Bed Load and Suspended Load Transport Rates

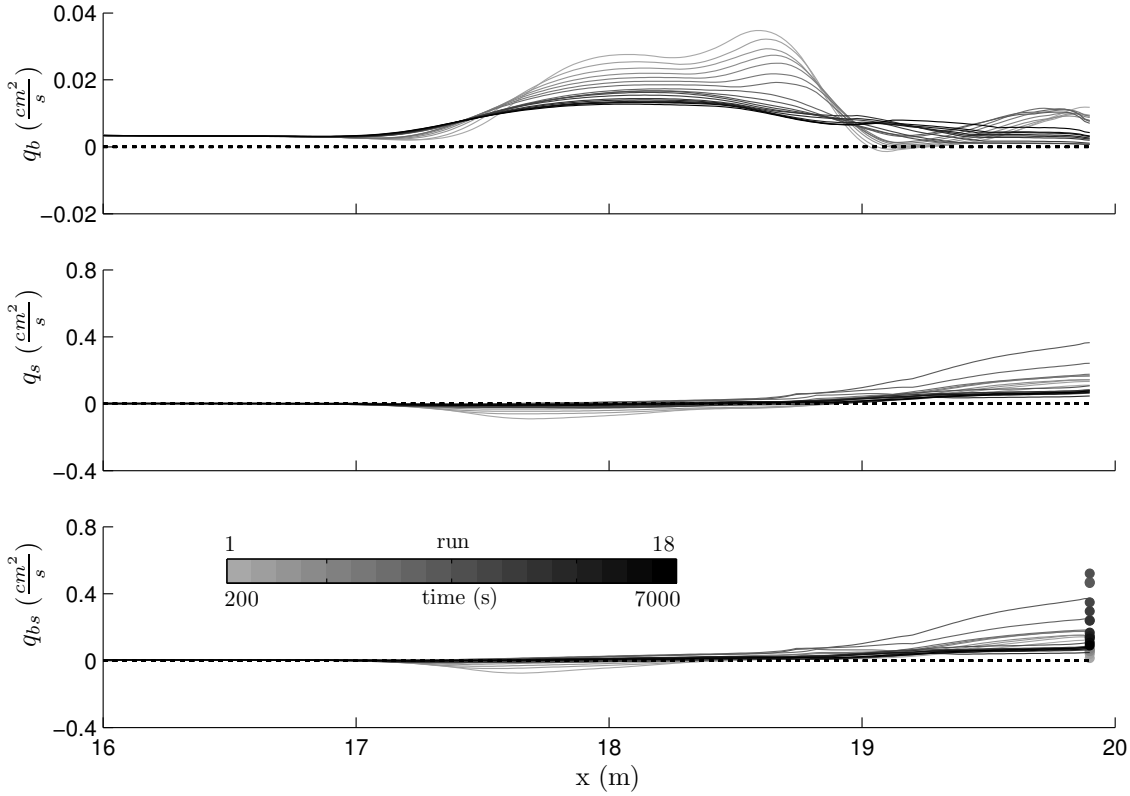

Figure B.4: *Computed bed load transport rate q_b, suspended load transport rate q_s and combined rate q_{bs} for all 18 runs of the BD test. Gray shades denote run number and corresponding time at the middle of each 400-s run. Measured data for q_{bs} over the vertical wall is displayed as circles in the bottom panel.*

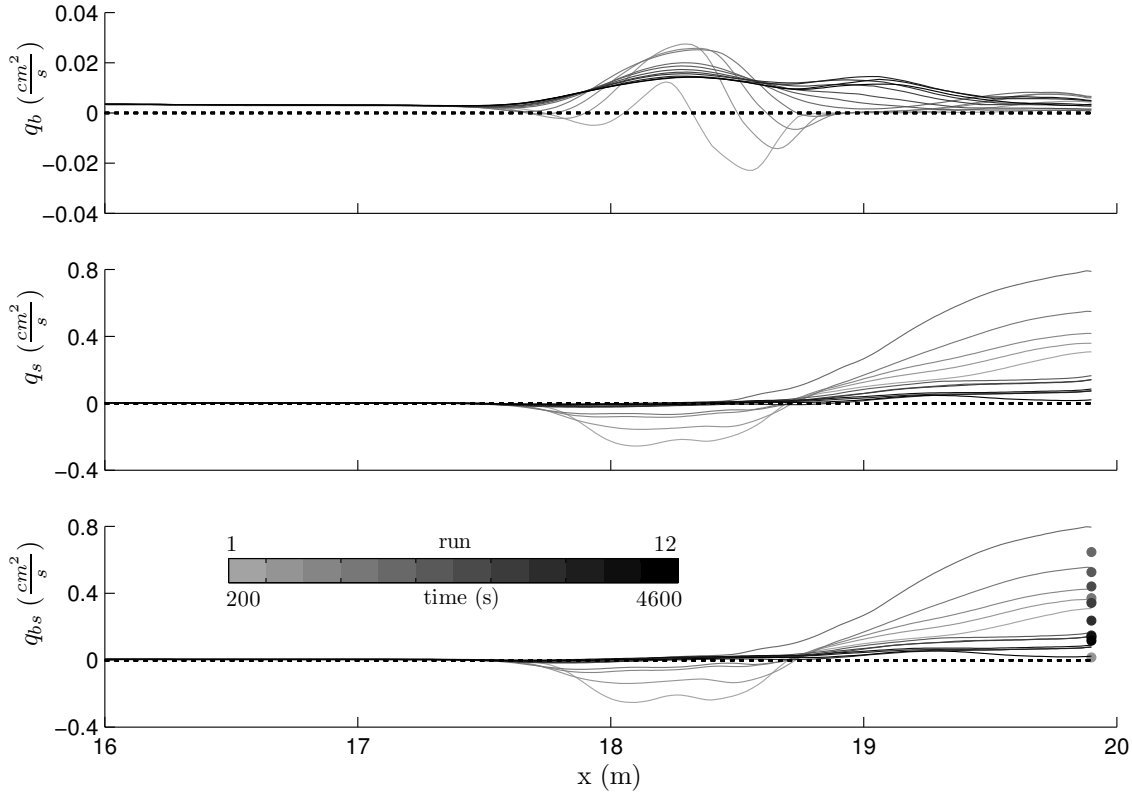

Figure B.5: *Computed bed load transport rate q_b, suspended load transport rate q_s and combined rate q_{bs} for all 12 runs of the WD test. Gray shades denote run number and corresponding time at the middle of each 400-s run. Measured data for q_{bs} over the vertical wall is displayed as circles in the bottom panel.*

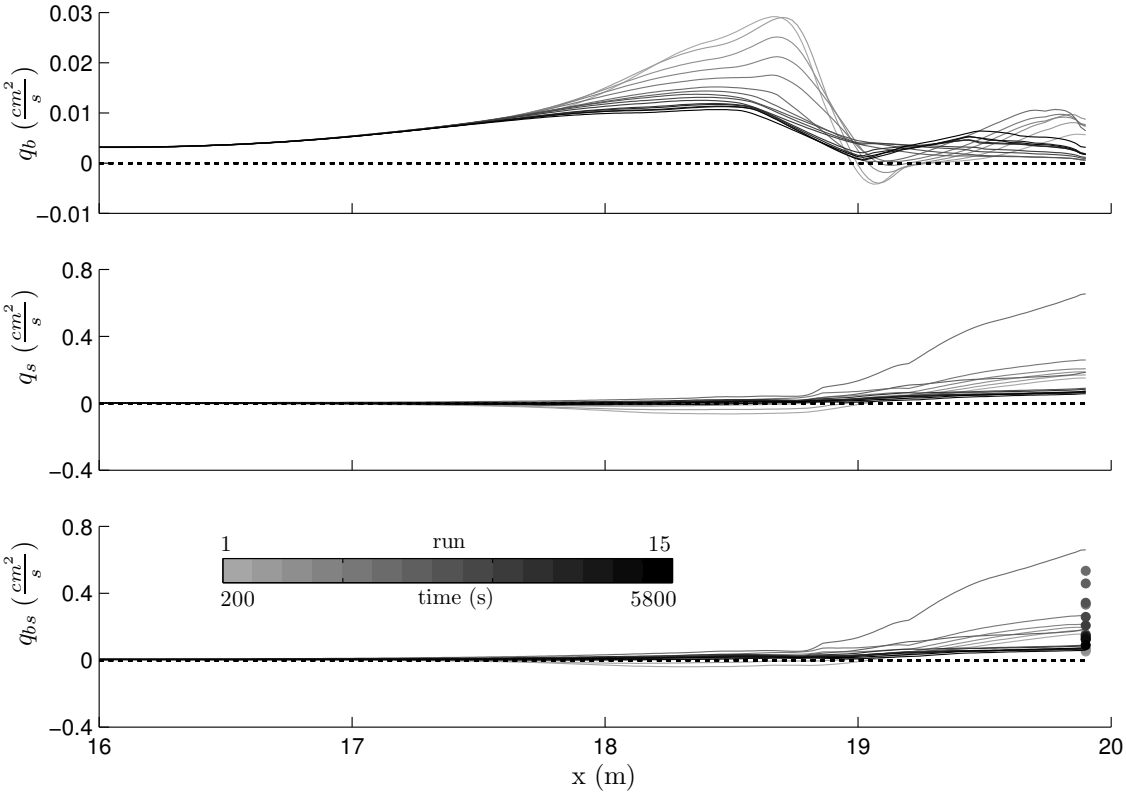

Figure B.6: *Computed bed load transport rate q_b, suspended load transport rate q_s and combined rate q_{bs} for all 15 runs of the SD test. Gray shades denote run number and corresponding time at the middle of each 400-s run. Measured data for q_{bs} over the vertical wall is displayed as circles in the bottom panel.*

References

Acuity (2003a). *AccuRange 1000 laser distance sensor user's manual.* Schmitt Measurement Systems, Inc.

Acuity (2003b). *AccuRange 4000 laser rangefinder and AccuRange line scanner user's manual.* Schmitt Measurement Systems, Inc.

Battjes, J. and Stive, M. (1985). Calibration and verification of a dissipative model for random breaking waves. *Journal of Geophysical Research*, 90(C5):9159–9167.

Boers, M. (1996). Simulation of a surf zone with a barred beach: Part 1: wave heights and wave breaking. Communication on Hydraulic and Geotechnical Engineering, Report No. 96-5, Delft University of Technology, Delft.

Buck, M., Kobayashi, N., Payo, A., and Johnson, B. D. (2007). Berm and dune erosion during a storm. Research Report CACR-07-03, University of Delaware Center for Applied Coastal Research.

CEM (2003). *Coastal Engineering Manual, Part V.* Coastal and Hydraulics Laboratory, U.S. Army Engineer Research and Development Center, Vicksburg, Miss.

Donnelly, C., Kraus, N., and Larson, M. (2006). State of knowledge on measurement and modeling of coastal overwash. *Journal of Coastal Research*, 22(4):965–991.

Dunnum, C. (2006). *CTI-HSIF-PCI software library for Acuity AR4000 laser distance sensors and PCI High-Speed Interface Card programmer's guide and reference manual.* Crandun Technologies, Inc.

Goda, Y. (2000). *Random seas and design of maritime structures*, volume 15 of *Advanced Series on Ocean Engineering*. World Scientific, Singapore.

Henderson, F. (1966). *Open Channel Flow*. Macmillan, New York, N.Y.

Holland, K. T., Holman, R. A., and Asbury H. Sallenger, J. (1991). Estimation of overwash bore velocities using video techniques. In Kraus, N. C., editor, *Coastal Sediments '91*, volume 1, pages 489–487. ASCE.

Kobayashi, N., Buck, M., Payo, A., and Johnson, B. D. (2009). Berm and dune erosion during a storm. *Journal of Waterway, Port, Coastal, and Ocean Engineering*, 135(1):1–10.

Kobayashi, N., Cox, D. T., and Wurjanto, A. (1990). Irregular wave reflection and run-up on rough impermeable slopes. *Journal of Waterway, Port, Coastal, and Ocean Engineering*, 116(6):708–726.

Kobayashi, N., DeSilva, G., and Watson, K. (1989). Wave transformation and swash on gentle and steep slopes. *Journal of Geophysical Research*, 94(C1):951–966.

Kobayashi, N., Farhadzadeh, A., Melby, J. A., Johnson, B. D., and Gravens, M. (2010). Wave overtopping of levees and overwash of dunes. *Journal of Coastal Research*, (in press).

Kobayashi, N., Herrman, M., Johnson, B. D., and Orzech, M. (1998). Probability distribution of surface elevation in surf and swash zones. *Journal of Waterway, Port, Coastal, and Ocean Engineering*, 124(3):99–107.

Kobayashi, N., Meigs, L. E., Ota, T., and Melby, J. A. (2007). Irregular breaking wave transmission over submerged porous breakwater. *Journal of Waterway, Port, Coastal, and Ocean Engineering*, 133(3):104–116.

Kobayashi, N., Payo, A., and Schmied, L. (2008). Cross-shore suspended sand and bed load transport on beaches. *Journal of Geophysical Research*, 113(C07001).

Kobayashi, N., Tega, Y., and Hancock, M. W. (1996). Wave reflection and overwash of dunes. *Journal of Waterway, Port, Coastal, and Ocean Engineering*, 122(3):150–153.

Kobayashi, N., Zhao, H., and Tega, Y. (2005). Suspended sand transport in surf zones. *Journal of Geophysical Research*, 110(C12009):1–21.

Kraus, N. C. and McDougal, W. G. (1996). The effects of seawalls on the beach: Part I, an updated literature review. *Journal of Coastal Research*, 12(3):691–701.

Mei, C. C. (1989). *The applied Dynamics of ocean surface waves*. Advanced Series on Ocean Engineering. World Scientific, Singapore.

Tega, Y. and Kobayashi, N. (1996). Wave overwash of subaerial dunes. In *Proceedings of the 25th International Conference on Coastal Engineering*, pages 4148–4160. World Scientific, Singapore.

van Gent, M. (2008). Large-scale tests to analyse the influence of collapsed dune revetments on dune erosion. In *Proceedings of the 31st International Conference on Coastal Engineering*, pages 2583–2595. World Scientific, Singapore.

Wamsley, T. V., Kraus, N. C., Larson, M., Hanson, H., and Connell, K. (2006). Coastal barrier breaching: comparison of physical and numerical models. In *Proceedings of the 30th International Conference on Coastal Engineering*, pages 2818–2828. World Scientific, Singapore.

Wise, R. A., Smith, S., and Larson, M. (1996). SBEACH: Numerical model for simulating storm-induced beach change. Report 4. cross-shore transport under

random waves and model validation with SUPERTANK and field data. Technical Report CECR-89-9, U.S. Army Engineer Waterways Experiment Station.